

Mechanical and functional properties of nano-structured polyvinylidene fluoride and its carbon nanotube composites

Chen, Xuelong

2016

Chen, X. (2016). Mechanical and functional properties of nano-structured polyvinylidene fluoride and its carbon nanotube composites. Doctoral thesis, Nanyang Technological University, Singapore.

<https://hdl.handle.net/10356/69098>

<https://doi.org/10.32657/10356/69098>



NANYANG
TECHNOLOGICAL
UNIVERSITY

**Mechanical and Functional Properties of Nano-Structured
Polyvinylidene Fluoride and Its Carbon Nanotube Composites**

Chen Xuelong

School of Materials Science and Engineering

2016

Mechanical and Functional Properties of Nano-Structured Polyvinylidene Fluoride and Its Carbon Nanotube Composites

School of Materials Science and Engineering

A thesis submitted to the Nanyang Technological University
in partial fulfilment of the requirement for the degree of
Doctor of Philosophy

2016

Abstract

Polyvinylidene Fluoride (PVDF) is one type of semicrystalline fluoropolymers that has been widely used in automotive and chemical industries, semiconductor, biomedical and sensor applications; owing to its superior chemical resistance, excellent mechanical properties and unique electronic properties. Polymeric composites containing nanoscale fillers, such as graphene, carbon nanotube (CNTs) or nanoclay often render polymers with interesting mechanical, structural, electrical, optical and many other functional properties. The objective of this work is to improve mechanical and functional properties of PVDF by the advantageous introduction of CNTs. Studies will focus on the preparation methodology of PVDF/CNTs composites with uniform morphology, the interaction between CNTs and polymer matrix and surface treatment of CNTs.

The surface properties of CNTs often play an important role in determining the performance of polymer/CNTs composites. Therefore, in the first study, we focused on studying the surface functionalization of CNTs. Controlled thermal annealing in air was employed in order to oxidize CNTs. It was found that longer time/higher temperature can effectively increase the oxygen content in CNTs. Shorter duration/higher temperature annealing results in more C-O-C groups than longer duration/lower temperature annealing, while the latter yields more C=O groups. The mechanism of CNT surface functionalization by air annealing was proposed.

In the following work, PVDF/CNTs composites with well dispersed and distributed CNTs were fabricated using both solution mixing and melt extrusion strategies. The introduction of low content of CNTs lead to an unusual observation of large enhancement in ductility; while marginal increase were observed for Young's modulus and tensile strength. Systematic characterizations lead to the conclusion that the unexpected phenomenon is correlated with the change of polymorphs because of the existence of CNTs. Mechanism of phase

transformation and pinning effect are proposed to further elucidate the phenomenon.

In the third study, we explore the possibility using PVDF and its CNTs composites for oil/water separation applications. PVDF and PVDF/CNTs aerogel were fabricated through a vapor induced phase inversion process. Contributed by the hierarchical micro-nano structure that is tailorable by PVDF concentration, both surfactant-free and surfactant-stabilized oil-in-water emulsion could be effectively separated by the fabricated PVDF aerogel simply under gravity, with good flux and high filtrate purity up to 99.99%. PVDF aerogel also exhibited moderate oil absorption capacity and almost instantaneous oil up-taking when tested using various types of oil. Furthermore, PVDF aerogel is highly stable towards concentrated alkaline solution owing to its superhydrophobicity, and shows good reusability in both oil/water separation and oil absorption. The influence of introduction of CNT on the mechanical and porous microstructure was examined. With 0.1 wt. % CNTs, the mechanical performance could be improved without impairing the surface properties of aerogel.

In the last part of this thesis, the findings are summarized and potential future works are suggested.

Acknowledgements

First, I wish to dedicate my sincere thanks to my supervisor Prof. Hu Xiao for his great help and inspiration during my four year's study. Prof Hu has continuously encouraged me on my study; supported me on the research and transform the way of thinking in the area of research. Without his guidance and patience, I would never learn so much during my PhD study. I thank MSE@NTU for the financial support during the last four years. I am very proud to be a student of MSE@NTU. Furthermore, I would like to extend many thanks to Dr. Liang Yen Nan for his long lasting help and deep friendship in both study and life. It seems impossible for me to forget his humorousness and kindness. His critical and valuable discussions were always beneficial to my research. I would like to thank Dr. Yin Ming, who has helped me a lot in the early days of my study, without his resourcefulness my work would not be able to have a smooth start.

I also want to thank my group members (Dr. Hu Jinhua, Dr. Liu Ming, Dr. Xu Yanping, Dr. Wang Libo, Mr Mu Chenzhong and Mr Song Yujie) for their helpful discussions, sharing of knowledge and friendship. My thanks also goes to Wilson, Sharon and Patrick, technicians in organic materials laboratory, who has help me a lot on equipment usage.

I would like to thank Mr. Hu Peng, my roommate and good friend, who has kindly helped me in my research and life.

In the end, I would like to thank my sister and my parents. Their unconditional love is the energy source of my life. It is them who help me out when I am in need. It is them who pray for me day and night. Every time when I confront severe difficulties and frustrations, my mom's smile always gives me strength.

Table of Contents

Abstract	i
Acknowledgements	iii
Table Captions	ix
Figure Captions	xi
Abbreviations	xvii
Chapter 1 Introduction	1
1.1 Background and Hypothesis	2
1.2 Objectives and Scope.....	3
1.3 Dissertation Overview	3
1.4 Findings and Outcomes	5
References	6
Chapter 2 Literature Review	7
2.1 Polymer/CNTs Composites	8
2.1.1 Mechanical Properties of Polymer/CNTs Composites	9
2.1.2 Approaches to Fabricate Polymer/CNTs Composites	12
2.2 Surface Functionalization of Carbon Nanotubes	14
2.2.1 Physical Functionalization	15
2.2.2 Chemical Functionalization	16
2.3 Materials for Oil/Water Separation.....	18
2.3.1 Hydrophobic/hydrophilic Surfaces	18

2.3.2 Polymeric Aerogel	23
2.4 Materials	25
2.5 Characterizations.....	25
2.5.1 Scanning Electron Microscopy (SEM)	25
2.5.2 Transmission Electron Microscopy (TEM)	26
2.5.3 Differential Scanning Calorimetry (DSC)	28
2.5.4 Fourier Transform Infrared Spectroscopy (FTIR)	29
2.5.5 X-ray Diffraction (XRD).....	30
2.5.6 Mechanical Test	31
2.5.7 X-ray Photoelectron Spectroscopy (XPS).....	32
2.5.8 Raman Spectroscopy	33
2.6 Summary	34
References	36
 Chapter 3 Surface Functionalization of Carbon Nanotubes.....	45
3.1 Introduction.....	46
3.2 Experiments	47
3.2.1 Air Annealing.....	47
3.2.2 Dispersion of Air-Annealed CNTs in PVDF	48
3.2.4 Characterizations.....	48
3.3 Results and Discussion	49
3.4 Conclusion	63
References	64
 Chapter 4 Mechanical Properties of PVDF/CNTs Composites	67
4.1 Introduction.....	68
4.2 Experiments	68
4.2.1 Sample Preparation	68

4.2.2 Characterizations.....	69
4.3 Results and Discussion	70
4.4 Conclusions.....	81
References.....	82
 Chapter 5 PVDF Aerogel and PVDF/CNTs Composite Aerogel for Oil/Water Separation and Fast Oil Absorption	
85	
5.1 Introduction.....	86
5.2 Experiments	87
5.2.1 Sample Preparation	87
5.2.2 Characterizations.....	88
5.3 Results and Discussion	89
5.4 Summary	106
References.....	107
 Chapter 6 Conclusions and Future Recommendations.....	
111	
6.1 Conclusions.....	112
6.2 Recommendations for Future Works	113
6.2.1 Investigation of CNTs Induced Phase Transition in Other Polymer Systems	113
6.2.2 Enhancement of the Mechanical Properties of PVDF Aerogel	114
6.2.3 Functionalize CNTs with Other Reactive Gases.....	115
6.2.4 Modeling and Simulation.....	115
References.....	117

Table Captions

Table 2.1	Mechanical properties of polymer/CNTs composites from tensile tests.	11
Table 2.2	FTIR absorption peaks of different PVDF phases.	30
Table 2.3	Standard dimension of tensile testing.	32
Table 3.1	Table 3.1 Percentages of different C and O oxidation states as determined from XPS spectra.	58
Table 5.1	Composition of water-in-oil mixture with surfactant.	88
Table 5.2	Composition of water-in-oil mixture without surfactant.	88
Table 5.3	Absorption capacity of PVDF aerogel for various oils.	97
Table 5.4	Compressive strength and modulus of each aerogel prepared from different PVDF concentrations. To enable statistical reliability, 5 samples for each concentration were tested.	101

Figure Captions

Figure 2.1	Stress–strain curves for individual MWNT.....	8
Figure 2.2	Stress-strain profiles of SWNT/nylon-6 composite fibers at different SWNT loadings. The curves are labeled with the percentage of SWNT in polymer matrix.....	10
Figure 2.3	Schematics of CNT functionalization using non-covalent methods (A: polymer wrapping; B: surfactant adsorption; C: endohedral inclusion).....	15
Figure 2.4	Surface functionalization of carbon nanotubes.....	16
Figure 2.5	Schematic illustration of droplet on different kinds of surfaces. (a) flat surface (b) Wenzel regime surface and (c) Cassie–Baxter regime surface..	19
Figure 2.6	Images showing the interaction between the coated mesh and toluene and water.	20
Figure 2.7	Removal of collection oil from water using superhydrophobic sponge.	21
Figure 2.8	a) Schematic illustration on the PAA-g-PVDF membrane b) image of an as-prepared PAA-g-PVDF membrane. c) Cross-section and d) top-view SEM images of the membrane. Images of an underwater oil droplet (e) and a water droplet on the membrane (f).	22
Figure 2.9	SEM photographs of carbon nanotubes on fracture surfaces of the composite samples: (a) with C ₁₂ EO ₈ and (b) without C ₁₂ EO ₈	26
Figure 2.10	MWCNT functionalized by HNO ₃ /H ₂ SO ₄ at 100 °C. SEM image after (a) 1 h treatment; (b) 12 h treatment and (c) 24 h treatment. Scale bars are 1 μm; TEM image after (d) 1 h treatment; (e) 12 h treatment; and (f) 12 h treatment.	27
Figure 2.11	DSC curves of PVDF with different filler loadings.	28
Figure 2.12	XRD patterns of neat PVDF.	30
Figure 2.13	XPS analyses of the MWCNTs: (a) XPS survey scan spectra; (b) variations in surface atom percentage of C1s, O1s and O/C ratio as a function of treatment durations.	33
Figure 2.14	Typical Raman spectra of MWCNTs.	34

Figure 3.1	Schematic illustration of air annealing process of CNTs and their dispersion states in organic solvent before and after treatment.	47
Figure 3.2	TGA curve of raw CNTs.....	49
Figure 3.3	TEM images of a CNT sample air annealed at 650 °C with different magnifications.....	50
Figure 3.4	The residue masses at different annealing conditions (a) and digital photographs of 1-week CNTs dispersion samples, prepared by sonicating 0.5 mg CNTs in 10 ml ethanol for 60 mins (b). Labelled on glass vials are the sample codes corresponding to different thermal functionalization conditions.....	52
Figure 3.5	TEM images of (a) raw CNTs and annealed CNTs under different conditions: (b) A4, 30min@500 °C (c) D3, 120min@450 °C and (d) B5, 60min@550 °C. The insets are enlarged images showing structural changes after thermal functionalization; in which CNT surface of sample A4 and D3 are well preserved while that of B5 is clearly damaged.....	54
Figure 3.6	Raman spectra of raw CNTs and annealed samples. (a) CNTs are annealed for 30 mins at different temperatures, (b) CNTs are annealed at 450 °C for different durations. The curves are nomalized with the G band as the reference, so the I_D/I_G values can be easily compared. The I_D/I_G values of each samples are included inside the right-hand-side brackets.	56
Figure 3.7	XPS spectra of raw CNTs, sample A4 (30mins@500°C) and A5 (30mins@550°C) (a) and deconvoluted high resolution XPS C1s spectra of raw CNTs (b1) A4 (c1) and A5 (d1); the corresponding O1s are given in (b2), (c2) and (d2), respectively. The oxygen contents for raw CNTs, A4 and A5 are calculated to be 5.53, 7.37 and 12.93 %, respectively.....	57
Figure 3.8	The proposed mechanisms of CNT surface functionalization via thermal annealing. The top part shows the formation of ether functional group, while the bottom part shows the formation of quinone group.....	60
Figure 3.9	FESEM images showing the cryo-fractured morphologies of PVDF/CNTs composites with 0.2 wt. % (a, b) raw CNT and (c, d) annealed sample D3..	61

- Figure 3.10 I-V curve of drop-cast raw CNTs and thermally functionalized CNTs (A4, 30 min@ 500°C) on ITO patterned glass. The drop volume is 10 μ L. Top-left inset shows raw CNTs (left) and air annealed CNTs (right) with different volumes (10, 20, 30 and 50 μ L) drop-cast on ITO patterned glass. Bottom right inset shows the schematic of electrical testing of drop-cast CNTs pattern. 62
- Figure 4.1 FESEM images of the cyro-fractured surface of PVDF/MWCNTs composites prepared from solution blending (A, B) and melt extrusion (C, D) with CNTs loading 0.2 wt. %. 70
- Figure 4.2 FESEM images of the cyro-fractured surface of (a) raw PVDF and PVDF/MWCNTs composites with CNTs loading of (b) 0.1 (c) 0.2 (d) 0.5 and (e) 1.0 wt. %, respectively. 71
- Figure 4.3 (a) Typical tensile test curves of neat PVDF and PVDF/CNTs composite sample with 0.2 wt. % CNTs and (b) tensile toughness improvements of composites compared with neat PVDF. 73
- Figure 4.4 USAXS scattering patterns of (a1) neat PVDF, 30 % strain; (b1) composite sample with 0.2 wt. % CNTs, 30 % strain; (a2) neat PVDF, 60 % strain; (b2) composite sample with 0.2 wt. % CNTs, 150 % strain and FESEM of necking section of (c) neat PVDF and (d) composite sample with 0.2 wt. % CNTs. To enable a clearer observation of morphological profile, both neat PVDF and composite sample are etched in oxidative solution of P_2O_5/H_2SO_4 before doing SEM. The arrows indicate the uniaxial stretching direction. 74
- Figure 4.5 Illustration of the proposed mechanism of CNT pinning effect. The breakage of neat PVDF is caused by void development and coalescence under stress, while the realigned CNTs in PVDF/CNTs composite pin and impede the coalescence of voids, delaying the failure. 76
- Figure 4.6 First heating DSC curves of PVDF/CNTs composites before (a) and after (b) tensile test and FTIR spectrum of PVDF/CNTs composites before (c) and after (d) tensile test. Curves from the bottom to top are spectrum of samples with 0, 0.1, 0.2, 0.5 and 1.0 wt. % CNT, respectively. 78

- Figure 4.7 Illustration of the proposed mechanism of polymorphic transformation-induced ductility. Under stress, the γ phase in PVDF/CNTs composite around CNTs transform into β phase, creating plasticization and resulting in enhanced ductility and toughness. 80
- Figure 5.1 (a) Schematic illustration of the formation of PVDF aerogel (b) Digital photo of different steps in fabricating PVDF aerogel. 90
- Figure 5.2 Photograph of PVDF aerogel on water with five cent Singaporean coin (diameter 16.75mm, thickness 1.22mm, mass 1.70g) on top (a) and FESEM of PVDF aerogel with different magnifications. 90
- Figure 5.3 Absorbing process of oil (a, 0.0ms; b, 16ms; c, 47ms) and contact angle of water (d). The volume of oil and water are 6 and 10 μ l, respectively. The photos are captured by the camera attached with contact angle measurement system. 91
- Figure 5.4 Optical images of oil/water mixture without surfactant before (a) and after (b) filtration and (c) filtrate purity of oil/water mixtures with various oils. The scale bar is 100 μ m. 93
- Figure 5.5 Size distribution of surfactant stabilized oil/water mixture before (a) and after (b) filtration and (c) filtrate purity of oil/water mixtures with various oils. .. 95
- Figure 5.6 Separation flux and efficiency at different separation cycles. 96
- Figure 5.7 Change of absorption weight as function of time of PVDF aerogel in dichloromethane and hexane (a) and absorption capacity as function of number of cycles in dichloromethane and hexane (b). 98
- Figure 5.8 Stress-strain curves of aerogels prepared from PVDF solutions with concentration 8, 10, 15 and 20 wt. % (a) and FESEM images of aerogel prepared from polymer loading of 8 wt. % (b), 15 wt.% (c) and 20 wt.% (d). 100
- Figure 5.9 Stress-strain curve (A) and Young's modulus as well as compression strengths (B) of PVDF aerogel and of PVDF/CNTs composite aerogel. (a) Compression strength of PVDF aerogel, 173 (66) MPa (b) compression strength of PVDF/CNTs composite aerogel, 307 (41) MPa (c) Young's modulus of PVDF aerogel, 34.7 (18.5) MPa (d) Young's modulus of

PVDF/CNTs composite aerogel, 45.4 (23.8) MPa; the value in the bracket is standard deviation.	102
Figure 5.10 FESEM (a, b), water (c) and oil (d) contact angle of PVDF/CNTs composite aerogel.....	103
Figure 5.11 Nitrogen adsorption and desorption isotherms of (A) PVDF aerogel and (B) PVDF/CNTs composite aerogel.	104

Abbreviations

PVDF	Polyvinylidene Fluoride
CNTs	Carbon Nanotubes
SEM	Scanning Electron Microscope
TEM	Transmission Electron Microscopy
TGA	Thermogravimetric Analysis
DSC	Differential Scanning Calorimetry
XRD	X-ray Diffraction
XPS	X-ray Photoelectron Spectroscopy
FTIR	Fourier Transform Infrared Spectroscopy
PS	Polystyrene
HDPE	high-Density Polyethylene
LDPE	Low-Density Polyethylene
PP	Polypropylene
PMMA	Polymethyl Methacrylate
PC	Polycarbonate
PVA	Polyvinyl Alcohol
PAN	Polyacrylonitrile
PU	Polyurethane

Chapter 1 Introduction

This chapter begins with the background and the hypothesis statement of the thesis, followed by the objectives and the scope of work. In the third section, the structure of the thesis is outlined. Main findings and promising outcomes are briefly summarized at the end of this chapter.

1.1 Background and Hypothesis

Polymer composites, combining the merits of light weight of polymer matrix and mechanical or functional properties of filler, are becoming increasingly important in our daily life and the technological fields.¹⁻⁵ Although polymer composites have been studied for a long time, the emergence of new generation of carbon based nanofillers, such as fullerene, carbon nanotube and graphene, has reanimated this research topic. Because of the unique size scales and morphology, polymer composites with these kinds of filler often display exceptional mechanical, thermal, chemical, electrical, optical and many other properties.⁶⁻⁹ For example, owing to the large aspect ratio, CNTs are superior conductive fillers compared with the traditional conducting fillers and show a much smaller electrical percolation. Furthermore, the high thermal conductivity of CNTs make them promising for thermal management applications.

Among the outstanding properties that have been realized in polymer nanofiller composites, the mechanical performance remains utmost important during practical application. Numerous works have been carried out to investigate the applications of these nanofillers in reinforcing polymer matrix, which include both thermoplastics and thermosets. Even so, the full potential of the mechanical properties of these ultra-strong nanofillers are far from being realized. Often, the reported mechanical data are inferior to the predicted values due to various reasons. Taking CNT for example, its dispersion is one of the most fundamental issues that determine the performance of the nanocomposite. CNTs are prone to aggregation due to Van der Waals force among CNT. Without an effective strategy for homogeneous dispersion of CNTs in polymer matrix, the mechanical and functional properties of composites remained non-optimal. Another common issue is the affinity between fillers and matrix. Due to the weak adhesion between the two components of composites, fillers are likely to slip or pull out, resulting in a failure in load transfer.

Furthermore, the complexity of polymer nanofiller composites not only comes from the two parent components, but also from the interphase created in the system. The interphase may have limited influence on composites at low filler content. With volume growth of interphase resulting from more filler addition, properties of composites could

be altered greatly. If the volume of interphase increases to a critical value, the interphase could become the matrix as the majority component of the composite. Therefore, a good predictability of polymer composites properties depends on accurate determinations of dispersion state, affinity, filler induced interphase and many other factors. Only when the mechanism is clearly elucidated, polymer composites with specifically tailored properties can be manufactured reproducibly.

In this work, PVDF/CNTs composites with different structures with uniform morphology were prepared by specifically designed routes. Both mechanical and functional properties of composites were investigated. To improve the dispersion of CNTs in solvents and polymers, a facile and environmental friendly approach was also employed to surface functionalize CNTs. It is hypothesized that by appropriate pretreatment and mixing strategy, CNTs could be well dispersed in PVDF to achieve enhancement of both mechanical and functional properties.

1.2 Objectives and Scope

In this work, surface functionalization of CNTs and its oxidation mechanism will be examined first and then PVDF/MWCNTs composites are prepared and studied. The objective is to develop composites with uniform morphology and investigate the influence of CNT on the composite performance, both mechanically and functionally. Studies will be focused on how CNTs alters the micro/nano structure of PVDF and the corresponding mechanical and functional properties.

1.3 Dissertation Overview

The thesis is outlined as follows:

Chapter 1 provides the outline, goals and scope of this work.

Chapter 2 reviews the literature on PVDF/CNTs composites and CNTs functionalization methods. It begins with the theoretical prediction of CNTs reinforced system in

mechanical properties, various CNTs enhanced polymeric materials and previous work on PVDF/CNTs composites. In the second section, previous works on the surface functionalization of CNTs including both physical and chemical functionalization are discussed. The third part talks about materials possessing techniques and special surface properties required for oil/water separation. Important characterization techniques and analyzing methods on PVDF and CNTs are also introduced in this chapter.

Chapter 3 introduces an environment friendly method for surface functionalization of CNTs. By thermal annealing in air at relatively low temperature range, CNTs could be functionalized with oxygen containing groups on the surface, which enables improved dispersion of CNTs in many organic solvents. The influence of temperature and annealing duration on the oxygen concentration and nature of functional groups were systematically studied. This chapter is completed with the mechanism of functionalization of CNTs with various functional groups and their potential applications.

Chapter 4 studies the influence of CNTs on mechanical performance of PVDF. With low content of CNTs loading, the ductility of PVDF was significantly enhanced. Structural change and phase transformation induced by CNTs were examined. By characterizing the phase change and structural evolution during deformation, the mechanism behind the improved ductility is proposed.

Chapter 5 presents the fabrication of PVDF aerogel with both superhydrophobicity and superoleophilicity. The porous three dimensional PVDF aerogel can effectively separate water-in-oil mixture with or without surfactant. The mechanisms of formation of PVDF aerogel and the outstanding selective oil separation property were proposed. Furthermore, CNTs reinforced PVDF aerogel was prepared and studied in terms of the microstructures, and the mechanical and the surface properties.

Chapter 6 draws conclusions for the works completed for this thesis. Additionally major contributions are highlighted and possible future works are proposed.

1.4 Findings and Outcomes

This research led to several novel outcomes:

1. Established an economical, green and effective method to functionalize CNTs.
2. Proposed CNTs oxidation mechanism in air.
3. Developed a facile method to fabricate PVDF/CNTs composite with well dispersed CNTs.
4. Illustrated the effects of CNTs on the mechanical properties of PVDF/CNTs composite via phase transformation and CNTs pinning effects.
5. Established novel method on fabricating superhydrophobic/oleophilic PVDF aerogel and CNTs/PVDF aerogel composite aerogel by vapor induced phase inversion technique.

References

- 1 Szeluga, U., Kumanek, B. & Trzebicka, B. Synergy in hybrid polymer/nanocarbon composites. A review. *Composites Part A: Applied Science and Manufacturing* **73**, 204-231 (2015).
- 2 Saba, N., Tahir, P. M. & Jawaid, M. A review on potentiality of nano filler/natural fiber filled polymer hybrid composites. *Polymers (Basel)* **6**, 2247-2273 (2014).
- 3 Pucci, A., Bizzarri, R. & Ruggeri, G. Polymer composites with smart optical properties. *Soft Matter* **7**, 3689-3700 (2011).
- 4 Barber, P. *et al.* Polymer composite and nanocomposite dielectric materials for pulse power energy storage. *Materials (Basel)* **2**, 1697-1733 (2009).
- 5 Gloria, A., De Santis, R. & Ambrosio, L. Polymer-based composite scaffolds for tissue engineering. *Journal of applied biomaterials & biomechanics: JABB* **8**, 57-67 (2009).
- 6 Hasan, T. *et al.* Nanotube-polymer composites for ultrafast photonics. *Adv. Mater* **21**, 3874-3899 (2009).
- 7 Kuilla, T. *et al.* Recent advances in graphene based polymer composites. *Prog Polym Sci* **35**, 1350-1375 (2010).
- 8 Sun, X., Sun, H., Li, H. & Peng, H. Developing polymer composite materials: carbon nanotubes or graphene? *Adv. Mater.* **25**, 5153-5176 (2013).
- 9 Thompson, B. C. & Frechet, J. M. Polymer–fullerene composite solar cells. *Angew. Chem. Int. Ed.* **47**, 58-77 (2008).

Chapter 2 Literature Review

This chapter comprises three sections. The first section reviews the mechanical properties and fabrication approaches of polymer/CNTs composites. In the second section, methods to surface functionalize CNTs are reviewed and summarized. Finally, hydrophobic/oleophilic materials and aerogel are introduced.

2.1 Polymer/CNTs Composites

As early as 4000 BC, straw has been used as filler to prepare pristine composite materials. In the past few decades, many types of fillers such as glass fiber, graphite, and carbon black, have been utilized to manufacture polymer matrix composites with huge success. Carbon nanotube, ever since its discovery about two decades ago, has been extensively explored to reinforce polymer matrix contributed by its exceptional mechanical performance. Depending on the morphology, carbon nanotube can be categorized into single walled carbon nanotube (SWCNT) and multi walled carbon nanotube (MWCNT). Both of them possess outstanding mechanical properties. Early calculations predicted that the Young's modulus of carbon nanotube to be around 1 TPa, regardless of the type or diameter of the nanotube.¹ Experimentally, mechanical property of individual MWCNT was measured by stress-strain test, giving a modulus of 0.27-0.95 TPa, elongation at break of 12 % and strength of 11-63 GPa, the mechanical performance of some tubes are plotted in Figure 2.1. SWCNT has also been tested with the same method, yielding a modulus of 0.32-1.47 TPa, elongation at break of 5.3 % and strength of 10-50 GPa.² Besides the striking mechanical performance, CNTs also possess unique optical, electrical, thermal properties, making it suitable candidate for making advanced polymer composite materials.

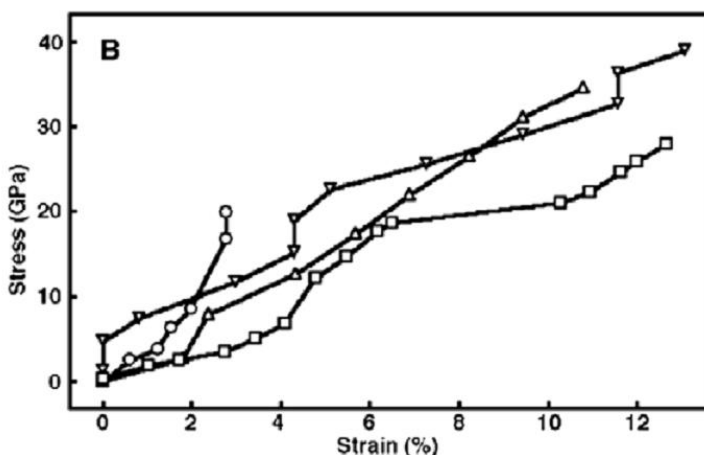


Figure 2.1 Stress-strain curves for individual MWNT.³

2.1.1 Mechanical Properties of Polymer/CNTs Composites

To effectively reinforce polymer matrix with tubular fillers, for example, carbon nanotubes and carbon fibers, several basic requirements should be met. The aspect ratio of nanofiller is primarily important. According to the well-known mixtures rules⁴, if the filler is long enough, well bonded to polymer matrix, and is equally strained as matrix in the direction of stress, the composites tensile modulus Y_c can be formulated as,

$$Y_c = (Y_f - Y_m) V_f + Y_m \quad (2.1)$$

where Y_f , Y_m and V_f are fiber modulus, matrix modulus and fiber volume fraction, respectively. The above equation illustrates a quite ideal condition that the fiber length is equivalent to specimen length. For shorter fibers, an interfacial stress transfer τ and a critical length l_c has been proposed. Under a specific interfacial stress transfer, the fiber with this critical length can be broken. For a hollow cylinder reinforcing filler, if σ_f is fiber strength, D is external fiber diameter and D_i is the internal diameter, the critical length⁵ can be formulated as,

$$l_c = \frac{\sigma_f D}{2\tau} \left[1 - \frac{D_i^2}{D^2} \right] \quad (2.2)$$

From another point of view, Cox⁶ proposed that the composites modulus can be described using a length efficiency factor η_l that,

$$Y_c = (\eta_l Y_f - Y_m) V_f + Y_m \quad (2.3)$$

Where

$$\eta_l = 1 - \frac{\text{Tanh}(a \cdot l / D)}{a \cdot l / D} \quad (2.4)$$

And,

$$a = \sqrt{\frac{-3Y_m}{2Y_f \ln V_f}} \quad (2.5)$$

As can be estimated from equation (4), the length efficiency factor is close to 1 when l/D is larger than 10 and high aspect ratio of fillers is preferred.⁷

The ability to transfer interfacial stress from matrix to filler significantly affects the mechanical performance of polymer nanocomposites. From equation (1), it can be expected that less transfer of interfacial stress will lead to a higher value of critical length. When the filler length is smaller than the critical length in system, stress cannot be

effectively transferred to the filler. As a result, the filler will be pulled out from the polymer matrix rather than being stretched to break. Under this situation, it is the matrix/filler interface strength, rather than the filler strength, that determine the composite strength. The composite strength could be described by another formulation that,

$$\sigma_c = (\ell / D - \sigma_m) V_f + \sigma_m \quad (2.6)$$

where σ_c and σ_m are the strength of composite and matrix, respectively.

In addition, nanofiller dispersion is a very important issue in preparing uniform polymer carbon nanotube composites. A good dispersion not only helps to effectively transfer load to the fillers but also leads to uniform stress distribution and stress concentration.

Modulus and ductility are the two most important parameters to assess the mechanical properties of polymer composites. Usually, after the introduction of carbon nanotubes, whether it is single-walled or multi-walled, the composites will become stiff and brittle, i.e. having an increase in modulus and decrease in ductility. The situation of simultaneous increase in modulus and ductility is rare and the case of increase in ductility but decrease in modulus is even rarer. Typical mechanical performance of successfully prepared polymer/CNTs composites displays obvious increase in modulus but certain extent of decrease in elongation at break. Shown in Figure 2.2 is the typical tensile test stress-strain result of prepared nylon 6/CNTs composites.

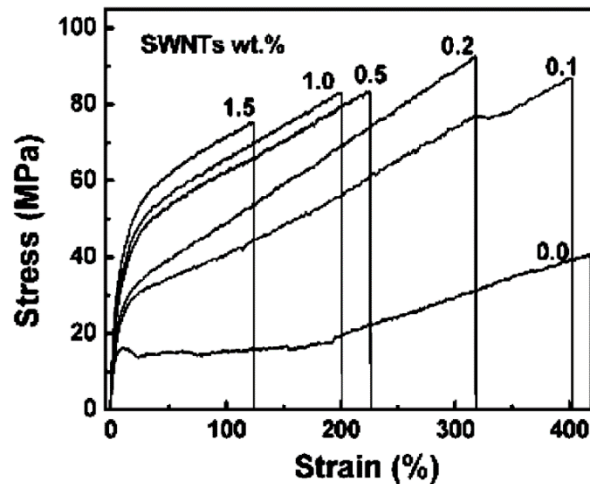


Figure 2.2 Stress-strain profiles of SWNT/nylon-6 composite fibers at different SWNT loadings. The curves are labeled with the percentage of SWNT in polymer matrix.⁸

Meinke also prepared nylon 6/MWCNTs composites, which achieved an enhancement of modulus from 1.6 to 4.2 GPa with 12.5 wt. % filler loading; however, the ductility decreased largely from 40 to 4 %.⁹ Similar work has also been done by Zhang and his collaborator who prepared nylon 6/MWCNTs composites that gave a three times increment in modulus from 0.4 to 1.24 GPa and the elongation at break decreased from 150 to 110 %.¹⁰ Polypropylene/SWNTs composites were prepared with low filler loading, modulus has been elevated from 0.85 to 1.19 GPa with CNT loading of 0.75 wt. % and the ductility was lowered from 493 to 402 %.¹¹ Sandler manufactured nylon 12/MWCNTs composite fibers with modulus of 47 MPa and ductility of 160 %; while the values of pure polymer are 22 MPa and 400 %, respectively.¹² In a previous report on poly(ethyleneimine)/CNTs composites, a large increase in modulus was attained, from 0.3 to 11 GPa, accompanied by a decrease in ductility from 4 to 1 %.¹³ Table 2.1 summarizes typical mechanical properties of representative CNTs reinforced polymers.

Table 2.1 Mechanical properties of polymer/CNTs composites from tensile tests.

Matrix	Weight %	Method	Tensile strength/ Modulus (% increase)	Strain at break (% increase)	Ref.
PS	0.50	Solution Mixing	100/100	-50	14
HDPE	1.00	Melt Extrusion	20/50	-50	15
LDPE	1.00	Melt Blending	15/70	-5	16
PP*	0.75	Shear Mixing	15/40	-17	11
PMMA	0.10	Solution Mixing	0/60	-30	17
PC	1.00	Solution Blending	15/30	-80	18
PVA	0.80	Solution Mixing	45/80	-30	19
PAN	5.00	Electrospinning	75/70	-75	20
Nylon 6	1.00	Melt Spinning	100/150	-50	8
PU	0.50	Solution Mixing	60/260	-30	21

* For PP, PVDF and nylon 6, the filler is SWCNTs, other systems are with MWCNTs.

Many studies used CNTs to reinforce PVDF to prepare high performance composite materials.²²⁻²⁵ Usually, the introduction of CNT increases modulus and tensile strength of PVDF composite at the cost of reducing the elongation at break. For instance, Amit et al. reported PVDF composites reinforced with MWCNTs (functionalized by methyl methacrylate) via a solution casting method.²² The modulus and tensile strength of the PVDF/MWCNTs composites progressively increased with the increase of CNT loading

up to 5.0 wt. %, with the elongation at break decreased by about 30%. Huang et al.²³ prepared PVDF/MWCNTs composites with 0.1 wt. % CNT, achieving an increase of modulus (from 1.46 to 1.61 GPa) and tensile strength (from 4.2 to 4.5 MPa); however, with a decrease of elongation at break from 8.5 to 7.3 %. In another study conducted by Tang et al.,²⁴ the prepared composite with 0.5 wt. % CNT loading in PVDF gained a slight enhancement in modulus and tensile strength, but the elongation at break decreased severely from 250 % of that of neat PVDF to around only 30 %. Even when metal particles were deposited onto the surface of CNT, which is claimed to be able to remarkably improve the ductility, the elongation at break could not match that of neat PVDF.²⁴ Besides PVDF, the compromise between strength/modulus and ductility is frequently required in various other polymer/CNTs systems, such as polystyrene, polyethylene, polypropylene, poly (methyl methacrylate), polycarbonate, poly (vinyl alcohol), polyacrylonitrile, polyamide, polyurethane, and epoxy.^{14, 18, 26}

Interestingly, counterintuitive results have also been documented in the system of CNT reinforced PVDF. Chang et al.²⁵ reported PVDF/MWCNTs composites with largely decreased tensile strength and Young's modulus with 3 wt. % CNTs, but with an increased elongation at break from 3.6 to 7.9%, compared with that of neat PVDF. The discrepancy among these works is partially due to different composites fabrication procedures as well as poor wetting between the fillers and highly fluorinated matrix. On the other hand, the polymorphic transformation in PVDF caused by fabrication techniques also plays important roles.

2.1.2 Approaches to Fabricate Polymer/CNTs Composites

To fully make use of advantages of CNTs in polymeric composites, it is important to ensure that carbon nanotubes are well dispersed in polymer matrix. Several approaches have been developed to facilitate the dispersion of CNTs; for instances, solution blending, melt compounding and in situ polymerization.

Solution blending is the most frequently used method to manufacture polymer/CNTs composites. The procedures of solution blending include three main steps: dispersion of nanofiller in appropriate solvent, mixing of filler and polymer matrix and evacuation of

the solvent. The main advantages of solution processing are that no complex procedures or equipment are required, and the satisfactory dispersion of filler could be obtained. Many research groups used this method to achieve good dispersion of CNTs in polymer matrix, even when the filler loading is very high.²⁷⁻³¹ In most cases, mechanical stirring, bath or probe sonication are used to aid the CNT dispersion in solvents. For example, Ruan et al.³¹ prepared polyethylene/CNTs composites by firstly dispersing CNTs in xylene with magnetic stirring and ultrasonic, followed by mixing of CNT/xylene and polyethylene/xylene. After solution casting, polyethylene/CNTs composites are obtained. Sometimes, to ensure good dispersion of CNTs in solvents, surfactants (e.g. sodium dodecylsulfate) would be used.^{32, 33} In the work of Probst et al.³², CNTs were dispersed in sodium salt of decylbenzenesulfonic acid (NaDDBS) before being added into poly(vinyl alcohol) matrix. With the help of surfactant, CNTs are fully suspended during the fabrication process. Polymer solutions instead of pure solvents have also been used to help dispersion of CNTs.^{34, 35} One problem of organic solvent processing is that it is not environmentally friendly as it uses large amount of organic solvents, which should be avoided in industrial production. Moreover, many polymers are insoluble in common organic solvents.

In contrast to solvent processing, melt processing is solvent free and has potential to be scaled up to industrial level for production of composites³⁶. Polymers can be processed with melt processing method above the glass transition temperature for amorphous polymers and above melting point for crystalline polymers. It is particularly useful for polymers that cannot be processed with solvent. Many polymer/CNTs composites with satisfactory filler dispersion have been prepared via melt processing.^{9, 10, 37-41} Due to the lacking of suitable solvents, Liu et al.¹⁰ fabricated nylon 6/CNTs composites by melt compounding nylon 6 and CNTs using twin screw mixer at 250°C with screw speed of 100 rpm. TEM shows that very good CNTs dispersion was achieved in polymer matrix. To disperse CNTs well into polymer matrix, master-batch composite with high filler loading is often used and they are mixed with calculated amount of neat polymers to obtain the final composites with specific filler loadings. In some cases, to guarantee the dispersion of filler and the uniform composition of the final composites, the combined method comprising both solution mixing and melt processing is used.^{42, 43} The melt

processing conditions need to be optimized as too high rotation speed or temperature may induce the degradation of polymer matrix. Furthermore, large shear stress during extrusion can significantly cut down the aspect ratio of CNTs.

Apart from the above two methods, in situ polymerization represents another method that has also been used to prepare polymer composites.⁴⁴ Based on this method, CNTs will firstly be dispersed in monomer solutions, followed by monomer polymerization. The merit of this strategy is that it helps the formation of strong covalent bonding between functionalized nanofiller and polymers that facilitate load transfer from macromolecules to CNTs. Another advantage is that polymer composites with higher CNTs loadings can be fabricated using this approach.

Before polymerization, CNTs are firstly functionalized by various methods to endow CNTs with functional groups that can react with the monomers. Cheng et al.⁴⁵ prepared PANI/CNTs hybrid materials via reaction of plasma treated CNTs and monomers. In this work, plasma had been used to produce reactive radical groups on the surface of nanotubes, which led to chain growth starting from the CNT surface. Nylon/CNTs hybrid material has also been fabricated by in situ polymerization. For example, Qu et al.⁴⁶ prepared nylon 6 functionalized carbon nanotubes by ring-opening polymerization of caprolactam in the presence of thionyl chloride attached carbon nanotubes.

2.2 Surface Functionalization of Carbon Nanotubes

The realization of numerous properties of CNTs in polymer depends critically on effective dispersion of the nanotubes. However, CNTs are usually entangled with each other and form an interpenetrating network, which is the main obstacle to give good dispersion. On the other hand, due to the inert chemical nature of CNT, it hardly interacts with polymer molecule and is again unfavorable to load transfer and achievement of other properties. Thus, functionalization of carbon nanotube has been adopted to address these problems. Numerous approaches have been employed to functionalize CNTs, the details can be found in several review papers.⁴⁷⁻⁴⁹ Based on the connection of introduced materials/groups with CNTs, i.e. covalent and noncovalent, CNTs functionalization can be broadly classified into two groups, namely, physical and chemical functionalization.

2.2.1 Physical Functionalization

Physical functionalization of CNTs utilizes only physical interactions without formation of covalent bonding. For example, the CNT suspension can be achieved by polymer wrapping. Gomulya et al.⁵⁰ functionalized single walled CNTs with long alkyl chain polyfluorene derivatives, making the separation and individualization of CNTs possible. Molecular dynamics simulations showed that the long alkyl tails on polyfluorenes binds strongly to the CNT walls with diversified geometries. Successful functionalization was confirmed by the high mobility functionalized CNTs based transistors. Before this study, Akazaki et al.⁵¹ managed to extract right and left handed semiconducting SWNTs, aided by a designed copolymer constituting of polyfluorene and chiral bulky moieties. The effective separation of different kinds of CNTs depends on the physical functionalization of nanotubes caused by cooperative effect between degree of chirality and polymer conformation.

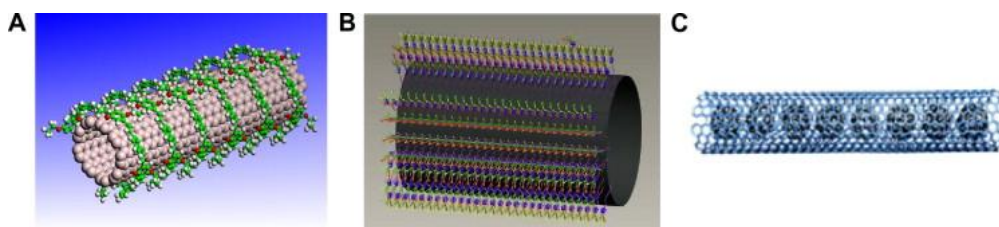


Figure 2.3 Schematics of CNT functionalization using non-covalent methods (A: polymer wrapping; B: surfactant adsorption; C: endohedral inclusion).⁵²

Various surfactants have been used to physically functionalize CNTs, such as non-ionic surfactants, anionic surfactants and cationic surfactants.⁵³⁻⁵⁷ It is believed that the application of surfactant on CNTs reduce the surface tension, thus blocking aggregations. In addition, surfactant functionalized CNTs helped suppress the Van der Waals interactions between tubes, contributing to their good dispersion. Endohedral inclusion of guest atoms/molecules in CNTs is also one of the physical methods to functionalize CNT. This methodology is based on the assumption that guest atoms/molecules can be inserted into the inner tubes via capillary effect.⁵⁸ The hybrid materials fabricated via this

approach effectively integrate properties of two original ingredients. The main physical functionalization approaches are illustrated in Figure 2.3.

Physical functionalization is advantageous in some aspects. The most important one is that the CNT crystalline structure is not impaired during the functionalization process, which helps to conserve the intrinsic properties of CNTs. Secondly, although in some cases the synthesis of guest molecules is far from simple, physical functionalization process itself is not complicated compared to chemical functionalization method; which will be discussed in the next section.

2.2.2 Chemical Functionalization

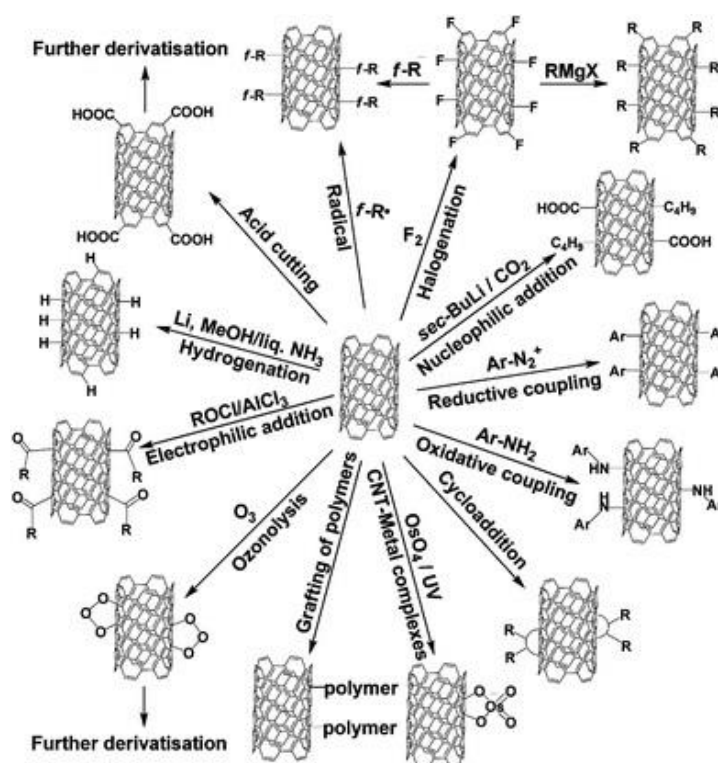


Figure 2.4 Surface functionalization of carbon nanotubes.⁵⁹

By chemical functionalization, CNTs are functionalized/linked with other atoms or molecules with covalent bonding. Following the formation of covalent bonds, nanotube structures are disrupted, resulting in the transformation of sp^2 to sp^3 of carbon atoms. Since CNTs are structurally stable and inert, the first step of chemical functionalization of CNTs usually involves strong oxidants or corrosive chemicals, such as concentrated acids,

radicals and etc. The mixture of acids comprising of nitric and sulfuric acids with specific ratio are frequently used as chemical functionalization agents. The treatment with mixed acids introduce large amount of carboxylic and hydroxyl groups onto CNTs, which helps to enhance CNT dispersability in various polar organic solvents and aqueous medium. Building on the foundation of abundant chemistries involving COOH and OH, CNTs with these groups are easy to be further functionalized via methods such as acylation or esterification. Masahito Sano⁶⁰ fabricated an interesting CNTs ring by firstly oxidizing CNTs with HNO₃/H₂SO₄ and then reacting them with 1,3- dicyclohexylcarbodiimide (DCC). It was believed that the CNTs, after acid oxidation, possess abundant carboxylic acid groups at the two ends of nanotubes. With the presence of DCC, COOH at two ends underwent condensation reaction and form anhydride. Note that oxidation using concentrated acids is very detrimental to CNT structure. Therefore, it is crucial to carefully control the reaction durations and temperature to avoid extensive disruption to CNT properties. Shin⁶¹ studied the influence of reaction time on the structure of CNTs and found that after 12 h treatment with strong acids, most of the CNTs turned into amorphous carbon. Traditional method that uses liquid phase acid to boil CNTs usually requires excess amount of acid, and the required subsequent washing step to remove residual acid is also tedious, which limits its large scale industrial production. To tackle these problems, Ming et al.⁶² modified this approach using acid vapor under high temperature and pressure rather than liquid acids. Under this condition, the nitric acid vapor is highly efficient in oxidizing CNTs. Results showed that as little as 0.5 ml concentrated nitric acid was sufficient to functionalize one gram of CNTs, largely reducing the required acid dosage compared to conventional method. The reduced amount of acid also simplifies the subsequent washing step.

Contributed by its high reactivity, different radicals have also been used to chemically functionalize CNTs; and were proved to be feasible.⁶³⁻⁶⁸ For example, by heating succinic or glutaric acid acyl peroxides, radicals can be generated and they can attack CNTs in situ.⁶⁹ CNT functionalization were also achieved by the photolysis of perfluoroazooctane wherein perfluorooctyl radicals are generated, resulting in perfluorooctyl functional groups which are attached on the sidewall of CNTs.⁷⁰ Apart from strong acids and

radicals, many other chemical agents have also been used to functionalize CNTs.⁷¹⁻⁸³ A summary of CNT chemical functionalization is provided in Figure 2.4.

2.3 Materials for Oil/Water Separation

Industrial waste water from petrochemical, textile, leather, steel and food manufacturing contains excessive amount of oil and many other hazardous materials, which poses a real and serious threat to both human beings and environment.^{84, 85} Historically, oil spillage events have taken place and gave huge and lasting effects to the surrounding biosphere. For instance, the BP oil disaster occurred in April 2010 discharged 4.9 million barrels of oil into Gulf of Mexico, even more than during Ixtoc I oil spill which is also considered as one of the largest oil spill in the history.⁸⁶ To tackle this issue, novel materials that can selectively absorb water (oil) and/or repel oil (water) are highly desirable.

2.3.1 Hydrophobic/hydrophilic Surfaces

Materials that can successfully separate oil and water are either hydrophobic/oleophilic or underwater oleophobic. The wettability of material is determined by two main factors, surface free energy (surface tension) and microstructure of the surface (roughness). Materials with higher surface free energy are easily wetted by liquid, such as glass and metals. Polymers usually have low surface free energy between 25 and 100 mJ/m², making them more difficult to be wetted. Introduction of other elements into polymer alters the surface free energy. For example, the replacement of hydrogen by fluorine in aliphatic polymers reduces the surface tension while some other elements, such as nitrogen, oxygen, iodine, bromine and chlorine enhance it.

The state of a drop of liquid on the flat surface (Figure 2.5a) can be described by Young's equation:

$$\gamma_{SV} = \gamma_{SL} + \gamma_{LV} \cos\theta \quad (2.7)$$

$$\cos\theta = \frac{\gamma_{SV} - \gamma_{SL}}{\gamma_{LV}} \quad (2.8)$$

where γ_{SV} , γ_{SL} and γ_{LV} are respectively surface tension of solid-vapor, solid-liquid and liquid-vapor interface. The lower the theta value, the better is the wettability. When $\theta =$

0° , liquid is spread out completely on the surface; when $\theta = 180^\circ$, liquid is completely repelled and form sphere on the surface.

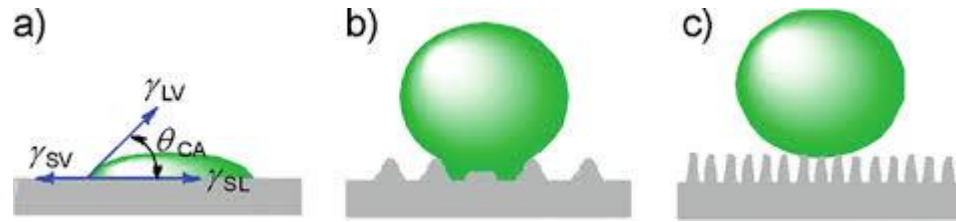


Figure 2.5 Schematic illustration of droplet on different kinds of surfaces. (a) flat surface (b) Wenzel regime surface and (c) Cassie–Baxter regime surface.⁸⁴

To describe the drop on rough surface, Wenzel proposed the Wenzel equation (Figure 2.5b)⁸⁷:

$$\cos \theta_r = r \frac{\gamma_{SV} - \gamma_{SL}}{\gamma_{LV}} \quad (2.9)$$

where r is the roughness ratio, defined as the ratio of true area of the solid surface been wetted to the apparent area. Wenzel equation indicates that on rough surface, the real solid-liquid interfacial area is larger than the apparent area, enhancing the actual hydrophobicity or hydrophilicity. That is, when $\theta < 90^\circ$, θ_r decreases as roughness increases, the surface is easier to be wetted; when $\theta > 90^\circ$, θ_r increases as roughness increases, the surface is more difficult to be wetted.

Cassie and Baxter developed Wenzel's theory illustrating the condition that the liquid cannot fully wet the solid surface with vapor still trapped inside (Figure 2.5c).⁸⁸ This frequently occurs when the surface is coved by micro or nano protrusions. They hypothesized that the surface cannot be wetted solely by liquid made of two different materials with fraction f_1 and f_2 . So,

$$\cos \theta_r = f_1 \cos \theta_1 + f_2 \cos \theta_2 \quad (2.10)$$

where θ_1 and θ_2 are material 1 and 2 while $f_1 + f_2 = 1$. This equation is also applicable to porous materials, for which the real surface of solid consists of solid and air. In this case, water droplet cannot completely fill in all the pores on the surface, leaving large amount of air trapped in the cavities. Thus, the apparent interfacial surface area is actually covered by both solid and air.

Since the contact angle (θ_2) between air and water is 180° , the above equations can be rewrite as:

$$\cos \theta_r = f_1 \cos \theta_1 - f_2 \quad (2.11)$$

According to Young's equation, if the surface free energy of solid is between that of water and oil, the solid surface may exhibit both hydrophobic and oleophilic properties. From Wenzel's equation, superhydrophobicity and superoleophilicity can be achieved by proper manipulation of the surface roughness.

In early studies on hydrophobic/oleophilic materials, metal meshes with pores have been used as the skeleton. After surface functionalization, usually by polymer coating, superhydrophobicity and superoleophilicity could be achieved on metal structures. For example, Wang et al.⁸⁹ fabricated superhydrophobic TPU film covered on copper mesh for oil/water separation. First, fibrous TPU with bead on the fibers were electrospun on the copper mesh collector. After functionalized with hydrophobic nanosilicas, the film becomes superhydrophobic. Test shows that this TPU porous film can successfully separate water/oleic acid mixture. Feng et al.⁹⁰ described a spray and dry method to prepare PTFE on stainless steel film exhibiting both superhydrophobicity and superoleophilicity. A 156° contact angle and 4° sliding angle of water were achieved. Furthermore, the coating film possessed high hardness. It was believed that the unique coated PTFE structure contributed to these properties. This film was efficient in separating diesel/water mixture.

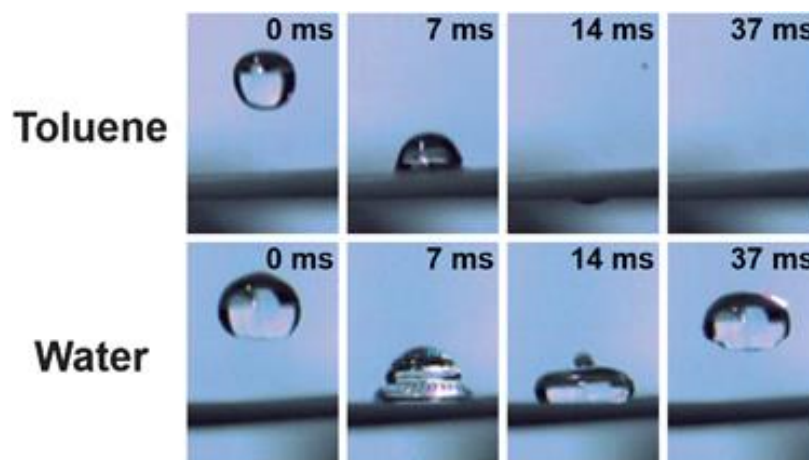


Figure 2.6 Images showing the interaction between the coated mesh and toluene and water.⁹¹

Colin et al.⁹¹ fabricated superhydrophobic copper mesh with water contact angle between 152 and 167° by coating rough silicone elastomer on the copper surface. By capturing using ultra-high speed video, they observed that toluene droplet could penetrate the film very quickly while the water droplet bounce back, see Figure 2.6. The designed filtration system can separate hexane, petroleum ether and toluene from water efficiently.

Except metal meshes, textiles, such as polyester textile and cotton fibers, can also be used for separation applications.⁹²⁻⁹⁷ Compared with metals, textile materials have advantages of low price and better flexibility. They also show high stability under conditions of high temperature, high humidity, corrosive solutions or mechanical abrasion.

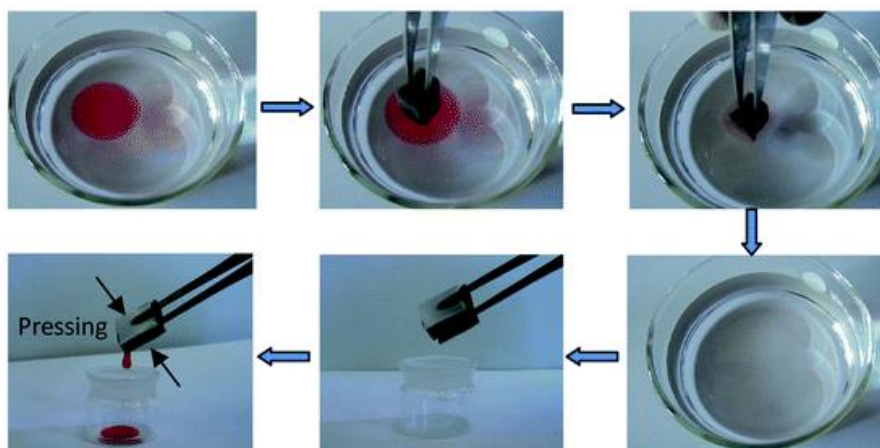


Figure 2.7 Removal of collection oil from water using superhydrophobic sponge.⁹⁸

Three dimensional porous materials with high elasticity, high absorbing and large surface area have also been used for the oil/water separation. Zhu et al.⁹⁸ fabricated superhydrophobic polyurethane sponge by coating one layer of superhydrophobic polysiloxane on polyurethane sponge via a facile solution immersion method. The sponge exhibits superhydrophobicity with the polymer coating and selectively absorbed oil with high capacity from the water surface, shown in Figure 2.7. The oil can be recovered by simply squeezing the sponge. Furthermore, this kind of sponge is mechanically stable, thus enabling reusability. Similar strategy to fabricate three dimensional porous materials was also employed in other studies.⁹⁹⁻¹⁰²

To remove oil from emulsions with droplet size as low as several micrometers or even nanometers, filtration system with very small pores is necessary. Zhang et al.⁸⁵ prepared a superhydrophobic/superoleophilic PVDF membrane via a modified phase inversion process. Because of the unique partially connected spherical nanoparticles, the membrane was able to separate both surfactant free oil/water mixture and surfactant stabilized emulsions with high flux.

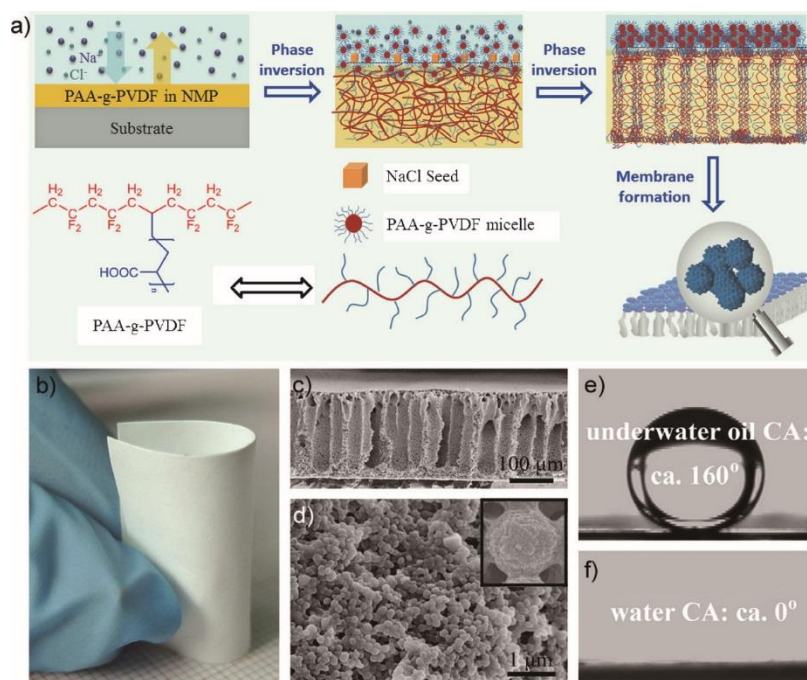


Figure 2.8 a) Schematic illustration on the PAA-g-PVDF membrane b) image of an as-prepared PAA-g-PVDF membrane. c) Cross-section and d) top-view SEM images of the membrane. Images of an underwater oil droplet (e) and a water droplet on the membrane (f).¹⁰³

Except from superhydrophobic/superoleophilic surfaces, underwater superoleophobic materials can also be employed for oil/water separation.¹⁰⁴⁻¹⁰⁷ Compared with superhydrophobic/superoleophilic materials, the superoleophobic materials have the additional advantageous of antifouling from oils. Jin and coworkers¹⁰³ reported the preparation of superhydrophilic and underwater superoleophobic PVDF membrane. PVDF molecules were first grafted with PAA, followed by a phase inversion processes of the copolymer. The product was spherical particles with a skin layer composed of PAA

extending outward, thus displaying both superhydrophobicity and underwater superoleophobicity. The fabricated membrane was capable of separating oil from water in both surfactant free and surfactant stabilized oil-in-water emulsions.

2.3.2 Polymeric Aerogel

As one kind of solid materials, aerogel is unique in many aspects. In fact, aerogel has been considered as a new state of matter, on top of solid, liquid and gas.¹⁰⁸ According to IUPAC, aerogel is a gel comprised of a microporous solid within which the dispersed phase is a gas. The definition of aerogel is evolving during the last century since the first invention of this type of interesting porous materials.¹⁰⁹ This is because of the fact that many new forms of aerogel have been discovered and new features relating to all aspects of this material are taken into account. Initially, it was thought that aerogels can only be made from the sol-gel process. However, recent report on preparing CNT aerogel demonstrated that sol-gel process can also be avoidable.¹¹⁰ In spite of the difficulty to give a universally accepted definition, all these aerogels have some common material characteristics. Structurally, all aerogels are gel-like with hierarchical structure and pores. Aerogels have different properties compared with that of their bulk form, (regardless in solid, liquid or gas form) such as low thermal conductivity, high sound insulation, high surface area, and so on. For example, SiO₂ aerogel can be as transparent as glass, thermally conductive as polystyrene and with large surface area as that of charcoal.¹¹¹ Contributed by the many unique properties of aerogels, they have found extensive applications in supercapacitor¹¹², buildings^{113, 114}, drug delivery¹¹⁵, energy applications¹¹⁶ etc.

Generally, the fabrication of aerogels consists of three steps: (i) solution-sol transition, (ii) sol-gel transition (gelation) and (iii) gel-aerogel transition (drying). For drying methods, supercritical drying, freeze drying and ambient drying are frequently employed.^{111, 117} In freeze drying, the liquid is firstly frozen, followed by sublimation, which avoids the liquid/gas boundaries. This economical method is easy to operate and environmentally friendly; hence many aerogels have been prepared using freeze-drying.¹¹⁸⁻¹²⁰

From the perspective of composition, aerogels can be classified into single-component aerogels and composite aerogels. Single-component aerogels mainly include oxide aerogels, organic aerogels, carbon aerogels and chalcogenide aerogels; while composite aerogels mainly include multi-composition, micro/nano composite and gradient aerogels. Oxide aerogels have been studied since the very beginning and are most thoroughly investigated. For oxide aerogels, many commercial applications have been proposed or employed.¹²¹ However, these aerogels are mechanically brittle, preventing them from more practical applications. As a result, stronger polymeric aerogels with many interesting properties increasingly gain attention in recent years. Generally, polymeric aerogels are aerogels with polymeric framework. In a typical sol-gel process involved in fabricating inorganic aerogel, the molecular precursors are transformed into cross linked structure before drying, leaving behind solid porous structures. Similarly, polymeric aerogel are obtained either by polymerizing monomers into cross linked network or transformation from liquid to solid phase aided by physical phase inversion.^{116, 122} For example, by cross linking polyamic acid with triamine, polyamide gel could be obtained.¹²³ Graphene/PVDF organogel was obtained by mixing PVDF and graphene in DMF/water solution followed by heat treatment at 160 °C, before cooling to room temperature. After solution exchange in water and drying process, PVDF aerogel could be obtained.¹²⁴

To optimize various material properties of polymeric aerogels, such as mechanical properties, electrical and thermal properties, many types of fillers have been used. By incorporating carbon nanofiber (CNF) into polyvinyl alcohol (PVA) aerogel,¹²⁵ both storage modulus and loss modulus of the pure polymer aerogel can be enhanced, indicating successful reinforcement. Simultaneously, the introduction of CNF also reduces thermal conductivity and surface area. Cellulose/graphene oxide aerogel were also prepared,¹²⁶ the results showed that with 0.1 wt. % graphene oxide, the compression strength and Young's modulus were increased by 30 and 90%, respectively. Qi et al.¹²⁷ fabricated electrically conductive cellulose with conductivity as high as $2.2 \times 10^2 \text{ S cm}^{-1}$, with 10 wt. % CNTs loading. The Young's modulus can reach approximately 90 MPa. Wang et al.¹²⁸ also prepared cellulose/CNTs aerogel, achieving an improvement in compression strength by 25 % with 10 wt. % CNT loading.

2.4 Materials

Poly (vinylidene fluoride) (PVDF) powder was purchased from Alfa Aesar and multi-walled carbon nanotubes with average diameter of 10 nm and average length of 1.5 μm was purchased from Nanocyl, Belgium. The surface area is 250-300 m^2/g . Sulfuric acid with concentration 95-97% and nitric acid with concentration 69-70% were purchased from Honeywell. Analytical grade ethanol, acetone, chloroform and N, N-Dimethylformamide (DMF) and hexane were purchased from Sigma Aldrich. HPLC grade toluene and analytical grade cyclohexane were bought from Merck. HPLC grade chlorobenzene was bought from Alfa Aesar; dichloromethane and dimethyl sulfoxide (DMSO) was purchased from TEDIA. The FuelSave 95 gasoline and diesel were purchased from Shell.

2.5 Characterizations

2.5.1 Scanning Electron Microscopy (SEM)

Compared with optical microscopy, SEM has a higher contrast and observation field size and it is the most direct evidence of material micro- or nano- structure. The surface topology and composition information of materials can be obtained from SEM images. Principally, SEM produces the image by collecting the electrons from the surface atoms during the interaction of the sample with electron beams. Three main signals generated include secondary electrons, back-scattered electrons and characteristic X-rays. In most cases during SEM imaging, the secondary electron imaging (SEI) was created by collecting the secondary electrons. SEI can have a very high resolution, making the observation of structure down to 1 nm possible. Additionally, back-scattered electrons imaging and characteristic X-rays can be used to identify the distribution and abundance of different elements in the samples.

SEM has been frequently used to examine the morphology of polymer nanocomposites. Figure 2.9 shows a SEM image of polymer/CNTs composites with and without the surfactant. It is clearly observed from Figure 2.9 (a) that in the presence of surfactant,

excellent CNT dispersion was achieved. Figure 2.9 (b) shows that CNTs without surfactant is prone to aggregate.

To obtain high quality SEM images, the samples are supposed to be electrically conductive to prevent electron induced charging. Since CNTs are high in electrical conductivity, good SEM images of pure CNTs samples can be obtained, especially when the CNTs are on conductive substrates. However, when it comes to polymer composite, it is necessary to perform a gold or platinum coating before the SEM operation, due to the nonconductive nature of most polymers. As a result of the surface coating, the nano fillers under SEM are larger than their real size. To examine the morphology of polymer composites, such as CNT distribution or dispersion, a fractured surface is normally observed. For polymers with glass transition temperature below room temperature, cryo-fracture in liquid nitrogen is necessary to prevent any stress induced morphology transformation.

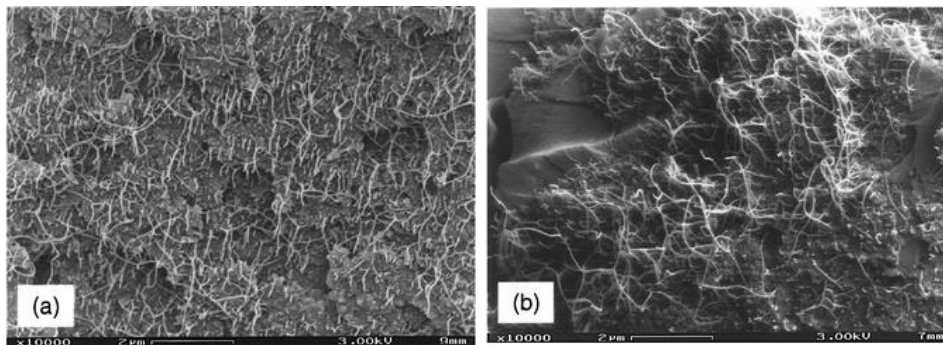


Figure 2.9 SEM photographs of carbon nanotubes on fracture surfaces of the composite samples: (a) with $C_{12}EO_8$ and (b) without $C_{12}EO_8$.¹²⁹

2.5.2 Transmission Electron Microscopy (TEM)

Similar to SEM, transmission electron microscopy (TEM) also generates images after the beam electrons interact with samples. The difference is that the sample is thin enough for the beam electrons to pass through. The interaction with sample atoms leads to the change of beam electron directions according to a scattering angle that is depending on the density and thickness of samples. TEM Image with different brightness could be generated by collecting the scattering signals. Different from SEM, surface coating is not

required for TEM. However, due to the weak penetrability of beam electrons, the thickness of sample must be very thin, preferably around 50 to 100 nm. Polymeric samples are usually needed to be sectioned by microtome or cryo-microtome (for polymers with glass transition temperature below room temperature). Furthermore, because of the fragile nature of polymeric and biological samples, low working voltage and short focusing/imaging process is recommended. High voltage and long retention of electron beam can damage the sample.

Compared with SEM, TEM has much higher magnification. TEM has high resolution down to 0.1 to 0.2 nanometer, making the investigation of small structures composing of only a row of atoms possible. More importantly, inner structure and crystalline lattice can be observed with TEM, which SEM is not capable of. Figure 2.10 shows the difference between SEM and TEM in probing the influence of oxidation time on the structure transformation of CNTs. With SEM it is seen with the extension of reaction time, CNTs adhere to each other and become mud-like. Meanwhile, TEM shows more amorphous carbon is created with the increase of oxidation time. Both SEM and TEM can be employed to study the CNT dispersion in various polymer matrices. Actually, SEM and TEM are usually used together to fully characterize the sample morphology and interfaces.

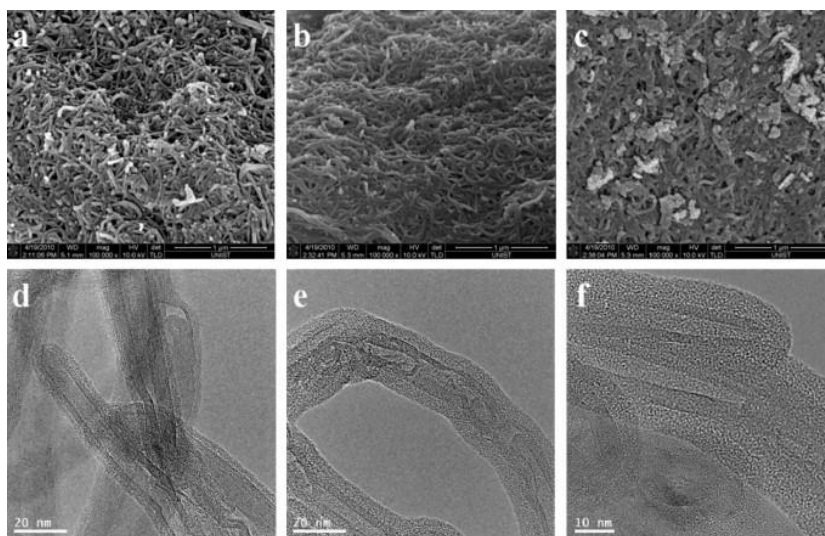


Figure 2.10 MWCNT functionalized by $\text{HNO}_3/\text{H}_2\text{SO}_4$ at 100 °C. SEM image after (a) 1 h treatment; (b) 12 h treatment and (c) 24 h treatment. Scale bars are 1 μm ; TEM image after (d) 1 h treatment; (e) 12 h treatment; and (f) 12 h treatment.⁶¹

2.5.3 Differential Scanning Calorimetry (DSC)

Differential Scanning Calorimetry (DSC) is a frequently used thermal analytical technique to study polymer materials. It measures the difference in heat flow between the sample and reference, as a function of time. During heating, the heat difference will be compensated by the heating wire that located under both the reference and sample cells. By recording the heating power difference of two heating wire, DSC curves could be obtained. Typical DSC curves have y axis of endothermic or endothermic rate and x axis of temperature or time. Many thermodynamic or kinetic parameters, such as specific heat capacity, reaction heat, phase transition heat, phase diagram, reaction and crystallization rate, crystallinity in polymers and material purities can be measured. DSC has wide measurement range and requires very little amount of samples.

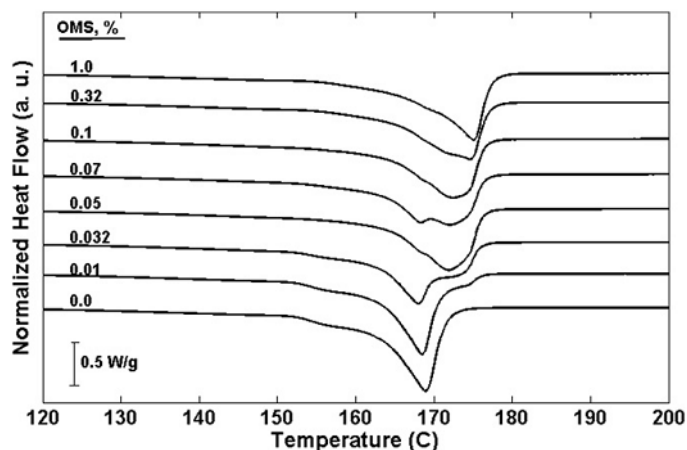


Figure 2.11 DSC curves of PVDF with different filler loadings.¹³⁰

DSC has been used to determine the glass transition temperature for amorphous polymers and melting/crystallization temperatures for semi-crystalline polymers. Three peaks are frequently seen in DSC curves for PVDF. As shown in Figure 2.11, the peak around 150 °C results from imperfect crystals, and the melting of gamma phase PVDF leads to a peak around or slightly above 170 °C that depends on molecular weight of the PVDF used.¹³⁰ Many publications have mistakenly assigned the γ peak to β phase fusion¹³¹. Ince-Gunduz and Gregorio have explained the origin and evolution of this mistake^{130, 132}. In

fact, the melting peaks of α and β phase PVDF are overlapped in DSC, which is several degrees lower than that of γ phase.

2.5.4 Fourier Transform Infrared Spectroscopy (FTIR)

Fourier Transform Infrared Spectroscopy (FTIR) is a technique that collects the infrared spectrum of samples. When molecules are exposed to infrared light, if the radiation energy is equivalent to the energy difference between the ground state and the excited state of sample, the sample molecules can absorb the radiation energy and transit to the excited vibration. The absorption of energy leads to the reduction of radiation intensity, which can be detected and recorded to give the FTIR spectrum after a series of mathematical calculation. Both stretching vibration and bending vibration of molecules can be detected, which comprises of symmetric stretching vibration, asymmetric stretching vibration, in-plane bending vibration and out-of-plane bending vibration. The common wave length used in in FTIR is between 2.5~25 μm , corresponding to 4000~400 cm^{-1} in FITR spectrum.

FTIR is a useful tool to investigate different crystals in PVDF. α , β and γ phases of PVDF, each one has its own characteristic peaks in FTIR. A list of absorption peaks for different crystals^{130, 132-134} is provided in Table 2.2. It is noted that both peaks at 840 and 1234 cm^{-1} are observed for both β and γ phases. In addition, the peak of β at 510 cm^{-1} and the peak of γ at 512 cm^{-1} are very close to each other. Confusion could arise if these two peaks are not examined carefully. The β phase is important since it is responsible for the piezoelectricity; it is required to obtain the weight percentage of this phase in many cases. The β phase fraction can be calculated according to the following equation:

$$F(\beta) = \frac{A_{\beta}}{1.26A_{\alpha} + A_{\beta}} \quad (2.12)$$

where A_{α} and A_{β} are adsorption bands of α and β at 532 and 840 cm^{-1} , respectively.

Table 2.2 FTIR absorption peaks of different PVDF phases.

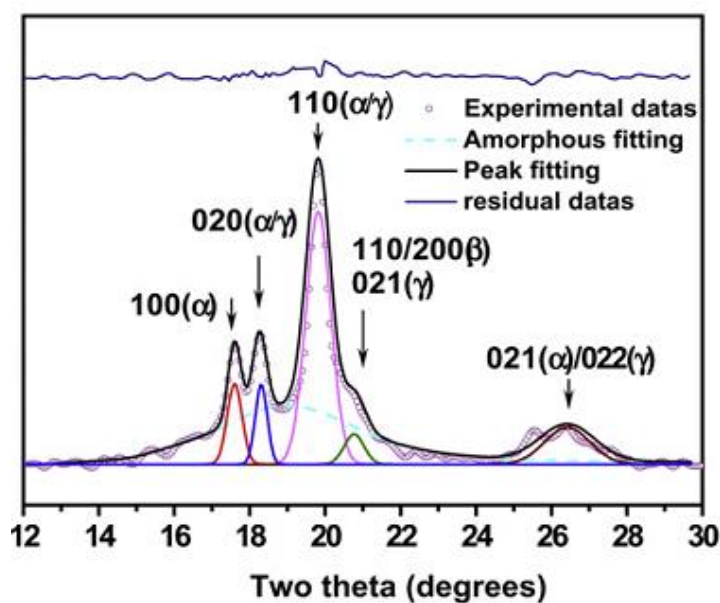
Phase	Peak Wavenumber (cm ⁻¹)
α	408, 532, 614, 764, 796, 855, 976
β	445, 510, 840, 1234
γ	431, 512, 776, 812, 833, 840, 1117, 1234

2.5.5 X-ray Diffraction (XRD)

The structure of crystalline materials can be studied by X-ray Diffraction (XRD). Since crystals are composed of unit cell which is a set of atoms with regular arrangement, when the distance between atoms has the same magnitude as the wavelength of the incident beam of X-ray, the scattered X-ray interfere with each other as they leave the crystal. The interference intensity of X-ray in a specific direction is closely related to the crystal structures. Therefore, the X-ray pattern reveals the inner atom arrangement of the materials. The lattice spacing and the wavelength of incident beam is described by Bragg's Law,

$$2d \sin\theta = n\lambda \quad (2.13)$$

where d and λ are the distance between atomic layers and wavelength of incident X-ray beam, respectively. θ is the complement angle of incident angle and n is an integer.

**Figure 2.12** XRD patterns of neat PVDF.¹³⁵

XRD has been used to determine the polymorphism of PVDF. Figure 2.12 shows a typical XRD pattern of pure PVDF,¹³⁵ in which the peak at 17.6° belongs to α phase crystal, peaks at 18.5, 20.1 and 25.6 are attributed to α/γ phases and the peak around 20.5 to 22° may come from the combination of polar β and γ phases, respectively. The determinations of each crystal are slightly different among the literature. For example, Gregorio et al.¹³² claimed that the peak of around 17.6° is common to both α and γ phases while the peak at 20.26° is exclusively originated from β crystal. The difference is due to the fact that the peaks of each crystal are very close to each other and overlap in some cases. Besides, the crystallization of γ phase often leads to the formation of α crystal and makes the differentiation of γ and α crystal characteristic peak impossible.

2.5.6 Mechanical Test

The mechanical performance of PVDF and its CNT composites are examined by tension and compression testing. During tensile testing, the sample is subjected to a controlled tension force until it fails by fracture. Ultimate tensile strength, elongation at break, Young's modulus and yield strength can be obtained by tensile testing. By calculating the strain ε and stress σ according to the following equations, a stress-strain curve is given during the testing:

$$\varepsilon = \frac{\Delta L}{L_0} = \frac{L - L_0}{L_0} \quad (2.14)$$

$$\sigma = \frac{F_n}{A} \quad (2.15)$$

where L_0 is the initial length, L is the final length and ΔL is the change in length. F is the tensile force and A is the cross-sectional area of the specimen.

Uniaxial tensile testing is applicable to isotropic materials, while biaxial tensile testing is usually needed to test anisotropic materials, such as many composites systems. Because CNTs are well dispersed in the polymer matrix, sample prepared in this work can be considered as isotropic materials.

The samples for tensile test are prepared following standardized geometry, which has two shoulders at two ends and a gauge in between. The dimension of the sample tested in this work is based on the ASTM D638-V and listed in the table below:

Table 2.3 Standard dimension of tensile testing.

Measured Parts	Standard (mm)
Width of Narrow Section	3.18
Length of Narrow Section	9.53
Width Overall	9.53
Length Overall	63.50

During compression testing, the samples are subjected to compressive force. Similar to tensile testing, a stress-strain curve will be plotted during testing. Besides that, the compression strength and Young's modulus could be calculated. The samples tested by compression testing have a column shape with diameter 42 mm and height around 3.6~3.8 mm. At least five samples are tested for each composition to guarantee the reliability of the statistical value. The universal testing machine is used to perform both the tensile and compression testing.

2.5.7 X-ray Photoelectron Spectroscopy (XPS)

X-ray photoelectron spectroscopy (XPS) is a technique used to analyze the material at 0 to 10 nanometers from the surface. The principle of XPS is based on the photoelectric effect. That is, electrons can be emitted upon the exposure to light. In XPS, the X-ray beam irradiates the material; by collecting the data of kinetic energies and numbers of emitted electrons, XPS spectrum could be obtained. The binding energy of material can be calculated from the following equation:

$$E_{\text{binding}} = E_{\text{photon}} - (E_{\text{kinetic}} + \phi) \quad (2.16)$$

where E_{binding} , E_{photon} and E_{kinetic} are binding energy, X-ray photon energy and kinetic energy of emitted electrons, respectively. ϕ is a parameter related to spectrometer and sample material.

XPS can provide information about the elemental composition and concentration of compounds, chemical state, molecular structure and chemical bonding. Since X-ray beam only penetrates very thin top layer of material surface, XPS can be regarded as a non-destructive technique.

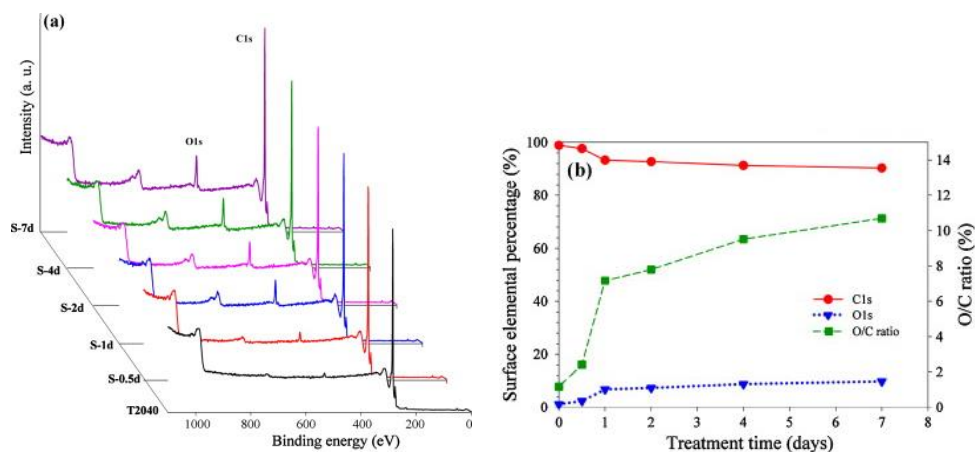


Figure 2.13 XPS analyses of the MWCNTs: (a) XPS survey scan spectra; (b) variations in surface atom percentage of C1s, O1s and O/C ratio as a function of treatment durations.¹³⁶

The elemental composition change during functionalization of CNTs can be studied by XPS. XPS is commonly used to investigate the electronic structure and functional groups of various carbon materials, such as graphene oxide¹³⁷⁻¹⁴¹ or carbon nanotubes¹⁴²⁻¹⁴⁶. The functionalization of CNTs usually introduces new elements to the CNTs and this could be monitored by XPS. The compositional variations caused by different acid treatment times are illustrated in the XPS profile in Figure 2.13(a). As seen, the oxygen peak increases with increased reaction durations. The percentage of carbon, oxygen and carbon/oxygen ratio can also be calculated from the XPS, which is summarized in Figure 2.13 (b). From high resolution XPS spectra, elements with different binding energies can also be differentiated, from which the percentage of various groups can be obtained.¹⁴⁵

2.5.8 Raman Spectroscopy

Raman spectroscopy is a useful tool to characterize crystalline and electronic structure of carbon nanotubes. When incident light radiates on the sample, scattered light is produced. Most of the scattered light has the same frequency as the radiation source, which is known as elastic scattering or Rayleigh scattering. Due to the interaction between the incident light and molecules, a small fraction of the scattered light shifted in energy and frequency, which is called inelastic scattering or Raman scattering. Raman spectroscopy collects information of molecular vibration and rotation through inelastic scattering. By

plotting the scattered light intensity as a function of the energy difference between incident photon and Raman scattered photon, which is also equivalent to the molecular vibrational energy, the Raman spectrum is obtained.

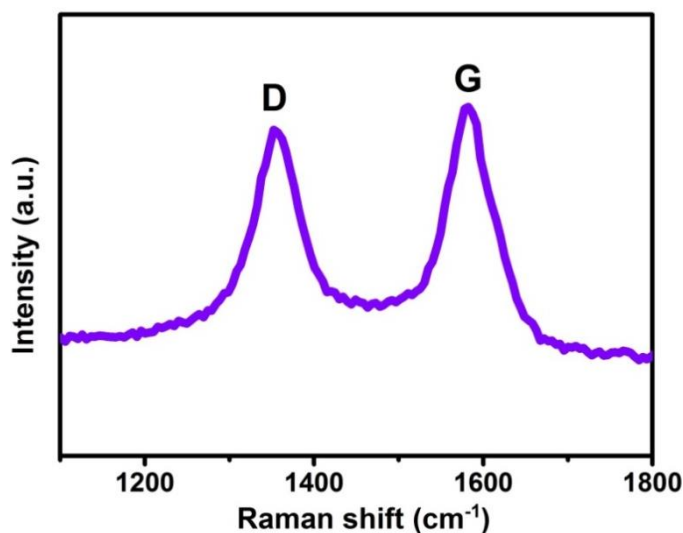


Figure 2.14 Typical Raman spectra of MWCNTs.

Figure 2.14 is a typical Raman spectrum of MWCNTs. The D band around 1350 cm^{-1} is a disorder induced band. Acid oxidation or other chemical functionalization that modify CNT structure may increase this band. Besides, this band is also sensitive to amorphous carbon on CNT surface.¹⁴⁷ The second band around 1580 cm^{-1} is related to the sp^2 carbon of CNTs. The intensity ratio of D to G peak I_D/I_G that dividing the band area or height of D band over G band is usually used to analyze the structures. I_D/I_G is found to increase as more defects exist in the CNTs.^{61, 148}

2.6 Summary

CNTs have been widely used to reinforce various polymers. The usually seen phenomenon with the introduction of CNTs is the enhancement of modulus and yield strength and simultaneous suppression in ductility. Generally speaking, there are three different strategies to fabricate polymer/CNTs composites: solvent blending, melt compounding and in situ polymerization. Most of the previous works on PVDF/CNTs

composites required tedious surface functionalization of the CNTs; and limited enhancement of mechanical properties were achieved at the expense of decreased ductility. Furthermore, there is very limited discussion across the literature on the effect of polymorphism toward performance of PVDF/MWCNT composites. All these issues will be discussed in the thesis.

Surface functionalization of CNTs has been reviewed in this chapter. There are basically two types of methods, physical and chemical functionalization, based on the connection with CNTs after the functionalization process. Both methods have their advantages. The physical method can well reserve the physical properties of CNTs while the chemical approaches facilitate further surface modifications. In chapter 3, we report a facile method to surface chemically functionalizes CNTs that can be well controlled to avoid significant damage to the CNTs wall.

Materials with special surface properties, such as superhydrophobic/superoleophilic and underwater superoleophobic membranes, can be used for oil/water separation. Besides, porous 3D materials can also separate oil/water mixtures by two consecutive steps, selective absorption and mechanical compression. Aerogel is one kind of highly porous material. Combining the hydrophobic feature of PVDF owing to its chemical structure, PVDF aerogel is promising to be used for both separation and absorption applications. The superhydrophobic/superoleophilic PVDF aerogel are fabricated and investigated in the thesis.

References

1. J. P. Lu, *J. Phys. Chem. Solids* 1997, **58**, 1649-1652.
2. M.-F. Yu, B. S. Files, S. Arepalli and R. S. Ruoff, *Phys Rev Lett*, 2000, **84**, 5552-5555.
3. M.-F. Yu, O. Lourie, M. J. Dyer, K. Moloni, T. F. Kelly and R. S. Ruoff, *Science* (80-), 2000, **287**, 637-640.
4. C. WD, *Materials science and engineering, an introduction*, New York: Wiley, 2003.
5. A. Kelly and W. R. Tyson, *J Mech Phys Solids*, 1965, **13**, 329-350.
6. M. A. H.L.Cox, F.R.Ae.S., A.M.I.Mech.E., *Br. J. Appl. Phys.* , 1952, **3**, 72-79.
7. G. P. Carman and K. L. Reifsnider, *Compos Sci Technol*, 1992, **43**, 137-146.
8. J. Gao, M. E. Itkis, A. Yu, E. Bekyarova, B. Zhao and R. C. Haddon, *J Am Chem Soc*, 2005, **127**, 3847-3854.
9. O. Meincke, D. Kaempfer, H. Weickmann, C. Friedrich, M. Vathauer and H. Warth, *Polymer (Guildf)*, 2004, **45**, 739-748.
10. T. Liu, I. Y. Phang, L. Shen, S. Y. Chow and W.-D. Zhang*, *Macromolecules*, 2004, **37**, 7214-7222.
11. M. Manchado, L. Valentini, J. Biagiotti and J. Kenny, *Carbon N Y*, 2005, **43**, 1499-1505.
12. J. Sandler, S. Pegel, M. Cadek, F. Gojny, M. Van Es, J. Lohmar, W. Blau, K. Schulte, A. Windle and M. Shaffer, *Polymer (Guildf)*, 2004, **45**, 2001-2015.
13. A. A. Mamedov, N. A. Kotov, M. Prato, D. M. Guldi, J. P. Wicksted and A. Hirsch, *Nat Mater*, 2002, **1**, 190-194.
14. R. Blake, J. N. Coleman, M. T. Byrne, J. E. McCarthy, T. S. Perova, W. J. Blau, A. Fonseca, J. B. Nagy and Y. K. Gun'ko, *J Mater Chem*, 2006, **16**, 4206-4213.
15. Y. Zou, Y. Feng, L. Wang and X. Liu, *Carbon N Y*, 2004, **42**, 271-277.
16. B. X. Yang, K. P. Pramoda, G. Q. Xu and S. H. Goh, *Adv Funct Mater*, 2007, **17**, 2062-2069.
17. K. H. Kim and W. H. Jo, *Compos Sci Technol*, 2008, **68**, 2120-2124.
18. K. H. Kim and W. H. Jo, *Carbon N Y*, 2009, **47**, 1126-1134.

19. L. Liu, A. H. Barber, S. Nuriel and H. D. Wagner, *Adv Funct Mater*, 2005, **15**, 975-980.
20. H. Hou, J. J. Ge, J. Zeng, Q. Li, D. H. Reneker, A. Greiner and S. Z. Cheng, *Chem. Mater.*, 2005, **17**, 967-973.
21. M. Xu, T. Zhang, B. Gu, J. Wu and Q. Chen, *Macromolecules*, 2006, **39**, 3540-3545.
22. A. Mandal and A. K. Nandi, *J Mater Chem*, 2011, **21**, 15752-15763.
23. W. Huang, K. Edenzon, L. Fernandez, S. Razmpour, J. Woodburn and P. Cebe, *J Appl Polym Sci*, 2010, **115**, 3238-3248.
24. X.-G. Tang, M. Hou, J. Zou, R. Truss, M. Yang and Z. Zhu, *Compos Sci Technol*, 2012, **72**, 263-268.
25. C.-M. Chang and Y.-L. Liu, *Carbon N Y*, 2010, **48**, 1289-1297.
26. K. H. Kim and W. H. Jo, *Composites Science and Technology*, 2008, **68**, 2120-2124.
27. L. Jin, C. Bower and O. Zhou, *Appl Phys Lett*, 1998, **73**, 1197-1199.
28. M. S. Shaffer and A. H. Windle, *Adv. Mater.*, 1999, **11**, 937-941.
29. D. Qian, E. C. Dickey, R. Andrews and T. Rantell, *Appl Phys Lett*, 2000, **76**, 2868-2870.
30. C. Velasco-Santos, A. Martinez-Hernandez, F. Fisher, R. Ruoff and V. Castano, *J Phys D Appl Phys*, 2003, **36**, 1423.
31. S. Ruan, P. Gao, X. Yang and T. Yu, *Polymer (Guildf)*, 2003, **44**, 5643-5654.
32. O. Probst, E. M. Moore, D. E. Resasco and B. P. Grady, *Polymer (Guildf)*, 2004, **45**, 4437-4443.
33. P. Watts and W. Hsu, *Nanotechnology*, 2003, **14**.
34. J. N. Coleman, M. Cadek, R. Blake, V. Nicolosi, K. P. Ryan, C. Belton, A. Fonseca, J. B. Nagy, Y. K. Gun'ko and W. J. Blau, *Adv Funct Mater*, 2004, **14**, 791-798.
35. M. Cadek, J. Coleman, K. Ryan, V. Nicolosi, G. Bister, A. Fonseca, J. Nagy, K. Szostak, F. Beguin and W. Blau, *Nano Lett*, 2004, **4**, 353-356.
36. O. Breuer and U. Sundararaj, *Polym. Compos.*, 2004, **25**, 630-645.
37. P. Pötschke, A. R. Bhattacharyya, A. Janke and H. Goering, *Compos. Interfaces* 2003, **10**, 389-404.
38. Z. Jin, K. Pramoda, G. Xu and S. H. Goh, *Chem Phys Lett*, 2001, **337**, 43-47.
39. W. De Zhang, L. Shen, I. Y. Phang and T. Liu, *Macromolecules*, 2004, **37**, 256-259.

40. R. E. Gorga and R. E. Cohen, *J. Polym. Sci., Part B: Polym. Phys.* , 2004, **42**, 2690-2702.
41. W. Tang, M. H. Santare and S. G. Advani, *Carbon N Y*, 2003, **41**, 2779-2785.
42. E. T. Thostenson and T.-W. Chou, *J Phys D Appl Phys*, 2002, **35**, L77.
43. C. A. Cooper, D. Ravich, D. Lips, J. Mayer and H. D. Wagner, *Compos Sci Technol*, 2002, **62**, 1105-1112.
44. C. Velasco-Santos, A. L. Martínez-Hernández, F. T. Fisher, R. Ruoff and V. M. Castaño, *Chem. Mater.* , 2003, **15**, 4470-4475.
45. J. Cheng, B. Zhao, S. Zheng, J. Yang, D. Zhang and M. Cao, *Applied Physics A*, 2015, **119**, 379-386.
46. L. Qu, L. M. Veca, Y. Lin, A. Kitaygorodskiy, B. Chen, A. M. McCall, J. W. Connell and Y.-P. Sun, *Macromolecules*, 2005, **38**, 10328-10331.
47. K. Balasubramanian and M. Burghard, *Small*, 2005, **1**, 180-192.
48. A. Hirsch and O. Vostrowsky, in *Functional molecular nanostructures*, Springer, 2005, pp. 193-237.
49. D. Tasis, N. Tagmatarchis, A. Bianco and M. Prato, *Chem Rev*, 2006, **106**, 1105-1136.
50. W. Gomulya, G. D. Costanzo, E. J. F. de Carvalho, S. Z. Bisri, V. Derenskiy, M. Fritsch, N. Fröhlich, S. Allard, P. Gordiichuk and A. Herrmann, *Advanced Materials*, 2013, **25**, 2948-2956.
51. K. Akazaki, F. Toshimitsu, H. Ozawa, T. Fujigaya and N. Nakashima, *Journal of the American Chemical Society*, 2012, **134**, 12700-12707.
52. P.-C. Ma, N. A. Siddiqui, G. Marom and J.-K. Kim, *Composites Part A: Applied Science and Manufacturing*, 2010, **41**, 1345-1367.
53. L. Vaisman, G. Marom and H. D. Wagner, *Adv Funct Mater*, 2006, **16**, 357-363.
54. Y. Geng, M. Y. Liu, J. Li, X. M. Shi and J. K. Kim, *Composites Part A: Applied Science and Manufacturing*, 2008, **39**, 1876-1883.
55. M. Islam, E. Rojas, D. Bergey, A. Johnson and A. Yodh, *Nano Lett*, 2003, **3**, 269-273.
56. E. A. Whitsitt and A. R. Barron, *Nano Lett*, 2003, **3**, 775-778.
57. T. H. Kim, C. Doe, S. R. Kline and S. M. Choi, *Adv. Mater.* , 2007, **19**, 929-933.

58. V. Georgakilas, D. Gournis, V. Tzitzios, L. Pasquato, D. M. Guldi and M. Prato, *Journal of Materials Chemistry*, 2007, **17**, 2679-2694.
59. H.-C. Wu, X. Chang, L. Liu, F. Zhao and Y. Zhao, *J Mater Chem*, 2010, **20**, 1036-1052.
60. M. Sano, A. Kamino, J. Okamura and S. Shinkai, *Science (80-)*, 2001, **293**, 1299-1301.
61. Y.-R. Shin, I.-Y. Jeon and J.-B. Baek, *Carbon N Y*, 2012, **50**, 1465-1476.
62. J. Ming, Y. Wu, Y. Yu and F. Zhao, *Chem. Commun.* , 2011, **47**, 5223-5225.
63. M. S. Strano, C. A. Dyke, M. L. Usrey, P. W. Barone, M. J. Allen, H. Shan, C. Kittrell, R. H. Hauge, J. M. Tour and R. E. Smalley, *Science (80-)*, 2003, **301**, 1519-1522.
64. C. A. Dyke and J. M. Tour, *Nano Lett*, 2003, **3**, 1215-1218.
65. H. Peng, P. Reverdy, V. N. Khabashesku and J. L. Margrave, *Chem. Commun.* , 2003, 362-363.
66. P. Umek, J. W. Seo, K. Hernadi, A. Mrzel, P. Pechy, D. D. Mihailovic and L. Forró, *Chem. Mater.* , 2003, **15**, 4751-4755.
67. Y. Ying, R. K. Saini, F. Liang, A. K. Sadana and W. Billups, *Org Lett*, 2003, **5**, 1471-1473.
68. B. Ni and S. B. Sinnott, *Phys. Rev. B*, 2000, **61**, R16343.
69. H. Peng, L. B. Alemany, J. L. Margrave and V. N. Khabashesku, *J Am Chem Soc*, 2003, **125**, 15174-15182.
70. T. Nakamura, M. Ishihara, T. Ohana, A. Tanaka and Y. Koga, *Diam Relat Mater*, 2004, **13**, 1971-1974.
71. T. Nakajima, S. Kasamatsu and Y. Matsuo, *Eur. J. Solid State Inorg. Chem.* , 1996, **33**, 831-840.
72. A. Hamwi, H. Alvergnat, S. Bonnamy and F. Beguin, *Carbon N Y*, 1997, **35**, 723-728.
73. E. Mickelson, C. Huffman, A. Rinzler, R. Smalley, R. Hauge and J. Margrave, *Chem Phys Lett*, 1998, **296**, 188-194.
74. H. Touhara and F. Okino, *Carbon N Y*, 2000, **38**, 241-267.

75. V. N. Khabashesku, W. E. Billups and J. L. Margrave, *Acc Chem Res*, 2002, **35**, 1087-1095.
76. M. Holzinger, O. Vostrowsky, A. Hirsch, F. Hennrich, M. Kappes, R. Weiss and F. Jellen, *Angew. Chem. Int. Ed.* , 2001, **40**, 4002-4005.
77. M. Holzinger, J. Abraham, P. Whelan, R. Graupner, L. Ley, F. Hennrich, M. Kappes and A. Hirsch, *J Am Chem Soc*, 2003, **125**, 8566-8580.
78. M. Holzinger, J. Steinmetz, D. Samaille, M. Glerup, M. Paillet, P. Bernier, L. Ley and R. Graupner, *Carbon N Y*, 2004, **42**, 941-947.
79. N. Tagmatarchis, V. Georgakilas, M. Prato and H. Shinohara, *Chem. Commun.* , 2002, **0**, 2010-2011.
80. T. S. Balaban, M. C. Balaban, S. Malik, F. Hennrich, R. Fischer, H. Rösner and M. M. Kappes, *Adv. Mater.* , 2006, **18**, 2763-2767.
81. E. V. Basiuk, M. Monroy-Peláez, I. Puente-Lee and V. A. Basiuk, *Nano Lett*, 2004, **4**, 863-866.
82. S. Banerjee and S. S. Wong, *The journal of physical chemistry B*, 2002, **106**, 12144-12151.
83. J. L. Delgado, P. de la Cruz, F. Langa, A. Urbina, J. Casado and J. T. L. Navarrete, *Chem. Commun.* , 2004, 1734-1735.
84. Z. Chu, Y. Feng and S. Seeger, *Angew. Chem. Int. Ed.* , 2015, **54**, 2328-2338.
85. W. Zhang, Z. Shi, F. Zhang, X. Liu, J. Jin and L. Jiang, *Adv. Mater.* , 2013, **25**, 2071-2076.
86. C.-F. Wang, F.-S. Tzeng, H.-G. Chen and C.-J. Chang, *Langmuir*, 2012, **28**, 10015-10019.
87. R. N. Wenzel, *Industrial & Engineering Chemistry*, 1936, **28**, 988-994.
88. A. Cassie and S. Baxter, *Transactions of the Faraday Society*, 1944, **40**, 546-551.
89. L. Wang, S. Yang, J. Wang, C. Wang and L. Chen, *Mater Lett*, 2011, **65**, 869-872.
90. L. Feng, Z. Zhang, Z. Mai, Y. Ma, B. Liu, L. Jiang and D. Zhu, *Angew. Chem. Int. Ed.* , 2004, **43**, 2012-2014.
91. C. R. Crick, J. A. Gibbins and I. P. Parkin, *Journal of Materials Chemistry A*, 2013, **1**, 5943-5948.
92. J. Zhang and S. Seeger, *Adv Funct Mater*, 2011, **21**, 4699-4704.

93. L. Wu, J. Zhang, B. Li and A. Wang, *J Colloid Interface Sci*, 2014, **413**, 112-117.
94. X. Zhou, Z. Zhang, X. Xu, F. Guo, X. Zhu, X. Men and B. Ge, *ACS Appl Mater Interfaces*, 2013, **5**, 7208-7214.
95. W. Liang and Z. Guo, *RSC Adv*, 2013, **3**, 16469-16474.
96. B. Wang, J. Li, G. Wang, W. Liang, Y. Zhang, L. Shi, Z. Guo and W. Liu, *ACS Appl Mater Interfaces*, 2013, **5**, 1827-1839.
97. L. Wu, J. Zhang, B. Li and A. Wang, *Journal of Materials Chemistry B*, 2013, **1**, 4756-4763.
98. Q. Zhu, Y. Chu, Z. Wang, N. Chen, L. Lin, F. Liu and Q. Pan, *Journal of Materials Chemistry A*, 2013, **1**, 5386-5393.
99. X. Zhang, Z. Li, K. Liu and L. Jiang, *Adv Funct Mater*, 2013, **23**, 2881-2886.
100. P. Calcagnile, D. Fragouli, I. S. Bayer, G. C. Anyfantis, L. Martiradonna, P. D. Cozzoli, R. Cingolani and A. Athanassiou, *ACS Nano*, 2012, **6**, 5413-5419.
101. J. Li, L. Shi, Y. Chen, Y. Zhang, Z. Guo, B.-l. Su and W. Liu, *J Mater Chem*, 2012, **22**, 9774-9781.
102. C.-F. Wang and S.-J. Lin, *ACS Appl Mater Interfaces*, 2013, **5**, 8861-8864.
103. W. Zhang, Y. Zhu, X. Liu, D. Wang, J. Li, L. Jiang and J. Jin, *Angew. Chem. Int. Ed.*, 2014, **53**, 856-860.
104. Z. Xue, S. Wang, L. Lin, L. Chen, M. Liu, L. Feng and L. Jiang, *Adv. Mater.*, 2011, **23**, 4270-4273.
105. L. Zhang, Y. Zhong, D. Cha and P. Wang, *Sci Rep*, 2013, **3**.
106. A. K. Kota, G. Kwon, W. Choi, J. M. Mabry and A. Tuteja, *Nat Commun*, 2012, **3**, 1025.
107. F. Zhang, W. B. Zhang, Z. Shi, D. Wang, J. Jin and L. Jiang, *Adv. Mater.*, 2013, **25**, 4192-4198.
108. P. Wagh, R. Begag, G. Pajonk, A. V. Rao and D. Haranath, *Mater Chem Phys*, 1999, **57**, 214-218.
109. S. S. Kistler, *Nature*, 1931, **127**, 741.
110. A. E. Aliev, J. Oh, M. E. Kozlov, A. A. Kuznetsov, S. Fang, A. F. Fonseca, R. Ovalle, M. D. Lima, M. H. Haque and Y. N. Gartstein, *Science (80-)*, 2009, **323**, 1575-1578.

111. N. Hüsing and U. Schubert, *Angew. Chem. Int. Ed.* , 1998, **37**, 22-45.
112. X. Wang, L. Liu, X. Wang, L. Bai, H. Wu, X. Zhang, L. Yi and Q. Chen, *J. Solid State Electrochem.* , 2011, **15**, 643-648.
113. E. Cuce, P. M. Cuce, C. J. Wood and S. B. Riffat, *Renewable Sustainable Energy Rev.* , 2014, **34**, 273-299.
114. R. Baetens, B. P. Jelle and A. Gustavsen, *Energy and Buildings*, 2011, **43**, 761-769.
115. Z. Ulker and C. Erkey, *J. Controlled Release* 2014, **177**, 51-63.
116. J. Biener, M. Stadermann, M. Suss, M. A. Worsley, M. M. Biener, K. A. Rose and T. F. Baumann, *Energy Environ. Sci.* , 2011, **4**, 656-667.
117. B. Menaa, F. Menaa, C. Aiolfi-Guimaraes and O. Sharts, *Int. J. Nanotechnol.* , 2009, **7**, 1-45.
118. H. Schäfer, B. Milow and L. Ratke, *RSC Adv*, 2013, **3**, 15263-15272.
119. Y. Qian, I. M. Ismail and A. Stein, *Carbon N Y*, 2014, **68**, 221-231.
120. H. Sai, L. Xing, J. Xiang, L. Cui, J. Jiao, C. Zhao, Z. Li and F. Li, *Journal of Materials Chemistry A*, 2013, **1**, 7963-7970.
121. A. S. Dorcheh and M. Abbasi, *J. Mater. Process. Technol.* , 2008, **199**, 10-26.
122. S. H. Kim, M. A. Worsley, C. A. Valdez, S. J. Shin, C. Dawedeit, T. Braun, T. F. Baumann, S. A. Letts, S. O. Kucheyev and K. J. J. Wu, *RSC Adv*, 2012, **2**, 8672-8680.
123. M. A. B. Meador, E. J. Malow, R. Silva, S. Wright, D. Quade, S. L. Vivod, H. Guo, J. Guo and M. Cakmak, *ACS Appl Mater Interfaces*, 2012, **4**, 536-544.
124. R. Li, C. Chen, J. Li, L. Xu, G. Xiao and D. Yan, *Journal of Materials Chemistry A*, 2014, **2**, 3057-3064.
125. S. Víctor-Román, C. Simón-Herrero, A. Romero, I. Gracia, J. L. Valverde and L. Sánchez-Silva, *Chem. Eng. J.* , 2015, **262**, 691-701.
126. J. Zhang, Y. Cao, J. Feng and P. Wu, *The Journal of Physical Chemistry C*, 2012, **116**, 8063-8068.
127. H. Qi, E. Mäder and J. Liu, *Journal of Materials Chemistry A*, 2013, **1**, 9714-9720.
128. M. Wang, I. V. Anoshkin, A. G. Nasibulin, J. T. Korhonen, J. Seitsonen, J. Pere, E. I. Kauppinen, R. H. Ras and O. Ikkala, *Adv. Mater.* , 2013, **25**, 2428-2432.

129. X. Gong, J. Liu, S. Baskaran, R. D. Voise and J. S. Young, *Chem. Mater.*, 2000, **12**, 1049-1052.
130. B. S. Ince-Gunduz, R. Alpern, D. Amare, J. Crawford, B. Dolan, S. Jones, R. Kobylarz, M. Reveley and P. Cebe, *Polymer (Guildf)*, 2010, **51**, 1485-1493.
131. W. M. Prest and D. J. Luca, *J Appl Phys*, 1975, **46**, 4136-4143.
132. R. Gregorio, *J Appl Polym Sci*, 2006, **100**, 3272-3279.
133. Y. Bormashenko, R. Pogreb, O. Stanevsky and E. Bormashenko, *Polym Test*, 2004, **23**, 791-796.
134. S. Lanceros-Mendez, J. Mano, A. Costa and V. Schmidt, *Journal of Macromolecular Science, Part B*, 2001, **40**, 517-527.
135. J. Yang, J. Wang, Q. Zhang, F. Chen, H. Deng, K. Wang and Q. Fu, *Polymer (Guildf)*, 2011, **52**, 4970-4978.
136. Y.-C. Chiang, W.-H. Lin and Y.-C. Chang, *Appl Surf Sci*, 2011, **257**, 2401-2410.
137. Y. Li, W. Zhou, H. Wang, L. Xie, Y. Liang, F. Wei, J.-C. Idrobo, S. J. Pennycook and H. Dai, *Nat Nanotechnol*, 2012, **7**, 394-400.
138. D. Yang, A. Velamakanni, G. Bozoklu, S. Park, M. Stoller, R. D. Piner, S. Stankovich, I. Jung, D. A. Field and C. A. Ventrice, *Carbon N Y*, 2009, **47**, 145-152.
139. S. Yang, L. Zhi, K. Tang, X. Feng, J. Maier and K. Müllen, *Adv Funct Mater*, 2012, **22**, 3634-3640.
140. S. Kim, S. Zhou, Y. Hu, M. Acik, Y. J. Chabal, C. Berger, W. de Heer, A. Bongiorno and E. Riedo, *Nat Mater*, 2012, **11**, 544-549.
141. S. Park, J. An, J. R. Potts, A. Velamakanni, S. Murali and R. S. Ruoff, *Carbon N Y*, 2011, **49**, 3019-3023.
142. S. Kundu, Y. Wang, W. Xia and M. Muhler, *The Journal of Physical Chemistry C*, 2008, **112**, 16869-16878.
143. W. Xia, Y. Wang, R. Bergsträßer, S. Kundu and M. Muhler, *Appl Surf Sci*, 2007, **254**, 247-250.
144. R. Larciprete, S. Gardonio, L. Petaccia and S. Lizzit, *Carbon N Y*, 2009, **47**, 2579-2589.
145. V. Datsyuk, M. Kalyva, K. Papagelis, J. Parthenios, D. Tasis, A. Siokou, I. Kallitsis and C. Galiotis, *Carbon N Y*, 2008, **46**, 833-840.

146. H. Lee, Y. N. Choi, S. B. Choi, J. H. Seo, J. Kim, I. H. Cho, S. Gang and C. H. Jeon, *The Journal of Physical Chemistry C*, 2014, **118**, 5691-5699.
147. M. E. Itkis, D. E. Perea, R. Jung, S. Niyogi and R. C. Haddon, *J Am Chem Soc*, 2005, **127**, 3439-3448.
148. G. Mercier, J. r. m. Gleize, J. Ghanbaja, J.-F. o. Marêché and B. Vigolo, *The Journal of Physical Chemistry C*, 2013, **117**, 8522-8529.

Chapter 3 Surface Functionalization of Carbon Nanotubes

Despite extensive study on carbon nanotube (CNT), the proliferation of its real applications has been hindered by its dispersibility in various organic or inorganic media. Very often complex surface functionalization processes are required to endow CNTs with enhanced dispersibility. Hence, facile, high-yield, and scalable functionalization methods for CNT for better dispersion are highly desirable. Thermal annealing is sometimes adopted for purification of CNT, however limited discussion has been devoted to its functionalization effect and surface chemistry, which directly determine CNT dispersibility. In this work, via controlled mild thermal annealing, enhanced dispersion of functionalized CNTs was achieved in different organic solvents, including ethanol, dimethyl formamide, chloroform and acetone. Such enhancement had been studied through qualitative (dispersion and sedimentation, TEM) and quantitative analyses (XPS, Raman) of morphological structures and chemical states of thermally functionalized CNTs. The analyses reveal that under mild thermal annealing conditions, the surface oxidative reactions of the CNT can be well controlled, with minimal damage to the graphitic structure of the CNT. A plausible functionalization mechanism involving ether and quinone functional groups is proposed. The advantages of thermal annealing toward enhanced dispersion are further demonstrated by employing the functionalized CNT in poly (vinylidene fluoride) (PVDF) composite and drop-cast conductive CNT pattern.

3.1 Introduction

In the past two decades, carbon nanotubes (CNTs) as a quasi-1D material have been extensively investigated because of their unique and outstanding mechanical, chemical, electrical, electronic, and thermal properties. Their applications include, but not limited to, composite materials, sensors, photovoltaic devices, actuators, transistors and energy storage devices¹⁻³. However, due to the typical high aspect ratio (>100) and existing Van der Waals forces between CNTs, they usually form highly entangled bundles⁴. Such entanglement of CNTs causes poor dispersion in any solvent and seriously hinders their potential applications. Multiple strategies have been explored to disperse CNTs in various solvents via covalent and non-covalent modifications. Oxidation by strong acids is often a common and effective chemical modification, which introduces polar surface functional groups, e.g., carboxylic, hydroxyl, and ketone groups, to render good dispersion in mainly aqueous medium^{5, 6}. Despite the effectiveness of acid/chemical oxidation, the drawbacks of this approach are obvious. It requires usage of large quantity of strong acids, which limits industrial scale production and causes pollution. Another method is non-covalent physical wrapping of polymers on the surface of CNTs, which can also improve CNT dispersion^{7, 8}. Unlike oxidation, physical wrapping does not directly introduce new functional groups on CNTs. The polymer chains usually interact physically with CNTs to form a supramolecular structure. However, these physically wrapping polymers have to be specially designed and involves tedious synthesis steps, again limiting its practicality. Thermal annealing is widely adopted to process carbon materials, contributed by its simplicity, scalability and environmental friendliness^{9, 10}. It is known that annealing at high temperature in inert atmosphere generates more graphitic CNTs by removing dangling bonds and functional groups; while annealing at low temperature in oxidative gas (e.g., air or ozone) could have multiple effects on CNTs structures^{11, 12}. Yang et al. functionalized MWCNTs in air at 500 °C and demonstrated enhanced catalytic performance for wet air oxidation of phenol contributed by introduced oxygen containing functional groups¹³. Li et al.¹⁴ and Seo et al.¹⁵ reported improved electric double layer capacitance of MWCNTs thermally annealed in air, contributed by the increased surface area. Kung et al.¹⁶ and Zeng et al.¹⁷ studied the effects of heat treatment in air toward

field emission of MWCNTs. They found lower onset emission voltage and enhanced emission current with thermal annealing, which were claimed to be the results of selectively opened CNTs tips and increased surface area. We would like to highlight that most of the previous works on thermal annealing of CNTs focused on CNT based device performance, paying little attention to fundamental relationship between surface chemistry during thermal functionalization, as well as the dispersion behaviour in organic solvents. In this work, by controlling the thermal annealing conditions, we studied the effects of relatively mild annealing in oxidative atmosphere toward MWCNTs dispersion. Under the controlled conditions, the structural integrity of the CNT was maintained during our mild thermal annealing, at the same time promising high functionalized CNT yield. We propose a new mechanism that involves the formation of oxygen-containing surface ether C-O-C and quinone C=O functional groups, which directly helps to enhance the CNT dispersion.

3.2 Experiments

3.2.1 Air Annealing

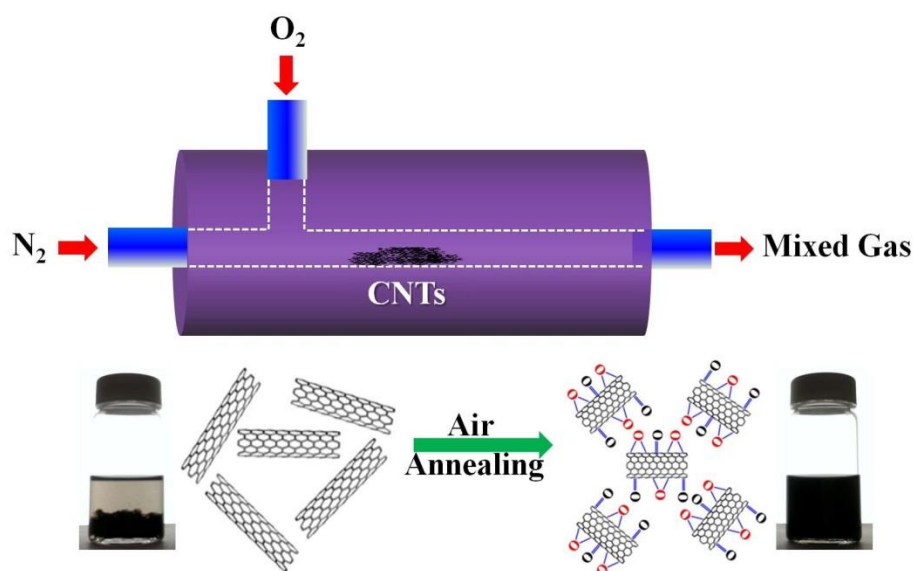


Figure 3.1 Schematic illustration of air annealing process of CNTs and their dispersion states in organic solvent before and after treatment.

Annealing process was performed in a Thermal Gravimetric Analyser (Q 500, TA Instruments). Raw CNTs without any pre-treatment were placed in a platinum boat and were heated to the pre-set temperature between 450 and 550 °C at 5 °C/min with an air flow rate of 5 ml/min. A simultaneous flow of N₂ at 50 ml/min was used. A schematic illustration of the process is given in Figure 3.1.

3.2.2 Dispersion of Air-Annealed CNTs in PVDF

Calculated amount of CNTs was processed with high power sonication (ultrasonic processor VCX 130, SONICS) for 5 mins in DMF. After that, dissolved PVDF in 50 ml DMF was mixed with CNTs solution by magnetic stirring for 1 hour and bath sonication for 1 hour. The uniform PVDF/CNTs/DMF solution was dried at 100 °C in hotplate and 120 °C in vacuum oven overnight.

3.2.4 Characterizations

The morphology of CNTs was studied using transmission electron microscope (TEM) (Carl Zeiss Libra 120 Plus). The fractural morphology of prepared composite samples was studied by field emission scanning electron microscope (FESEM) (JEOL JSM-7600F). SEM samples were prepared by firstly immersing the PVDF/CNT composites inside liquid nitrogen before fracturing them, and then the fractured surfaces were coated with platinum for 45s before SEM observation. Compositional analysis of CNTs was carried out using an X-ray photoelectron spectroscopy (XPS) equipped with an Axis Ultra spectrometer (Kratos Analytical). A monochromatic Al K α X-ray (1486.7 eV) operating at 15 kV was used as the source. Raman spectra were recorded by a Witec Alpha 300 SR spectrometer with an Argon ion laser (488 nm, 20mW) as the excitation source. For each sample, five Raman spectra were recorded at difference sample locations. To test the electrical resistivity of thermally annealed CNTs, 0.5 mg CNTs were dispersed in 10 ml ethanol and drop cast at 50 °C on glass with patterned ITO electrodes. The electrical measurement was done by Hewlett Packard 4140B pA

Meter/DC Voltage source. The I-V curves were measured over a range of 0.2 to -0.2 V, with a step of 0.01 V in normal ambient.

3.3 Results and Discussion

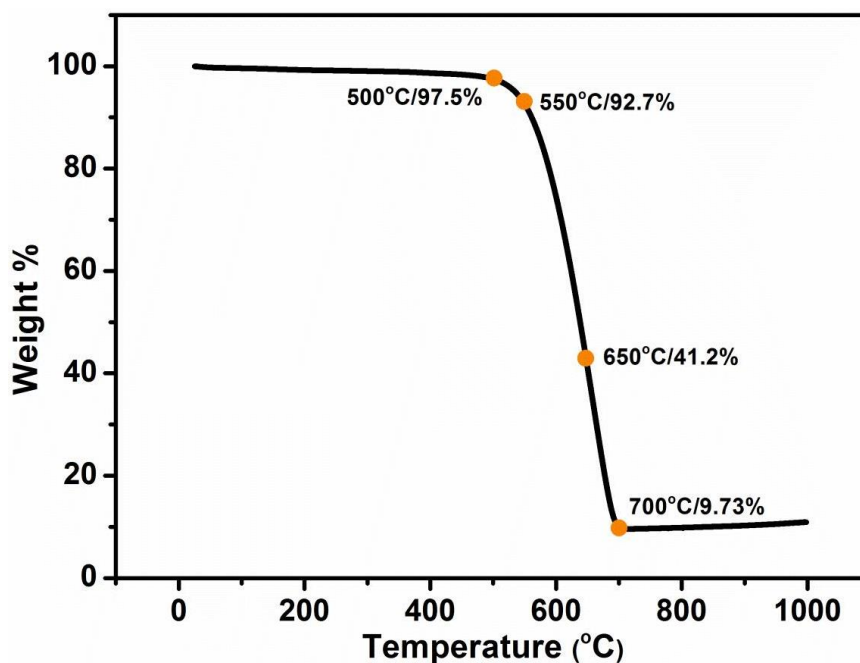


Figure 3.2 TGA curve of raw CNTs.

Figure 3.2 shows the TGA curve of CNTs in air and the decomposition of CNTs can be roughly divided into four steps. Before 500 °C, there is no obvious change for CNTs. The minor weight cut-off is due to the elimination of moisture and some other adsorbed materials. Slow oxidation might occur within this temperature range. Between 500 to 550 °C, weight decreases apparently but the decomposition rate is quite slow. High temperature before 550 °C is promising in functionalizing CNTs without serious decomposition. Between 550 and 700 °C, CNTs were quickly transformed into ash; beyond 700 °C there is only metal oxide left. In order to verify the hypothesis of air annealing, a trial sample of CNTs were treated at 650 °C. Due to the high decomposition rate, the temperature was increased to a set value and stopped without any isothermal annealing process.

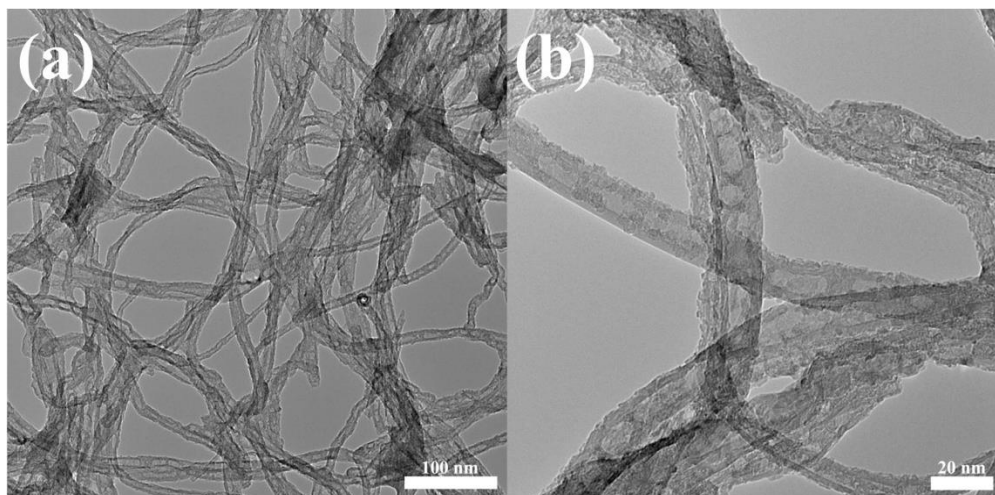


Figure 3.3 TEM images of a CNT sample air annealed at 650 °C with different magnifications.

Figure 3.3 (a) shows the TEM images of trial sample treated at temperature up to 650 °C. Compared with the rather clean surfaces of raw CNTs, the CNTs from trial sample appear to be attached to each other after high temperature treatment, although the truncation effect is not obvious. From the high magnification picture in Fig. 3.3 (b), the crystalline structure of CNT walls were seriously damaged and large amount of carbonaceous carbon was attached onto both the inner and outer surface of CNTs. This indicates the air is very aggressive to CNTs at this temperature. Dispersion test showed raw CNTs begins to sediment simultaneously after the sonication stops. In fact, the raw CNTs form flocculated structure and cannot be uniformly dispersed even with sonication. By contrast, the trial sample can be stable for months without obvious sedimentation.

Based on TGA analysis and preliminary study, a suitable temperature range was set between 350 and 550 °C for detailed study. In fact, it is not difficult to understand that oxidation can only occur above a critical temperature and accelerates as temperature increases. Furthermore, too high the temperature leads to excessive oxidation of CNTs in a short time and results in excessive weight loss and hence low yields. For example, CNTs treated at 650 °C led to 59% weight loss, i.e., low yield.

Figure 3.4 (a) shows the weight loss of various thermally treated samples. At 350 °C, the residue mass is almost constant from 30 to 120 mins of annealing durations, suggesting that CNTs are insensitive to oxidation at this temperature. Higher annealing temperature

expectedly leads to higher oxidation rate. For heating above 400 °C, the weight loss increases with longer annealing duration. When treated at 450 °C for 30 mins (A3), 96.4 wt. % CNTs were obtained. With prolonged annealing duration to 60 (B3), 90 (C3) and 120 mins (D3), the residue mass decreased to 95.8, 93.8 and 91.9%, respectively. At fixed 60 mins annealing duration, the residue mass for samples treated at 400, 450, 500 and 550 °C are 98.0, 95.8, 74.1 and 34.7 wt. %, respectively. The oxidation is greatly accelerated at 90 min@550 °C annealing and almost no carbon-based material remained, leaving behind only metal oxide based catalytic materials (C5 and D5).

With successful thermal functionalization, the introduced oxygen-containing groups on CNTs are able to form hydrogen bonding with polar solvents (e.g. ethanol), leading to enhanced dispersibility of CNTs. However, samples annealed at 350 °C with different durations (A1, B1, C1 and D1) were poorly dispersed (Figure 1b), indicating ineffective functionalization. Minimal weight loss and no clear improvement of dispersibility were observed for the samples annealed at 400 °C from 30 mins to 120 mins (A2, B2, C2 and D2). Samples annealed at 450 °C with shorter duration (A3: 30 min and B3: 60 mins) also could not be dispersed well in ethanol. Nevertheless, the fact that better dispersibility of CNTs followed by extended annealing duration (C3, 90 min and D3, 120 min) suggested that certain amount of oxygen-containing groups had formed on CNTs at 450 °C. All four samples annealed at 500 °C (A4, B4, C4 and D4) showed satisfactory dispersibility in ethanol. High enough annealed CNT yields were also achieved under this temperature, i.e. 85.0, 74.1, 67.6 and 62.7 wt. % respectively for annealing duration from 30 to 120 mins. The yield is much higher than that of similar previous work that employed air as to purify CNTs, which is believed to be contributed by much milder oxidation with minimal air flow rate in this study¹⁸. Higher annealing temperature at 550 °C is much more effective in oxidizing CNTs. Samples treated at this temperature with short duration of 30 or 60 mins (A5 and B5) showed very good dispersibility. However, the annealing yield is low, which were 42.0 and 34.7 wt. %. The structural integrity of CNTs annealed under these conditions had been compromised. Longer annealing durations (C5: 90 min and D5: 120 min) led to formation of metal oxide based residue, which is impossible to be dispersed in ethanol. Besides ethanol, representative organic

solvents with different polarity, i.e., acetone, chloroform and DMF were also found to be able to disperse well the thermally functionalized CNTs.

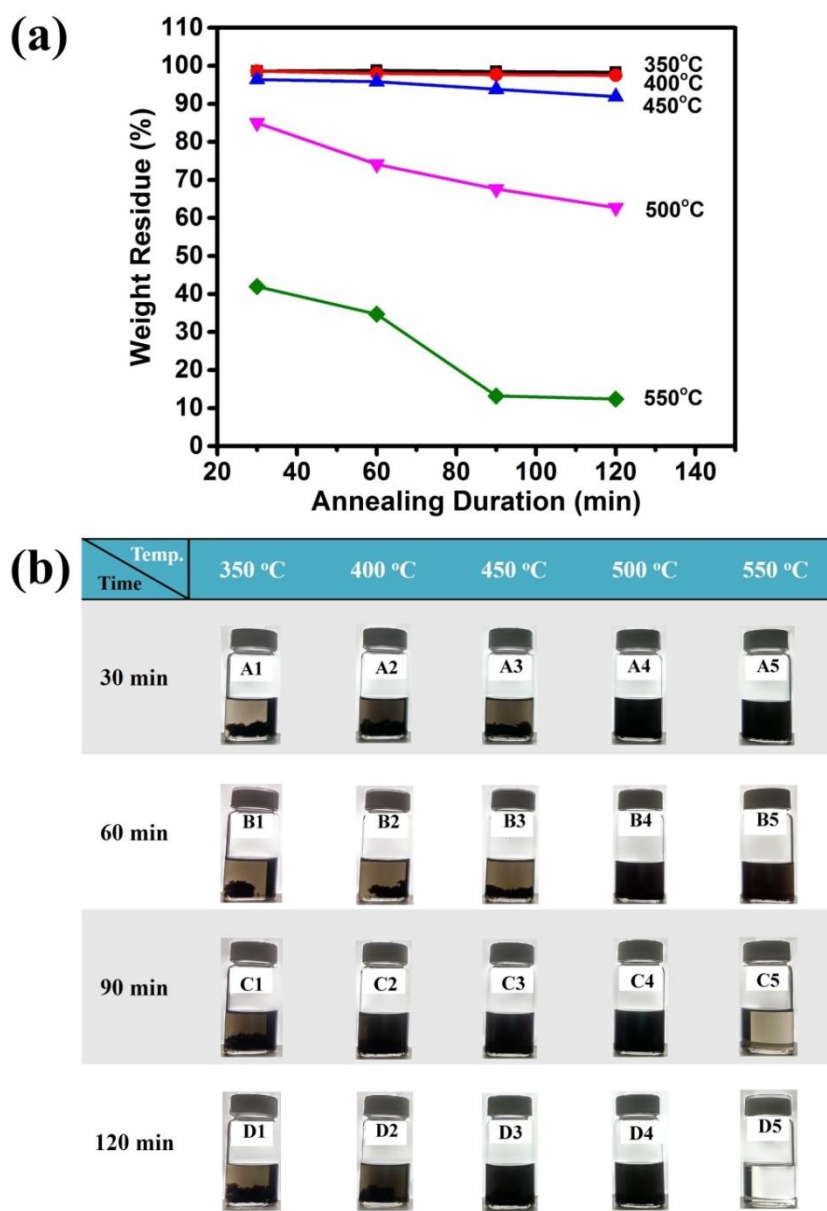


Figure 3.4 The residue masses at different annealing conditions (a) and digital photographs of 1-week CNTs dispersion samples, prepared by sonicating 0.5 mg CNTs in 10 ml ethanol for 60 mins (b). Labelled on glass vials are the sample codes corresponding to different thermal functionalization conditions.

From the dispersion test, annealed samples A4 (30min@500 °C) and D3 (120min@450 °C) showed that their conditions are optimal, contributed by the combined high yields and excellent dispersibility of CNTs. To examine their surface morphologies, TEM (shown in Figure 3.5) was employed. Comparing with that of raw CNTs, it can be seen that samples A4 and D3 have similar overall morphology with subtly rougher surfaces (Figure 3.5 b and 3.5 c inset images). The defects and particles generated on the CNTs surface evidenced the successful functionalization via thermal annealing. The weight losses for both samples are less than 15%, mainly attributed to the evaporation of moisture and elimination of amorphous carbon, while not including the oxidative gasification of carbon atoms. These results again demonstrate that controlled thermal annealing can facilely functionalize CNT at high yield and achieve excellent dispersion in organic solvents, without excessively damaging the integrity of the graphitic structure. Conventional CNT functionalization using boiling acids severely damages the graphitic structure of the CNTs, creating a relatively thick amorphous layer on outer surface of CNTs¹⁹. Such amorphous layer adversely affects the thermal stability and electrical properties. Obvious structural damage because of the rapid and excess oxidation at this temperature could be observed in sample B5 (Figure 3.5 d). It is well accepted that the CNT tips, as well as bends and kinks within the tubular structures, bear more strain and are more prone to be attacked upon oxidation. Thus, CNT surfaces are likely to be opened or cut at these positions, leading to shorter tubes with varied curvatures. No obvious CNTs fragmentation effect or curvature changes was observed from our TEM images, which is believed to be caused by the mild oxidative condition used in this work. Nevertheless, the CNT surface of sample B5 is thinner than that of raw CNTs, indicating that the outer layers of CNTs have been 'etched off' via oxidation.

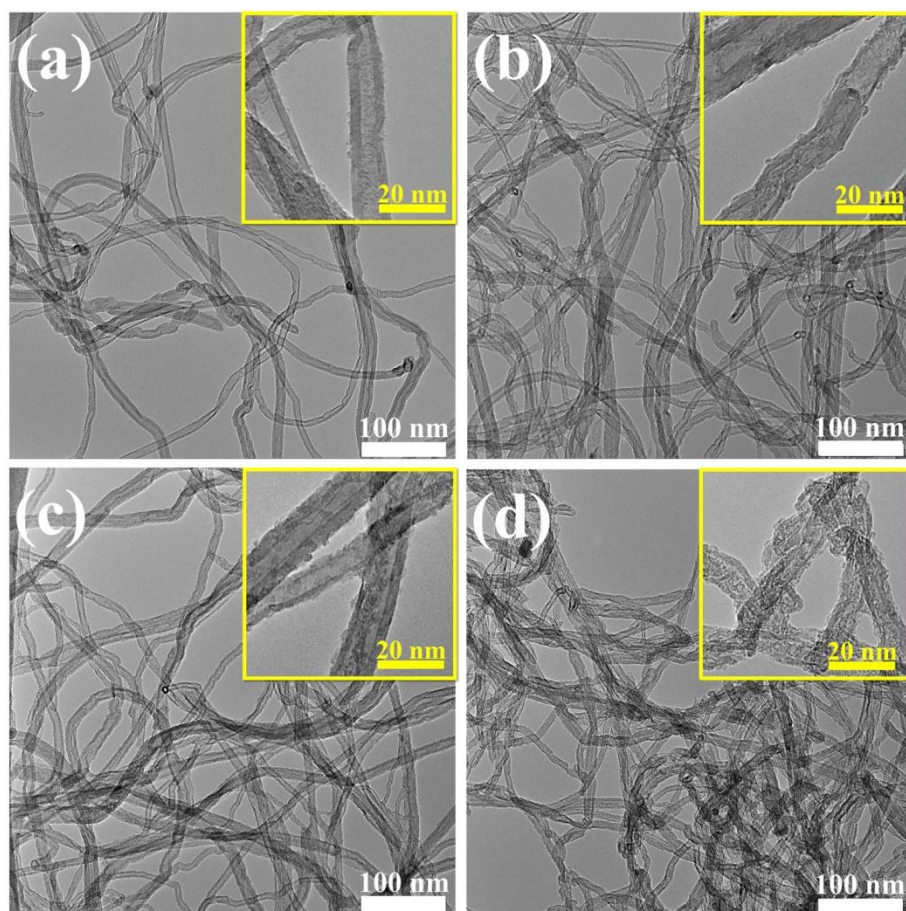


Figure 3.5 TEM images of (a) raw CNTs and annealed CNTs under different conditions: (b) A4, 30min@500 °C (c) D3, 120min@450 °C and (d) B5, 60min@550 °C. The insets are enlarged images showing structural changes after thermal functionalization; in which CNT surface of sample A4 and D3 are well preserved while that of B5 is clearly damaged.

The effect of thermal functionalization toward the surface chemistry of CNT was further investigated by Raman spectroscopy. It is well known that Raman effect is sensitive to any chemical modifications of CNT, such as any introduced defects and new functional groups^{14, 20, 21}. Raman spectra were collected from groups with fixed annealing duration (A1, A2, A3, A4 and A5) and temperature (A3, B3, C3 and D3), as shown in Figure 3.6. The peak called D band around 1350 cm^{-1} , representing sp^3 carbon atoms, is closely related to the integrity and intactness of the graphitic structure. The intensity of D band increases with the increase of defects sites, impurities, and the amount of amorphous carbon²². The peak at 1570 cm^{-1} is called G band, which comes from the conjugated

carbon atoms of sp^2 hybridization. The I_D/I_G intensity ratio is a frequently used indicator of defects on CNTs. When temperature increased from 350 to 450 °C, I_D/I_G values of A1, A2 and A3 also increased slightly, indicating very minor oxidation. It is known that thermal annealing has dual effects toward CNTs structure. On one hand, CNT can be oxidized and new defects sites formed, contributing to the D band. On the other hand, amorphous carbon on the CNT surface can be effectively eliminated, reducing the intensity of D band. It is believed that the amorphous carbon was largely reduced in A4 sample, which effects overwhelmed that of the newly formed defects, leading to an eventual suppressed I_D/I_G value. Similar phenomenon was also reported by other group¹⁸. The large increase of I_D/I_G value from A4 to A5 is caused by the extensive oxidation that created plenty of dangling oxygen-containing groups. Same trend was also observed when CNTs were annealed at fixed temperature and varied durations. Slight increase of I_D/I_G value was observed for A3 and B3 samples, as compared with that of raw CNTs. The I_D/I_G value declined firstly before increasing again, indicating simultaneous elimination of amorphous carbon and creation of new functional groups.

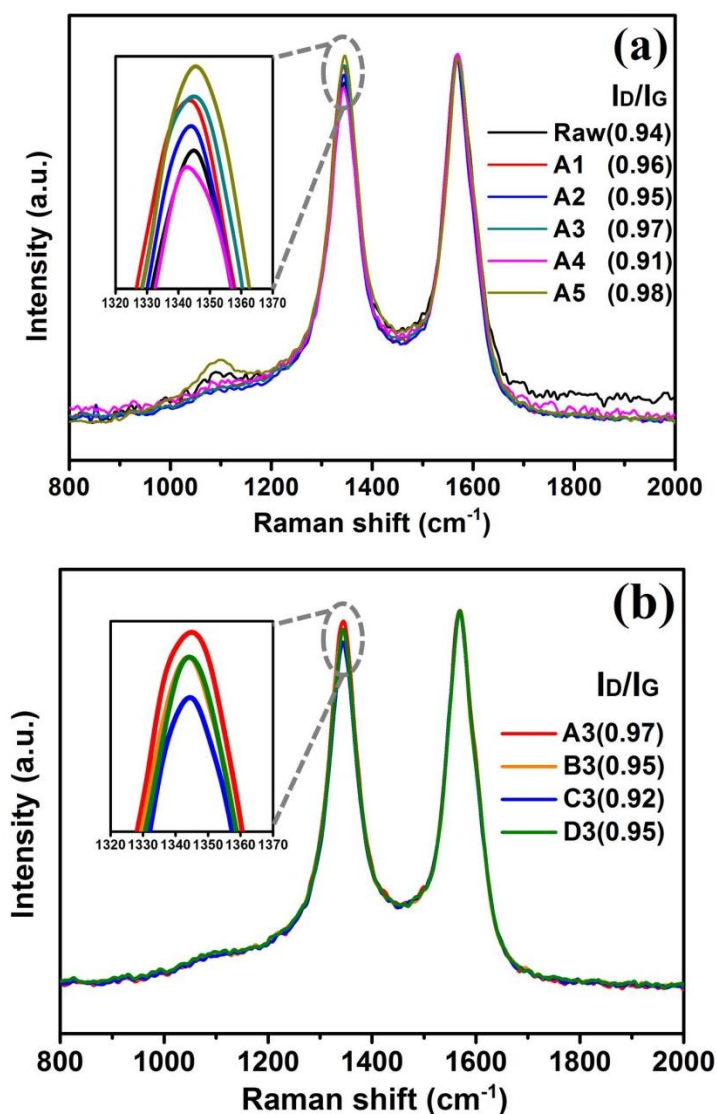


Figure 3.6 Raman spectra of raw CNTs and annealed samples. (a) CNTs are annealed for 30 mins at different temperatures, (b) CNTs are annealed at 450 °C for different durations. The curves are normalized with the G band as the reference, so the I_D/I_G values can be easily compared. The I_D/I_G values of each samples are included inside the right-hand-side brackets.

XPS is a useful tool to study the elemental compositions and functional groups on CNTs, either qualitatively or quantitatively²³⁻²⁶. Figure 3.7 (a) shows the C1s and O1s XPS spectra of raw CNTs and representative annealed samples. The oxygen content found in raw CNTs is believed to be due to impurities or catalyst residues. The oxygen content increases after thermal annealing; explaining the enhanced dispersibility of CNTs in organic solvents as more hydrogen bonding is formed. The total oxygen contents of a

series of selected samples are summarized in Table 3.1. The oxygen contents are 5.56, 7.37, 7.42 and 12.93% for samples A3, A4, D3 and A5, respectively; showing a gradual increasing trend at higher temperature/longer duration.

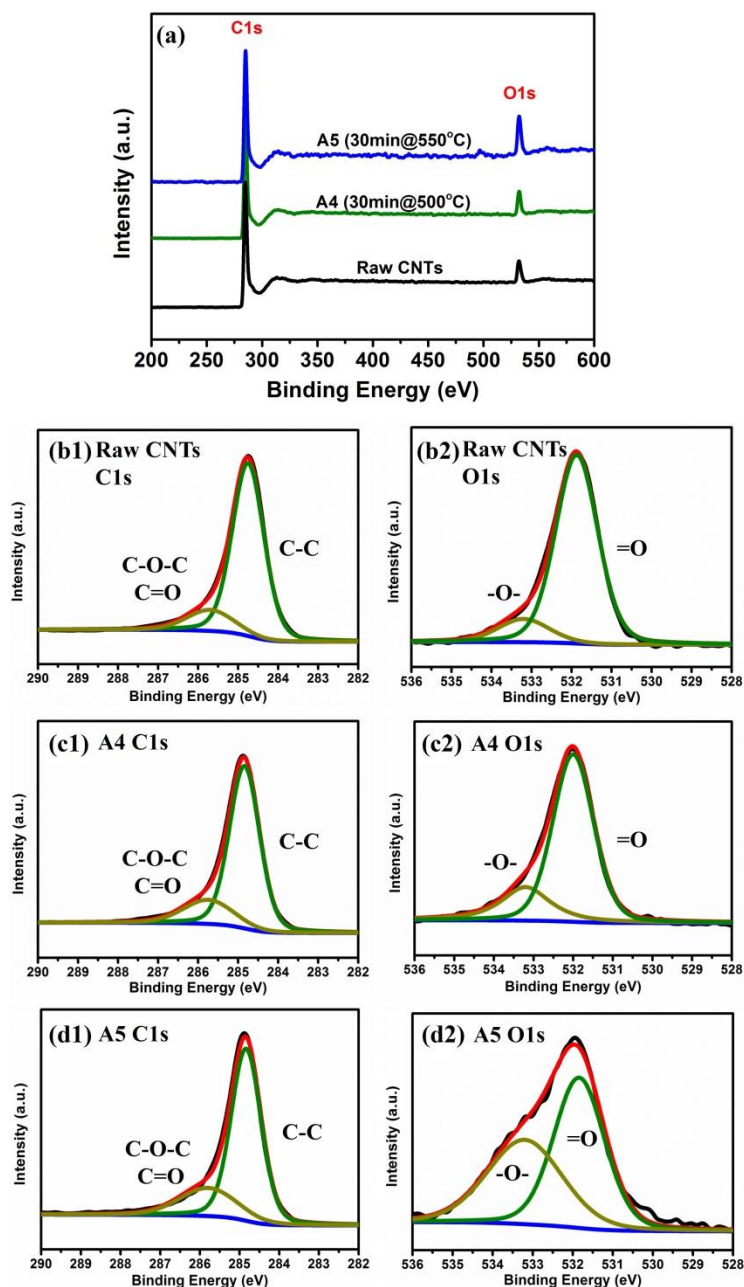


Figure 3.7 XPS spectra of raw CNTs, sample A4 (30mins@500°C) and A5 (30mins@550°C) (a) and deconvoluted high resolution XPS C1s spectra of raw CNTs (b1) A4 (c1) and A5 (d1); the corresponding O1s are given in (b2), (c2) and (d2), respectively. The oxygen contents for raw CNTs, A4 and A5 are calculated to be 5.53, 7.37 and 12.93 %, respectively.

Table 3.1 Percentages of different C and O oxidation states as determined from XPS spectra.

Sample	C 1s		O 1s		Total O wt. %
	284.8 eV (C-C)	285.8 eV (C-O-C, C=O)	531.9 eV (=O)	533.2 eV (-O-)	
Raw CNTs	84.71%	15.29%	84.71%	15.29%	5.53
A3(30min@450°C)	82.52%	17.48%	83.60%	16.40%	5.56
A4(30min@500°C)	80.25%	19.75%	76.87%	23.13%	7.37
A5(30min@550°C)	76.25%	23.75%	54.73%	45.27%	12.93
D3(120min@450°C)	81.41%	18.59%	81.37%	18.63%	7.42

The deconvoluted C1s and O1s spectra are shown in Figure 3.7 (b-d). The C1s peak for raw CNTs and annealed CNTs can be deconvoluted into and fitted by two sub-peaks. The major peak with a binding energy at 284.8 eV corresponds to sp^2 hybridized carbon atoms of the graphitic structure in the CNTs, while the minor peak at 285.8 eV is assigned to sp^3 hybridized carbon atoms bonded to oxygen²⁷. The sp^2 hybridized carbon contents are calculated to be 84.71, 82.52, 81.41, 80.25, 76.25% for raw CNTs and annealed samples A3, D3, A4 and A5, respectively (Table 3.1). There is only a small reduction of sp^2 carbon content in the annealed samples. Correspondingly, the O1s spectra can also be fitted into two peaks. The lower binding energy peak at 531.9 eV is assigned to be quinone groups (C=O); and the other peak at 533.2 eV belongs to ether groups (C-O-C)^{28, 29}. Closer examination of the functional group ratios summarized in Table 3.1 further reveals that increasing annealing temperature has larger influence on contents of C-O-C and C=O functional groups than that of increasing annealing duration (C1s Table 1). Data derived from O1s spectra in Table 3.1 show that the relative contents of -O- (related to C-O-C) and =O (related to C=O) are very different when annealed at 450, 500, and 550 °C. It is important to note that higher annealing temperature has clearly favoured the formation of ether groups (C-O-C) at the expense of quinone groups (C=O). For example, the C-O-C group percentage of sample A3 annealed at 450 °C is 16.40%. It increased to 23.13 % and 45.27% in samples A4 and A5, which were annealed at 500 and 550 °C, respectively. It is also noted that samples A4 (30min@500°C) and D3 (120min@450°C) have almost the same total oxygen content, i.e., 7.37 and 7.42 %. However, the C-O-C to C=O ratio in sample A4 is 0.30 while that in D3 is 0.23. These observations indicate that shorter duration/higher temperature annealing leads to more C-O-C groups than longer duration/lower temperature annealing, while the latter yields more C=O groups. Different from thermal annealing, oxidizing CNTs in strong acids leads to other types of functional groups. Apart from the main peak of graphitic sp^2 around 284.8 eV, acid treated CNTs also comprises of C-OH and COOH^{23, 30}, which are absent in our thermal annealed samples. The absence of these two functional groups is an important reason that thermally annealed CNTs has poorer dispersion in aqueous medium (compared with acid-treated CNTs), despite well dispersed in organic solvents.

Based on Raman and XPS analyses, we hereby propose a plausible reaction mechanism that involves the formation of surface ether and quinone groups on CNTs during thermal annealing, which are illustrated in Figure 3.8. To form C-O-C group, the first and also the determining step is the 1, 4 peroxidation. After that, the π electrons in the two adjacent C=C bonds rearrange and simultaneously form single bonds with the two oxygen atoms, while the -O-O- bond breaks homolytically. On the other hand, the formation of C=O groups begins with a 1, 2 peroxidation on the graphitic ring, and this is followed by simultaneous homolytic breaking of C-C and O-O bond, leading to the formation of two quinone groups. It is seen in XPS analysis that lower temperature is less favourable in generating C-O-C groups, i.e. less favourable to 1, 4 peroxidation. This is reasonable as the activation energy for 1, 4 peroxidation in the planar graphitic ring is higher than that of 1, 2 peroxidation.

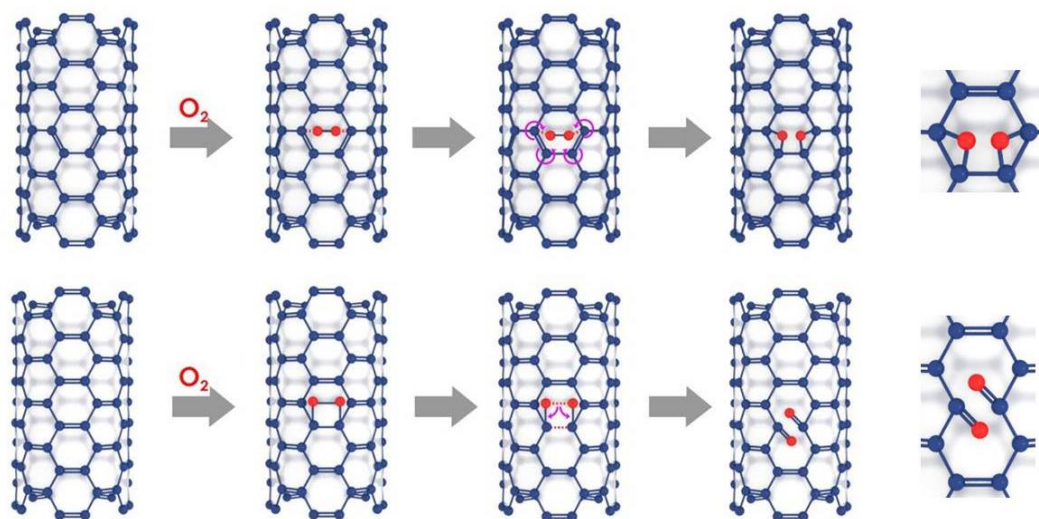


Figure 3.8 The proposed mechanisms of CNT surface functionalization via thermal annealing. The top part shows the formation of ether functional group, while the bottom part shows the formation of quinone group.

Enhanced dispersion of CNTs in organic solvents directly indicates the potential of readily incorporating the thermally functionalized CNTs into polymer matrices using conventional solution blending approach. To demonstrate such application, we compared composites with annealed CNTs and the raw CNTs dispersed in a PVDF matrix. Figure 3.9 compares the morphologies of the cryo-fractured morphologies of PVDF composites containing annealed CNT sample (sample D3) and raw CNTs (both 0.2 wt. %), prepared

by using DMF as the solvent. It can be seen that raw CNTs formed distinct and large aggregations in the polymer matrix (Figures 3.9 a and b), while annealed CNTs of sample D3 were individually separated and well dispersed throughout the polymer matrix (Figures 3.9 c and d). Achieving such a good dispersibility of CNTs in a polymer matrix is non-trivial and often requires lengthy and laborious treatment procedures that have poor scalability such as specialized grafting^{31, 32}.

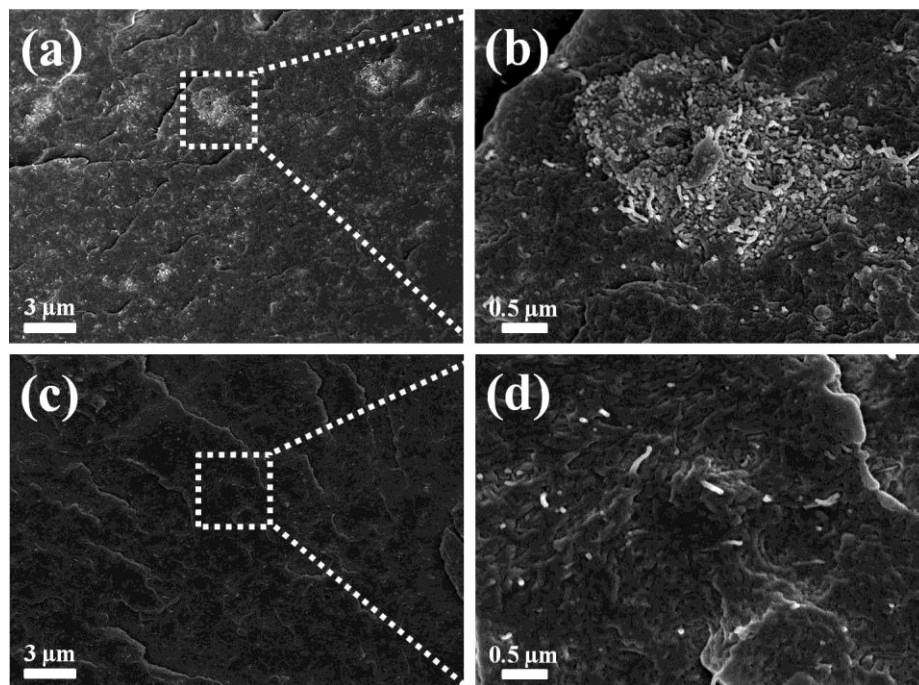


Figure 3.9 FESEM images showing the cryo-fractured morphologies of PVDF/CNTs composites with 0.2 wt. % (a, b) raw CNT and (c, d) annealed sample D3.

Good CNTs dispersion, with minimal structural damage, is particularly important for the applications of CNTs as conductive coating or circuitry. Inkjet printing represents one patterning technique that has been employed to fabricate conductive CNT films³³⁻³⁵. Despite the efforts, the difficulty to prepare uniformly dispersed CNT printing solution hinders this application. Previous works mostly used acid treated CNTs or surfactant to improve dispersion; however, these methods suffer from process complexity and compromise of electrical conductivity. To demonstrate the feasibility of using thermally functionalized CNTs as printing ink, ethanoic solutions containing annealed CNTs were drop-cast onto ITO patterned glasses, and electrical conductivity was tested. The

resistivity of 10 μL of annealed CNTs at 30min@ 500°C and raw CNTs without any treatment on ITO patterned glass are shown in figure 3.10. As shown also in the top-left inset are the optical microscopy images of samples with different ink volumes. It clearly shows that raw CNTs aggregated after the evaporation of solvent, and they stayed electrically insulated from each other on the ITO patterned glasses, due to the poor dispersion of raw CNTs and poor wetting to the substrate. The conductivity test shows that the pattern formed by raw CNTs is insulating until the feeding volume increased to 30 μL . By contrast, the thermally functionalized CNTs exhibited good pattern uniformity and obvious electrical conductivity, contributed by the oxygen-containing groups introduced during thermal annealing that enabled the good dispersion of CNTs in organic solvents and enhanced wetting to substrate. Again, it is shown that mild thermal annealing of CNT ensures the elimination of amorphous carbon, introducing functional groups and intactness of graphitic structures, which are critical in ensuring the high conductivity.

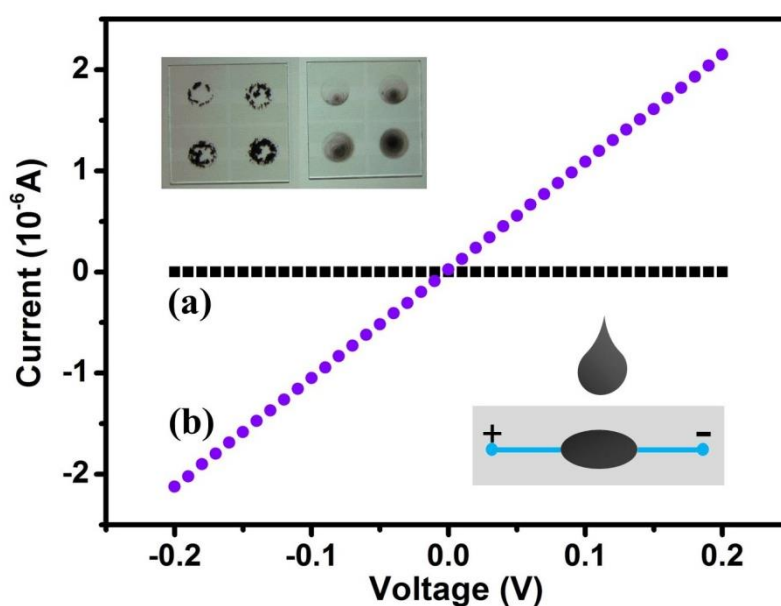


Figure 3.10 I-V curve of drop-cast raw CNTs and thermally functionalized CNTs (A4, 30 min@ 500°C) on ITO patterned glass. The drop volume is 10 μL . Top-left inset shows raw CNTs (left) and air annealed CNTs (right) with different volumes (10, 20, 30 and 50 μL) drop-cast on ITO

patterned glass. Bottom right inset shows the schematic of electrical testing of drop-cast CNTs pattern.

3.4 Conclusion

In this work, controlled mild thermal functionalization of CNTs was carried out and shown to be an effective route for surface modification of CNTs. This is a facile method which leads to high yield of annealed CNTs as high as 90%. After annealing at optimal temperature and duration, enhanced dispersion was demonstrated for the annealed CNTs in various organic solvents including ethanol, dimethyl formamide, chloroform and acetone. It was also shown that the controlled thermal annealing caused minimal damage to the graphitic structures of CNTs, as concluded from both Raman and TEM analysis. A plausible functionalization mechanisms related to surface chemistry is hereby proposed based on detailed Raman and XPS spectroscopic analyses, i.e. thermal annealing introduced uniform surface ether C-O-C and quinone C=O groups on CNT surface. We further demonstrated that thermal annealing is scalable and the resultant CNTs can be readily used for preparing CNT/polymer composite and fabricating printed electronics. This facile and scalable treatment process for CNTs opens up a lot of opportunities of wide range of applications that require uniformly dispersion CNTs within an organic media.

References

1. R. H. Baughman, A. A. Zakhidov and W. A. de Heer, *Science*, 2002, **297**, 787-792.
2. A. Bachtold, P. Hadley, T. Nakanishi and C. Dekker, *Science*, 2001, **294**, 1317-1320.
3. S. Ren, M. Bernardi, R. R. Lunt, V. Bulovic, J. C. Grossman and S. Gradecak, *Nano letters*, 2011, **11**, 5316-5321.
4. S. Qin, D. Qin, W. T. Ford, J. E. Herrera, D. E. Resasco, S. M. Bachilo and R. B. Weisman, *Macromolecules*, 2004, **37**, 3965-3967.
5. Z. Spitalsky, D. Tasis, K. Papagelis and C. Galiotis, *Progress in Polymer Science*, 2010, **35**, 357-401.
6. I. Mazov, V. L. Kuznetsov, I. A. Simonova, A. I. Stadnichenko, A. V. Ishchenko, A. I. Romanenko, E. N. Tkachev and O. B. Anikeeva, *Applied Surface Science*, 2012, **258**, 6272-6280.
7. J. Chen, H. Liu, W. A. Weimer, M. D. Halls, D. H. Waldeck and G. C. Walker, *Journal of the American Chemical Society*, 2002, **124**, 9034-9035.
8. A. Star, J. F. Stoddart, D. Steuerman, M. Diehl, A. Boukai, E. W. Wong, X. Yang, S. W. Chung, H. Choi and J. R. Heath, *Angewandte Chemie International Edition*, 2001, **40**, 1721-1725.
9. B. Bhushan, *Springer handbook of nanotechnology*, Springer Science & Business Media, 2010.
10. K. L. Klein, A. V. Melechko, T. E. McKnight, S. T. Retterer, P. D. Rack, J. D. Fowlkes, D. C. Joy and M. L. Simpson, *Journal of Applied Physics*, 2008, **103**, 061301.
11. K. Behler, S. Osswald, H. Ye, S. Dimovski and Y. Gogotsi, *Journal of Nanoparticle Research*, 2006, **8**, 615-625.
12. C. H. Lau, R. Cervini, S. R. Clarke, M. G. Markovic, J. G. Matison, S. C. Hawkins, C. P. Huynh and G. P. Simon, *J. Nanopart. Res.*, 2008, **10**, 77-88.
13. S. Yang, X. Wang, H. Yang, Y. Sun and Y. Liu, *Journal of hazardous materials*, 2012, **233**, 18-24.
14. C. Li, D. Wang, T. Liang, X. Wang, J. Wu, X. Hu and J. Liang, *Powder Technol.*, 2004, **142**, 175-179.

15. M.-K. Seo and S.-J. Park, *Current Applied Physics*, 2010, **10**, 241-244.
16. S.-C. Kung, K. C. Hwang and I. N. Lin, *Applied physics letters*, 2002, **80**, 4819-4821.
17. B. Zeng, G. Xiong, S. Chen, W. Wang, D. Wang and Z. Ren, *Applied physics letters*, 2006, **89**, 223119.
18. G. Mercier, J. r. m. Gleize, J. Ghanbaja, J.-F. o. Marêché and B. Vigolo, *The Journal of Physical Chemistry C*, 2013, **117**, 8522-8529.
19. Y.-R. Shin, I.-Y. Jeon and J.-B. Baek, *Carbon N Y*, 2012, **50**, 1465-1476.
20. M. Pimenta, G. Dresselhaus, M. S. Dresselhaus, L. Cancado, A. Jorio and R. Saito, *Physical Chemistry Chemical Physics*, 2007, **9**, 1276-1290.
21. K. R. Moonosawmy and P. Kruse, *The Journal of Physical Chemistry C*, 2009, **113**, 5133-5140.
22. S. Osswald, E. Flahaut, H. Ye and Y. Gogotsi, *Chemical Physics Letters*, 2005, **402**, 422-427.
23. S. Roy, T. Das, C. Y. Yue and X. Hu, *ACS applied materials & interfaces*, 2013, **6**, 664-670.
24. X.-Z. Tang, Z. Cao, H.-B. Zhang, J. Liu and Z.-Z. Yu, *Chem. Commun.*, 2011, **47**, 3084-3086.
25. X.-Z. Tang, X. Li, Z. Cao, J. Yang, H. Wang, X. Pu and Z.-Z. Yu, *Carbon*, 2013, **59**, 93-99.
26. O. C. Compton, D. A. Dikin, K. W. Putz, L. C. Brinson and S. T. Nguyen, *Advanced Materials*, 2010, **22**, 892-896.
27. Z. Luo, S. Lim, Z. Tian, J. Shang, L. Lai, B. MacDonald, C. Fu, Z. Shen, T. Yu and J. Lin, *Journal of Materials Chemistry*, 2011, **21**, 8038-8044.
28. L. Zhang, L. Ji, P.-A. Glans, Y. Zhang, J. Zhu and J. Guo, *Physical Chemistry Chemical Physics*, 2012, **14**, 13670-13675.
29. S. Biniak, G. Szymański, J. Siedlewski and A. Świątkowski, *Carbon*, 1997, **35**, 1799-1810.
30. K. Haubner, J. Murawski, P. Olk, L. M. Eng, C. Ziegler, B. Adolphi and E. Jaehne, *ChemPhysChem*, 2010, **11**, 2131-2139.
31. S. Roy, T. Das, Y. Ming, X. Chen, C. Y. Yue and X. Hu, *Journal of Materials Chemistry A*, 2014, **2**, 3961-3970.

32. H.-J. Lee, S.-J. Oh, J.-Y. Choi, J. W. Kim, J. Han, L.-S. Tan and J.-B. Baek, *Chemistry of materials*, 2005, **17**, 5057-5064.
33. O.-S. Kwon, H. Kim, H. Ko, J. Lee, B. Lee, C.-H. Jung, J.-H. Choi and K. Shin, *Carbon*, 2013, **58**, 116-127.
34. K. Kordás, T. Mustonen, G. Tóth, H. Jantunen, M. Lajunen, C. Soldano, S. Talapatra, S. Kar, R. Vajtai and P. M. Ajayan, *Small*, 2006, **2**, 1021-1025.
35. M. Singh, H. M. Haverinen, P. Dhagat and G. E. Jabbour, *Advanced materials*, 2010, **22**, 673-685.

Chapter 4 Mechanical Properties of PVDF/CNTs Composites

The reinforcement of mechanical properties of polymeric materials is often important to widen the applications; however, it remains a technical challenge to effectively increase toughness without degrading stiffness and strength of the polymers. In this work, by a facile methodology combining solution mixing and melt blending, poly (vinylidene fluoride)/multi-walled carbon nanotubes (PVDF/MWCNTs) composite with exceptionally enhanced ductility and toughness are prepared. With only 0.2 wt. % CNT loading, the elongation at break has increased from originally 138% to almost 500%, while toughness improved by as much as 386%, without compromising the stiffness and strength. Note that raw CNTs are directly dispersed in the matrix without any surface modification. In order to elucidate this novel enhancement of ductility of PVDF/MWCNTs composites, we carried out detailed analyses based on results from ultra-small-angle X-ray scattering (USAXS), cryo-fractured surface morphology, differential scanning calorimetry (DSC), and Fourier transform infrared spectroscopy (FTIR). It is proposed the enhanced ductility to be contributed by a synergistic combination of “void pinning effect” of CNT, as well as the formation of γ phase polymorph as the interphase in the PVDF/CNTs composites.

4.1 Introduction

Poly (vinylidene fluoride) (PVDF) has received much research attention in the past few years for its unique piezoelectric and pyroelectric properties.^{1, 2} Owing to its excellent mechanical properties, thermal and chemical resistance, PVDF has also been utilized as structural material in architectural, automotive, and chemical processing industry.³⁻⁵ In view of the widening applications of PVDF, it is highly desirable to improve its mechanical properties by employing facile and scalable methods. Carbon nanotube (CNT), contributed by its excellent functional and mechanical properties, represents one type of nano-fillers that has been extensively explored to reinforce polymer matrices.⁶

In this study, we report the fabrication of highly ductile PVDF/MWCNT composites prepared via a facile method combining solution mixing and melt extrusion. Excellent dispersion of raw MWCNTs in PVDF was achieved without the need of any surface functionalization of CNTs. Contrary to the usual cases; in our work, substantial enhancement in ductility by 400% in the PVDF/MWCNT composites with little change of modulus and yield strength were achieved. Seeing the counterintuitive enhancement of ductility observed in these PVDF/MWCNT composites, we carried out investigation on contributing mechanisms by characterizing systematically the void formation, interphase formation, phase transition during deformation, as well as filler-induced PVDF crystal polymorphism with and without the presence of MWCNTs during deformation.

4.2 Experiments

4.2.1 Sample Preparation

To identify the appropriate method to fabricate PVDF/CNTs composites with uniform morphology, three approaches were employed in this study. First, melt extrusion was used to prepare PVDF/CNTs composites. Initially, the CNTs powder and PVDF powder were pre-mixed before extrusion. After 10 mins extrusion at 190 °C, the products were hot pressed into thin films with 0.2 mm thickness. Solution blending was also used to prepare PVDF/CNTs composites. CNTs dispersed in acetone were processed with high

power sonication (ultrasonic processor VCX 130, SONICS) in 50 ml acetone for 5 mins by cooling using ice-water bath. At the same time, PVDF was dissolved in acetone. Afterwards, the two solutions were mixed by magnetic stirring for 1 hour and bath sonication for 2 hours. PVDF/CNTs can be obtained by casting the mixed solution in the petri-dish and evacuating the solvents. After that, the obtained products were hot pressed into thin films with 0.2 mm thickness. In the third approach, CNTs with calculated contents (0, 0.1, 0.2, 0.5 and 1.0 wt. %) were processed with high power sonication in 50 ml acetone for 5 mins with ice-water bath. After that, dissolved PVDF in 50 ml acetone was mixed with CNTs solution by magnetic stirring for 1 hour and bath sonication for 2 hours. The uniform PVDF/CNTs/acetone solution was subjected to solvent evaporation at room temperature, followed by drying in vacuum oven at 60 °C overnight to completely evacuate the residue solvent. The products obtained were extruded at 190 °C, 80 rad/minute for 10 mins. The obtained composites were then pressed into thin films with thickness around 0.2 mm by hot-press at 240 °C for further characterizations. To study the interfacial strength between CNT and polymer matrix, the as prepared PVDF/MWCNTs composite were Soxhlet extracted in boiling acetone for 72 h using the method described previously ⁷ before examining with an electron microscope. Specific section of stretched PVDF and its composite samples were etched in mixed solution of sulfuric and phosphorus pentoxide to investigate the structural evolution under strain.

4.2.2 Characterizations

The morphology of prepared samples was studied with a field emission scanning electron microscope (FESEM). SEM samples were prepared by firstly immersing samples inside liquid nitrogen to prepare cryo-fractured surface and then coated with platinum for 45 s before investigated by JEOL JSM-7600F. Mechanical properties were tested with Microtester Instron 5848. Attenuated total reflectance - Fourier transform infrared spectroscopy (ATR-FTIR) spectra were recorded by PerkinElmer Frontier FT-NIR/MIR spectrometers. Spectra were obtained with resolution of 2 cm⁻¹ and 16 scans. X-ray diffraction (XRD) was performed on a Bruker AXS D8 advance X-ray diffractometer using Cu K α radiation. Differential scanning calorimetry (DSC) was performed from 50

to 200 °C with a heating rate of 10 °C/min by TA Instruments 2010. Ultra small X-ray scattering (USAXS) experiments were carried out by a modified Xeuss system of XENOCS with a semiconductor detector (Pilatus 100K, DECTRIS, Swiss) attached to a multilayer focused Cu K α X-ray source (GeniX3D Cu ULD, Xenocs SA, France), generated at 50 kV and 0.6 mA. The wavelength of the X-ray is 0.154 nm. The beam was collimated with a two scatterless slits systems mounted 2.4 meters away from each other. The distance between the sample and detector is 6450 mm, with exposure time of 600 s and beam size of 0.6*0.6 mm².

4.3 Results and Discussion

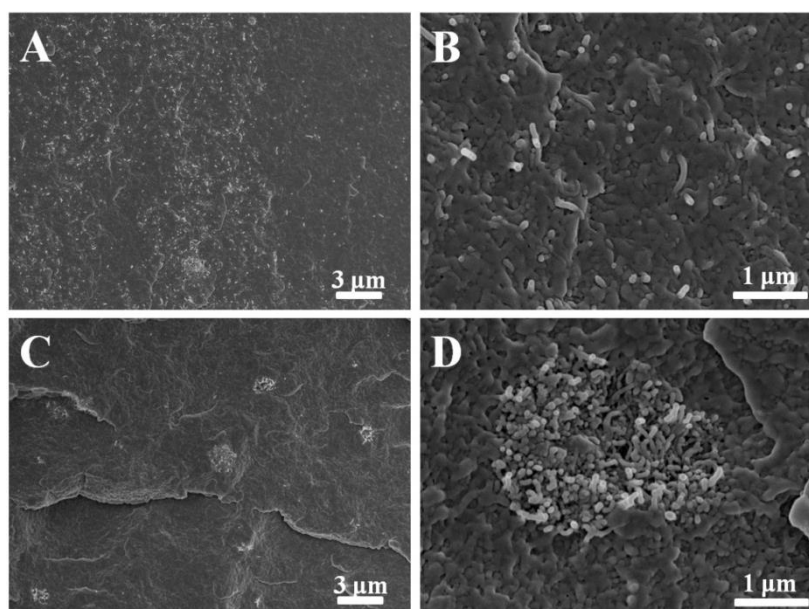


Figure 4.1 FESEM images of the cryo-fractured surface of PVDF/MWCNTs composites prepared from solution blending (A, B) and melt extrusion (C, D) with CNTs loading 0.2 wt. %.

Figure 4.1 shows the cryo-fracture surfaces of PVDF/MWCNTs composites prepared from solution blending and melt extrusion. With only solution blending, the CNTs cannot be well distributed in the polymer matrix, some regions possessing higher concentration CNTs than others, see Figure 4.1A. From enlarged image in Figure 4.1B, however, we observe that most of the tubes are individually dispersed. It suggests that the high power sonication is very effective in dispersing the CNTs in acetone. Due to the difference

between the density of CNTs and PVDF solution, CNT separation phenomenon occurs during solvent evaporation process. Accompany by heating induced polymer solution flow, the poor CNT distribution may happen. The method using melt extrusion only form CNT aggregates with diameter in several micrometers (Figure 4.1 C and D) although it seems that the aggregated particles are quite well dispersed, indicating melt extrusion only is not capable of individually dispersing CNTs.

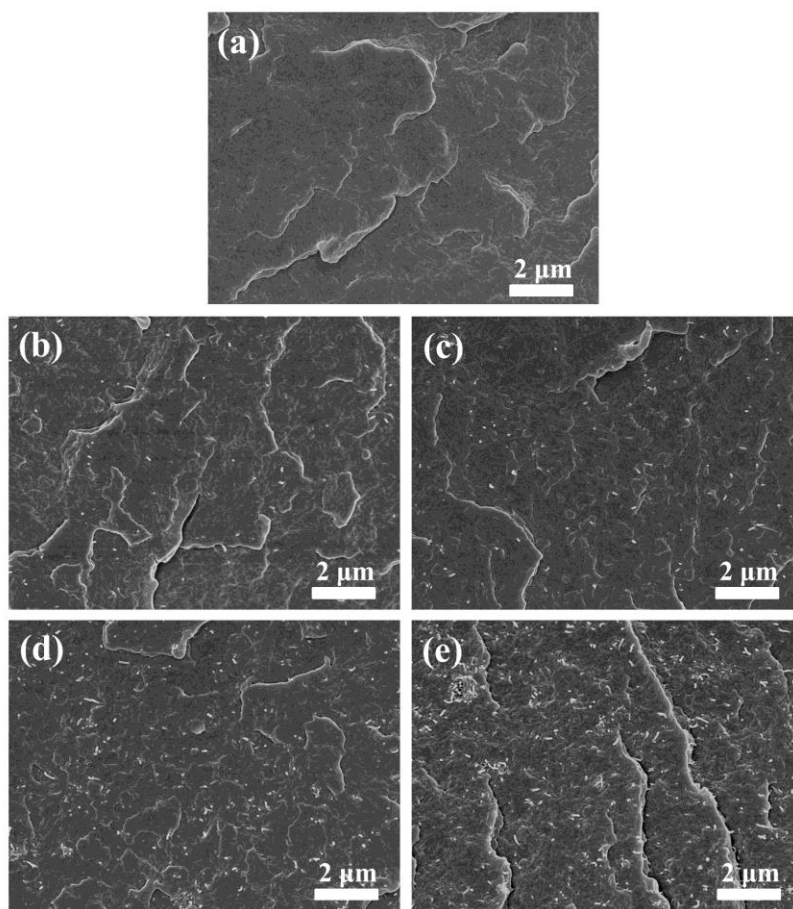


Figure 4.2 FESEM images of the cryo-fractured surface of (a) raw PVDF and PVDF/MWCNTs composites with CNTs loading of (b) 0.1 (c) 0.2 (d) 0.5 and (e) 1.0 wt. %, respectively.

A uniform dispersion was obtained by the third strategy, see Figure 4.2. Overall, uniform dispersion of raw CNTs was achieved in all samples prepared by our method. Such excellent dispersion of untreated MWCNT in a polymer matrix is rarely seen in literature. The internal morphology of the composites is important because it directly determines the mechanical and many other physical properties. Aggregation of CNTs could severely

deteriorate the mechanical performance of final products due to undesirable localized stress.

Table 4.1 Summarized mechanical data of PVDF/CNTs composites.

CNT Content (wt. %)	Young's Modulus (MPa)	Yield Stress (MPa)	Elongation at Break (%)
0	504 (15) ^a	47.5 (1.0)	128 (81)
0.1	457 (38)	46.0 (1.7)	411 (89)
0.2	491 (23)	45.8 (0.8)	483 (24)
0.5	532 (17)	46.6 (0.3)	361 (101)
1.0	551 (24)	47.3 (1.0)	113 (85)

^a: Values in parenthesis are the standard deviation. At least five samples for each composite condition were tested.

Table 4.1 shows the mechanical data obtained from tensile test of neat PVDF and its CNTs composites. It is seen that, for the modulus, there is a slight initial decrease followed by an increase after the introduction of CNTs into PVDF. The yield stresses of all composite samples are marginally lower than that of the neat polymer. Interestingly, the elongation at break has increased to 411, 483 and 361% for samples with 0.1, 0.2 and 0.5 wt. % CNT, as compared with that of neat polymer. Such substantial improvement of ductility without compromise in modulus and strength has never been reported previously in CNTs reinforced polymers.

Figure 4.3 (a) shows representative stress-strain curves of neat PVDF and composite with 0.2 wt. % CNT content. The elongation at break of neat PVDF is 128 %, while that of the composite sample increased to 483%. The peak in the stress-strain curve around 230 % is due to non-equilibrium necking during the stretching process. As a result of greatly increased ductility and comparable modulus and strength, the toughness of the composite samples (defined as the area under stress-strain curve) has significantly increased. The bar diagram in Figure 4.3 (b) shows the toughness increments of all CNTs composites as compared with that of neat PVDF; the normalized increment of tensile toughness of composite with CNT loading of 0.1, 0.2 and 0.5 wt. % are 291, 386 and 298 %, respectively.

respectively. With as low as only 0.2 wt. % pristine CNTs, the tensile toughness almost quadrupled. This is non-trivial and exceptional, requiring further research effort to investigate the underlying mechanism. Nevertheless, with further increase of CNTs up to 1.0 wt. %, toughness decreased due to the poorer dispersion of CNT at higher loading that leads to decreased elongation at break.

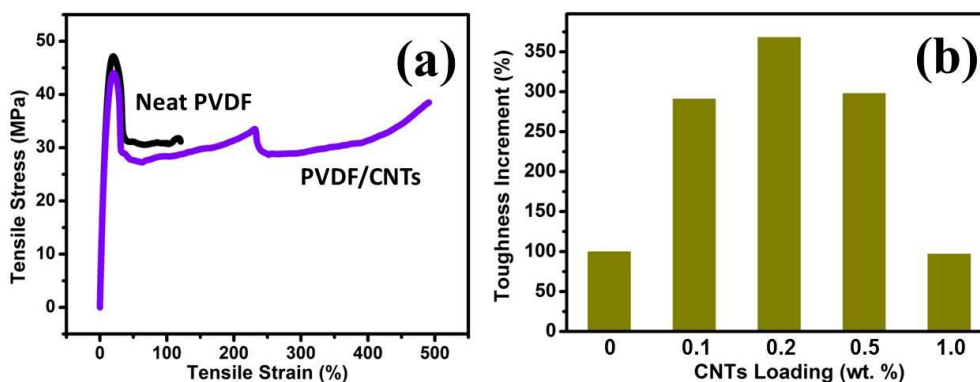


Figure 4.3 (a) Typical tensile test curves of neat PVDF and PVDF/CNTs composite sample with 0.2 wt. % CNTs and (b) tensile toughness improvements of composites compared with neat PVDF.

The reinforcement effect of CNTs on polymer modulus/strength is widely reported and discussed. However, CNTs induced improvement of ductility is very rare in the literature. The understanding of the mechanism behind the enhanced ductility is highly desirable for both academic interests and practical applications. It is well accepted that plasticizer or debonding/cavitation can both contribute to increased ductility.⁸⁻¹⁰ The plasticizer effect may originate from solvent, moisture, or low molecular weight additives. In our work, since the fabrication processes employed for neat PVDF and PVDF composite samples were the same, the possibility of solvent plasticizing effect is eliminated. TEM image that shows the morphology of composite sample after tensile test reveals that most of the CNTs are not de-bonded from PVDF matrix. In addition, FESEM images of cryo-fractured surface of tensile deformed sample in the transverse direction shows that even after stretching, the polymer matrix is still well coated on the surface of CNTs, further eliminating debonding as the factor. A previously reported simulation study on CNTs reinforced polymers stated that the stress-strain curve can be very sensitive to any

debonding process and its occurrence would lead to a stress downturn or strain softening.¹¹ However, no such strain softening was observed in our tensile testing results, which again eliminates the possibility of debonding induced ductility.

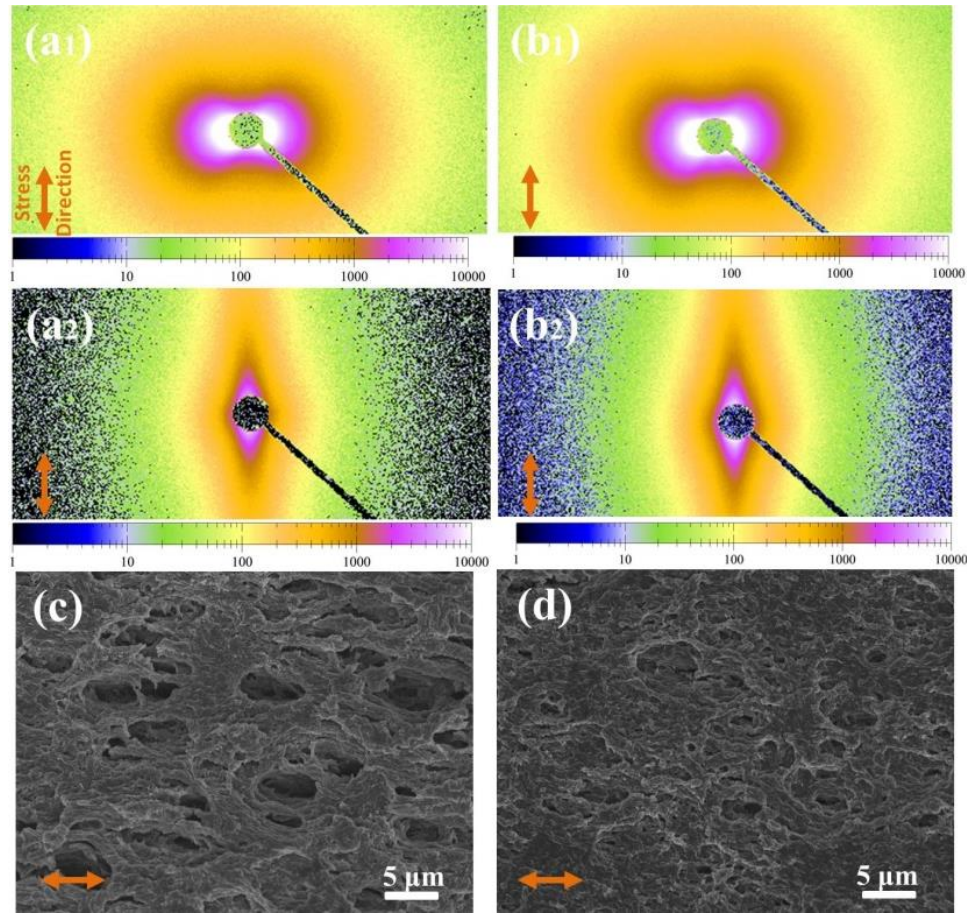


Figure 4.4 USAXS scattering patterns of (a1) neat PVDF, 30 % strain; (b1) composite sample with 0.2 wt. % CNTs, 30 % strain; (a2) neat PVDF, 60 % strain; (b2) composite sample with 0.2 wt. % CNTs, 150 % strain and FESEM of necking section of (c) neat PVDF and (d) composite sample with 0.2 wt. % CNTs. To enable a clearer observation of morphological profile, both neat PVDF and composite sample are etched in oxidative solution of P_2O_5/H_2SO_4 before doing SEM. The arrows indicate the uniaxial stretching direction.

Aravind et al.¹⁰ prepared thermoplastic polypropylene with incubated pre-existent submicrometer voids and found that the voids growth resulted in the formation of energy-absorbing crazes, which could delay the fracture of polymer. In order to fully understand

the effect of voids toward the mechanical properties of the PVDF/CNTs composites during stretching, in-situ USAXS analysis was carried out and the results are shown in Figure 4.4. It is seen that both neat PVDF and PVDF/CNTs composites possess abundant micrometer sized voids after tensile deformation, evidenced by the strong X-ray scattering intensity. This indicates that the exceptional ductility in our PVDF/CNT composite, which was not observed in neat PVDF, is not directly contributed by voids. In fact, as discussed earlier, CNTs debonding from the PVDF matrix after deformation is rarely seen, indicating negligible influence from debonding promoted voids formation, even if it takes place. In other words, CNTs do not cause the formation of voids in this study. It was also observed that when the deformation is small (Figure 4.4 a1 and 4.4 b1), microvoids in both samples align along the direction that is vertical to the stress direction. As the deformation increases (Figure 4.4 a2 and 4.4 b2), voids switched into the direction parallel to the stress in both neat PVDF and PVDF/CNT composites. Generally, microvoids are created with tips in the direction vertical to stress and develop along the stress direction. Despite that plenty of voids which are present in both neat PVDF and PVDF/CNT composite, we observed an obvious difference in the morphologies of necking section of the two deformed samples. It is seen that, from Figure 4.4 c and 4.4 d, the void size of neat PVDF is noticeably larger than that of PVDF/CNT composite. The size of the voids in neat PVDF are around 5 μm , while that of composite sample is several times smaller (1~2 μm).

The void growth behavior observed in both USAXS and SEM analysis suggest the role of CNTs in improving the ductility and toughness of PVDF composites via delaying the voids coalescence. The introduction of CNTs may hinder the development of voids, delaying them from further growth. Consequently, before the breakage, PVDF/CNT composites could absorb more energy, corresponding to enhanced ductility and tensile toughness. The difference in void growth found in neat PVDF and PVDF/CNTs composites is illustrated in Figure 4.5. For stretching of neat PVDF, perpendicular microvoids grow and realign towards the direction parallel to the stress direction (Figure 4.5, corresponding to the transition from Figure 4.4 a1 and Figure 4.4 a2). Since there is no restriction, the propagating microvoids eventually coalesce with neighboring voids, forming larger voids and resulting in final failure. In the case of PVDF/CNT composites,

CNTs in the path of crack propagation can pin and impede the growth, which slow down the coalescence of microvoids. After the initial propagating microvoids encounter CNTs, the fusion of neighboring voids is hindered. At the same time, more CNTs may realign parallel to the stress direction and becoming more effective in hindering voids growth. As a result, the formation and growth of voids will be delayed, hence leading to enhanced ductility and toughness.

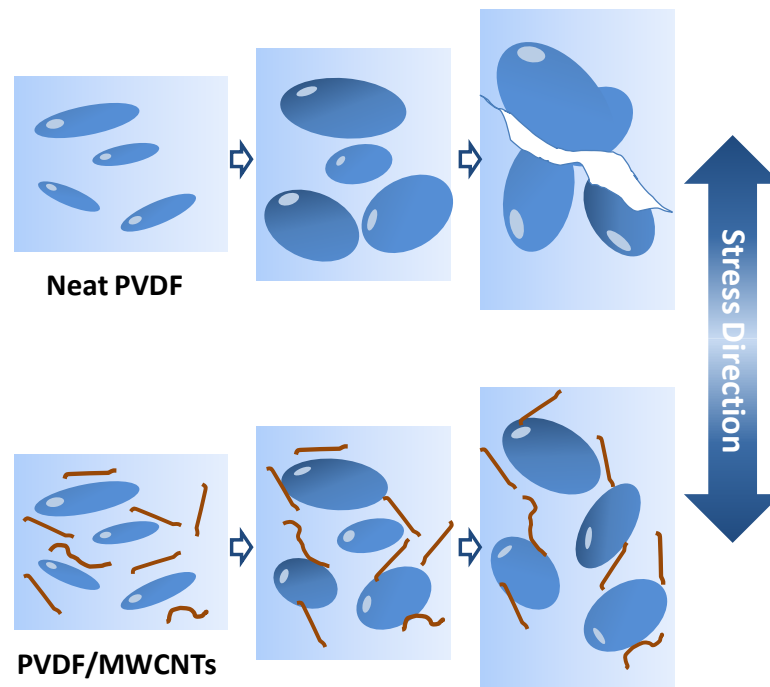


Figure 4.5 Illustration of the proposed mechanism of CNT pinning effect. The breakage of neat PVDF is caused by void development and coalescence under stress, while the realigned CNTs in PVDF/CNTs composite pin and impede the coalescence of voids, delaying the failure.

Apart from void pinning effect of CNTs, the complex polymorphs of PVDF with different crystalline structures have to be considered. Owing to the substantial difference in modulus and ductility among each crystalline phases, any variations in the ratio of PVDF crystal structures is expected to exert considerable influence on physical properties of PVDF composites.^{12, 13} There are altogether five forms of chain arrangements of PVDF, among which, α , β , and γ are the most frequently observed and studied. α phase is the most thermodynamically stable phase and with a chain conformation of TGTG' (trans-

gauche-trans-gauche); β phase has a chain conformation of TTTT (all trans) that is the main origin of the piezoelectric properties.¹⁴ For γ phase, it has a chain sequence of TTTGTTTG' and is the transition state between α and β .¹⁵ To investigate the effects of PVDF polymorphs on enhanced ductility, ATR-FTIR, XRD, and DSC were carried out to understand the polymorphic transformation during the tensile stretching process.

Figure 4.6 (a) and (b) shows the DSC curves of neat PVDF and its composites before and after tensile testing, respectively. Two peaks are found in the DSC curve of neat PVDF before deformation. The weak endotherm peak at lower temperature of 148 °C is due to imperfect crystals formed in the process of melt crystallization.¹⁶ The endotherm peak at 161 °C is attributed to α phase melting. For composite samples at all CNT loadings, a new shoulder peak at higher temperature of 167 °C emerged, which is the melting peak of γ phase PVDF. As summarized in Table 4.2 are the melting points of each phase and the crystallinities of neat PVDF and composites, as obtained from DSC curves. Crystallinity was calculated by integrating the heat flow between 130 and 175 °C. The melting temperature of α phase barely alters with the increase of CNT loading, and is unaffected by tensile stretching. Melting temperature of γ crystallite remains comparable at different CNT contents. The crystallinities of as prepared PVDF composites, regardless of the different phases, decrease with the introduction of CNTs. However, the variations are very marginal. For example, the crystallinity of composite sample with 0.2 wt. % CNTs is only 0.5 % less than that of neat PVDF. The difference in crystallinity is even smaller if the contents of CNTs are taken into account. The slightly reduced crystallinity could be partially responsible for the moderate change of modulus of composites. Furthermore, since γ crystallites possess much lower elastic modulus than that of α and β phase,¹⁷ the existence of γ phase in composites may also affect the modulus. It is also seen from Figure 4.6 (b) that the γ phase melting peak disappears after stretching, indicating the transformation into other phases.

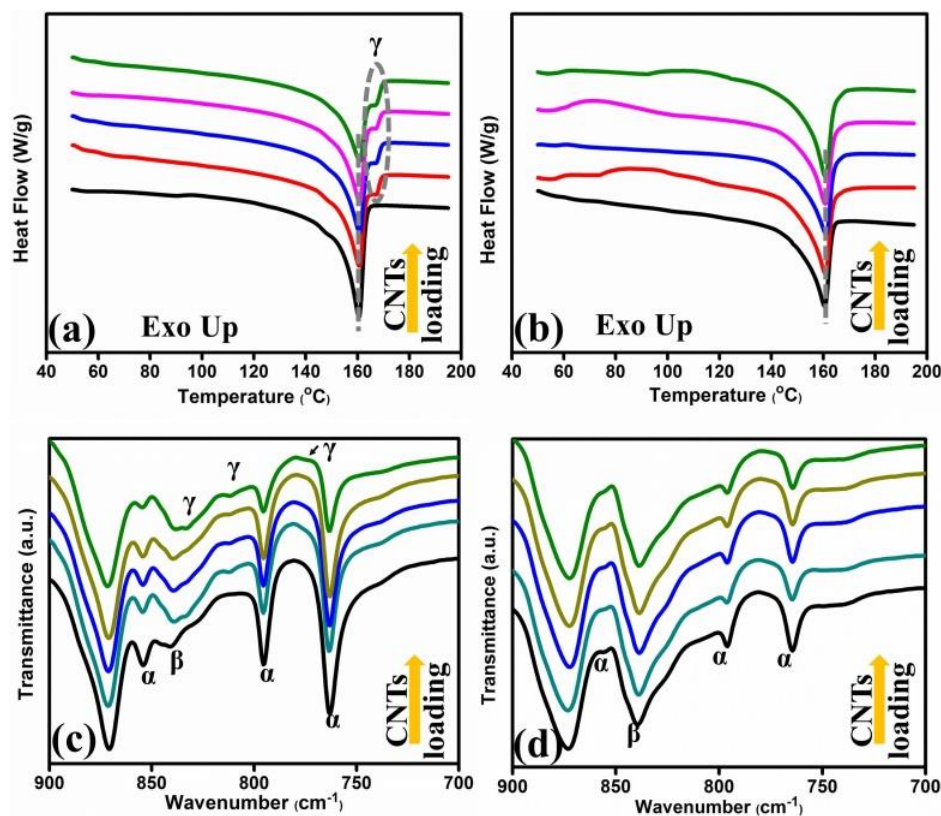


Figure 4.6 First heating DSC curves of PVDF/CNTs composites before (a) and after (b) tensile test and FTIR spectrum of PVDF/CNTs composites before (c) and after (d) tensile test. Curves from the bottom to top are spectrum of samples with 0, 0.1, 0.2, 0.5 and 1.0 wt. % CNT, respectively.

Table 4.2 Summary of the melting temperature and crystallinity of α and γ PVDF before and after stretching, as determined by DSC. Enthalpy was calculated by integrating the heat flow between 130 and 175 °C by TA Analysis software and the fusion heat of 100 % crystallinity is 102.5 J/g.¹⁸

CNT content (wt. %)		0	0.1	0.2	0.5	1.0
$T_m(\alpha/\beta)$ (°C)	Before stretching	160.6	160.7	160.9	160.9	160.9
	After stretching	160.7	160.9	161.1	160.9	160.9
$T_m(\gamma)$ (°C)	Before stretching	—	167.5	167.3	167.3	167.1
	After stretching	—	—	—	—	—
Crystallinity	Before stretching	34.0	33.0	33.5	33.2	32.5
	After stretching	34.7	36.6	35.6	34.7	38.8

FTIR is a useful tool that is frequently employed to differentiate each type of crystal in PVDF. Figure 4.6 (c) shows the ATR-FTIR spectra of as-prepared neat PVDF and the corresponding CNT composites. FTIR peaks at 855, 796 and 764 cm^{-1} belonging to α crystallite are clearly seen in the spectra of both neat PVDF and composites. With the increase of CNTs loading, absorption of α crystallite decreases gradually, indicating decreased α phase in the composites. There is one peak at 840 cm^{-1} with weak intensity observed in FTIR spectra for both PVDF and CNT composites. Since both β and γ phases may absorb at this wavenumber range, the origin of this peak cannot be determined at this point without further information. However, it is clear that a new peak at 833 cm^{-1} that exclusively belongs to γ crystallite¹⁹ emerged for the composite samples, which is absent in the spectrum of neat PVDF. Additionally, absorptions at 812 and 716 cm^{-1} also come from γ phase, although the peak at 716 cm^{-1} is relatively weak. The peak at 840 cm^{-1} is attributed to β crystallite and its absorption increases after CNTs were introduced (Figure 4.6 c). This is consistent with other works that reported increased β phase after addition of nanomaterials into PVDF, such as nanoclay^{20, 21} and various types of CNTs.^{22, 23} The zigzag surface of CNTs is believed to match well with all-trans configurations, which are beneficial to β PVDF growth formation.²⁴ This is further supported by simulation²³ that showed all-T configurations (β phase) are more favorable to be adsorbed onto the surface of CNT compared with TGTG' configuration. Molecules of α configuration are able to transform into β PVDF with the help of external energy input, for example via simple sonication. Since the γ phase is a transitional structure between α to β crystallite, it is reasonable that a portion of molecules on CNTs remain in γ configuration in the process of α/β transformation. γ PVDF is known to be crystallizing in the vicinity of the melting α phase.²⁵ Contributed by the melt crystallization occurred during both the melt extrusion and hot press processes we used, γ phase PVDF would form in the composites.

From Figure 4.6 (d), it can be seen that, after the tensile test, all the α PVDF peaks decrease while that of the β phase at 840 cm^{-1} increases markedly, owing to the α to β transformation induced by stretching.²⁶ It is also noted that all absorptions of γ phase at 840, 812 and 776 cm^{-1} disappear after the stretching, indicating transformation of γ phase during the tensile test, consistent with DSC results. The transformation of γ phase, which is only present in composites during stretching, was also evidenced by XRD. In another

words, based on the high similarity in chain configurations between β and γ PVDF, the γ PVDF transforms into β phase during stretching, similar to what was reported previously.²⁷ A separate simulation study²⁸ demonstrated that the phase transformation can be achieved in the way of interchain slippage, particularly along the molecule chain at the interface. As schematically illustrated in Figure 4.7, the γ phase slips into β phase under external load, where continuous slippage and transformation of γ phase create a plasticized zone around the β/γ phase interface in the vicinity of CNTs. This phase transformation induced plasticization leads to significant enhancement of ductility and absorb large amount of energy during stretching. On the other hand, the phase transformation induced plasticization reduces the stress transfer between the CNT and PVDF matrix and delay the fracture of CNTs, thus affect adversely to the performance of modulus and yield strength of the composites.

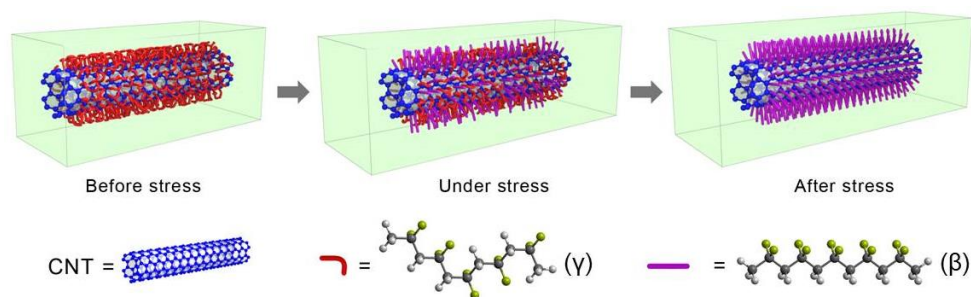


Figure 4.7 Illustration of the proposed mechanism of polymorphic transformation-induced ductility. Under stress, the γ phase in PVDF/CNTs composite around CNTs transform into β phase, creating plasticization and resulting in enhanced ductility and toughness.

The findings in this study show that CNT is not only able to reinforce polymeric matrix in terms of Young's modulus and tensile strength; it can also remarkably enhance the ductility of the PVDF composites. With low CNT loading, remarkably enhanced ductility was achieved in this study. The function of CNTs in PVDF matrix is two-fold. Firstly, CNTs serve as sites for void pinning during the stretching process. Secondly, the introduction of CNTs creates an interfacial PVDF crystal γ phase between the nanotube surface and the matrix, which undergoes polymorphic transformation under stretching. The synergistic effect of void pinning and interfacial phase transformation leads to exceptionally improved ductility and toughness in PVDF/CNTs composites.

4.4 Conclusions

In summary, exceptionally ductile PVDF/MWCNTs composites with excellent dispersion of raw CNT in PVDF matrix have been prepared via a facile method combining solution mixing and melt blending. The highly ductile PVDF/MWCNTs composites were achieved without compromising the yield strength and modulus. The mechanism of such unique and counterintuitive ductility change is systematically investigated using various characterization techniques. SAXS revealed that CNTs acts as void pinning sites that hinder the propagation of microvoids, preventing their further coalescence. Furthermore, the polymorphic transformation was found to be another main contributing factor. In our system, γ phase PVDF in as-prepared composite samples disappeared and transformed into β crystallite during the stretching, creating plasticized zone around CNTs. This plasticization led to significant increase of ductility and toughness of the resultant composites. These types of highly ductile PVDF/CNT composite with exceptional toughness are believed to be able to find wide potential for engineering applications.

References

1. R. Kepler and R. Anderson, *Journal of Applied Physics*, 1978, **49**, 1232-1235.
2. K. Koga and H. Ohigashi, *Journal of Applied Physics*, 1986, **59**, 2142-2150.
3. S.-c. Lin, M. Coates, E. M. Pearce and P.-t. Huang, *Journal*, 2004.
4. M. Khayet, G. Chowdhury and T. Matsuura, *AIChE journal*, 2002, **48**, 2833-2843.
5. Z. Cui, E. Drioli and Y. M. Lee, *Progress in Polymer Science*, 2014, **39**, 164-198.
6. Z. Spitalsky, D. Tasis, K. Papagelis and C. Galiotis, *Progress in Polymer Science*, 2010, **35**, 357-401.
7. H. Xia, Q. Wang and G. Qiu, *Chemistry of materials*, 2003, **15**, 3879-3886.
8. D. Notta - Cuvier, M. Murariu, J. Odent, R. Delille, A. Bouzouita, J. M. Raquez, F. Lauro and P. Dubois, *Macromolecular Materials and Engineering*, 2015.
9. P. Ma, A. Spoelstra, P. Schmit and P. Lemstra, *European Polymer Journal*, 2013, **49**, 1523-1531.
10. A. Dasari, Q.-X. Zhang, Z.-Z. Yu and Y.-W. Mai, *Macromolecules*, 2010, **43**, 5734-5739.
11. A. Needleman, T. Borders, L. Brinson, V. Flores and L. Schadler, *Composites Science and Technology*, 2010, **70**, 2207-2215.
12. Y. Pei and X. C. Zeng, *Journal of Applied Physics*, 2011, **109**, 093514.
13. P. Corradini and G. Guerra, in *Macromolecules: synthesis, order and advanced properties*, Springer, 1992, pp. 183-217.
14. K. Ke, Y. Wang, K. Zhang, Y. Luo, W. Yang, B.-H. Xie and M.-B. Yang, *J Appl Polym Sci*, 2012, **125**, E49-E57.
15. L. Jin, C. Bower and O. Zhou, *Appl Phys Lett*, 1998, **73**, 1197-1199.
16. B. S. Ince-Gunduz, R. Alpern, D. Amare, J. Crawford, B. Dolan, S. Jones, R. Kobylarz, M. Reveley and P. Cebe, *Polymer (Guildf)*, 2010, **51**, 1485-1493.
17. Y. Pei and X. C. Zeng, *Journal of Applied Physics*, 2011, **109**, -.
18. W. Mead, A. E. Zachariades, T. Shimada and R. S. Porter, *Macromolecules*, 1979, **12**, 473-478.
19. R. Gregorio, *J Appl Polym Sci*, 2006, **100**, 3272-3279.
20. L. Priya and J. Jog, *Journal of applied polymer science*, 2003, **89**, 2036-2040.

21. T. U. Patro, M. V. Mhalgi, D. Khakhar and A. Misra, *Polymer*, 2008, **49**, 3486-3499.
22. N. Levi, R. Czerw, S. Xing, P. Iyer and D. L. Carroll, *Nano Letters*, 2004, **4**, 1267-1271.
23. S. Yu, W. Zheng, W. Yu, Y. Zhang, Q. Jiang and Z. Zhao, *Macromolecules*, 2009, **42**, 8870-8874.
24. S. Manna and A. K. Nandi, *The Journal of Physical Chemistry C*, 2007, **111**, 14670-14680.
25. A. J. Lovinger, *Polymer*, 1980, **21**, 1317-1322.
26. B.-E. El Mohajir and N. Heymans, *Polymer*, 2001, **42**, 5661-5667.
27. K. Tashiro, ed., *Crystal structure and phase transition of PVDF and related copolymers*, New York: Marcel Dekker, 1995.
28. H. Su, A. Strachan and W. A. Goddard, III, *Physical Review B*, 2004, **70**, 064101.

Chapter 5 PVDF Aerogel and PVDF/CNTs Composite Aerogel for Oil/Water Separation and Fast Oil Absorption

Highly porous poly (vinylidene fluoride) (PVDF) aerogel with superhydrophobicity and superoleophilicity was successfully prepared by vapor induced phase inversion process. The surface properties studied by contact angle show that PVDF aerogel is superhydrophobic, with a water contact angle of 151° , and has almost instantaneous oil absorption. Contributed by the hierarchical micro-nano structure, both surfactant-free and surfactant-stabilized oil-in-water emulsion could be effectively separated by the fabricated PVDF aerogel simply under gravity, with good flux and high filtrate purity up to 99.99%. PVDF aerogel also exhibits moderate oil absorption capacity of 3~7g/g and high up-taking rate for various types of oil, suggesting that it is a promising material to be employed in various scenarios to absorb oils. Furthermore, PVDF aerogel is highly stable against concentrated alkaline solution owing to its superhydrophobicity. PVDF/CNTs composite aerogel has also been fabricated. With 0.1 wt. % CNTs, the compression strength and modulus can be largely improved, without impairing the surface properties.

5.1 Introduction

Membrane with special surface properties has drawn increasing attention in both industry and academia in recent years. Surface with water contact angle large than 150° is superhydrophobic.¹ In nature, many biomaterials have high to super hydrophobic surfaces, such as the lotus leaf, cabbage leaf and bird feathers.² The morphological structure is critical in achieving superhydrophobicity. It has been discovered that the superhydrophobicity of lotus leaf is contributed by the numberless micrometer sized papillae accompanying with even smaller protrusions.³ This kind of hierarchical structure is believed to be able to trap large amount of air minimizing the real contact area between the surface and water. On this account, superhydrophobic surface has been endowed with self-cleaning, anti-icing, anti-sticking and anti-contamination properties.⁴⁻⁷

Due to the outstanding performance in mechanical properties, heat and thermal resistance, as well as the inertness to most of organic or inorganic solvents, Polyvinylidene Fluoride (PVDF) based materials has been extensively used in membrane applications, such as top surface of raincoat, vehicles, outdoor conditioners, micro and ultrafiltration membranes.⁸⁻¹⁰ PVDF is a fluoropolymer with low surface energy, 25 dynes/cm. Meanwhile, PVDF is intrinsically polar material because of partial fluorination, resulting in a lower contact angle (CA) around 70° compared with that of some polyolefin.¹¹ In spite of this, PVDF superhydrophobic surface has been obtained by diversified strategies, such as plasma treatment¹², electrospinning¹³⁻¹⁶, surface coating¹⁷,¹⁸, hybridization¹⁹⁻²² and chemical deposition^{23, 24}. Recently, superhydrophobic PVDF and PVDF copolymer porous material were successfully prepared by introducing hydrophobic graphene inside via a phase inversion method.^{25, 26} Wenbin et al. fabricated both superhydrophobic and superoleophilic PVDF membranes by adding ammonia in the process of phase inversion facilitating the formation of PVDF clusters with special structures.

In this work, we prepared PVDF aerogel through vapor induced phase inversion. The obtained aerogel is light in weight and possesses very porous structure. It is both superhydrophobic and superoleophilic that make it selectively absorb oil from water-in-oil mixtures, with or without surfactant stabilization. The simple manufacture process

makes the method promising for the large scale production of this highly porous material which might be used for purifying oils from water in various circumstances.

5.2 Experiments

5.2.1 Sample Preparation

To make pure PVDF aerogel, 10 wt. % PVDF in DMSO was firstly prepared by magnetic stirring. The transparent solution was then transferred into glass Petri dish with diameter 60mm and height 15mm. Then the glass dish containing PVDF solution was put into a sealed container with 500 ml DI water inside. Three days later, after the water vapor induced phase inversion completed, the obtained PVDF/DMSO gel was repeatedly washed by water. After that, the PVDF hydrogel was dried by freeze drying. Similarly, to fabricate PVDF/CNTs composite aerogel, 20 wt. % PVDF/DMSO and CNTs/DMSO with calculated CNTs amount are prepared separately before mixing them together. Magnetic stirring and ultrasonication are employed to increase the uniformity of PVDF/CNTs/DMSO solution. After that, followed by phase inversion procedure in sealed container and freeze drying, PVDF/CNTs composite aerogel is obtained. The oil/water mixtures are prepared both with and without surfactant using various kinds of oils. The ingredient of surfactant free mixture and surfactant stabilized emulsions are listed in table 5.1 and 5.2 following. The surfactant free oil/water mixtures are obtained by 60 mins sonication in bath sonicator while surfactant stabilized oil/water mixtures are prepared by 3 hours vigorous magnetic stirring.

Table 5.1 Compositions of water-in-oil mixture with surfactant.

Solvent	Vol.	Vol. (Water)	Span 80
Hexane	50ml	0.25ml	0.125g
Dichloromethane	50ml	0.25ml	0.125g
Toluene	50ml	0.25ml	0.125g
Chlorobenzene	50ml	0.25ml	0.125g
Cyclohexane	50ml	0.25ml	0.125g
Gasoline	50ml	0.25ml	0.125g
Diesel	50ml	0.25ml	0.125g

Table 5.2 Compositions of water-in-oil mixture without surfactant.

Solvent	Vol.	Vol. (Water)	Span 80
Hexane	180ml	20ml	0
Dichloromethane	180ml	20ml	0
Toluene	180ml	20ml	0
Chlorobenzene	180ml	20ml	0
Cyclohexane	180ml	20ml	0
Gasoline	180ml	20ml	0
Diesel	180ml	20ml	0

5.2.2 Characterizations

The morphology of prepared samples was studied by field emission scanning electron microscope (FESEM, JEOL JSM-7600F). The SEM samples were coated with platinum before observation. The contact angle of water and absorbing process of oil are studied by Contact Angle Data Physics OCA15Pro equipped with camera and video. The water content in oils is measured by CA-200 moisturemeter. The compression strength and modulus are measured by Mech Tester Instron 5567. Samples under test are in cylinder

shape with diameter 42 mm and height 3.6~3.8 mm. The strain rate is set to be 5 mm/min and at least five samples are tested for each data point. The water droplet in oil/water mixture without surfactant is studied by Olympus BX51 and the droplet size in surfactant stabilized mixtures is determined by Malvern Nanosizer. N₂ adsorption/desorption isotherms were measured by micromeritics ASAP 2020.

5.3 Results and Discussion

The three main steps of our fabrication method of PVDF aerogel are illustrated in Figure 1 (a). In the first phase inversion step, both solvents DMSO and non-solvent H₂O would evaporate inside the water containing sealed container. With the increase of concentration of water than that of DMSO, PVDF solution gradually became gel. In a traditional sol-gel process used for fabricating inorganic aerogel, the molecular precursors are firstly converted into cross-linked structure, followed by drying to create a solid porous structure. Similarly, polymeric aerogel can be obtained either by polymerizing monomers into cross-linked network, or transforming the liquid to solid phase via physical phase inversion.^{27, 28} The latter method is adopted in this work because of its simplicity and tailorability of morphology. After PVDF/DMSO gel formed, subsequent solvent exchange by immersing inside water further replaced the DMSO with H₂O. The final product i.e. PVDF aerogel was obtained after freeze drying. The sample appearances during each step are shown in Figure 1 (b). It is seen that the transparent PVDF/DMSO expectedly became opaque and white in color after DMSO was exchanged with non-solvent, i.e. water.

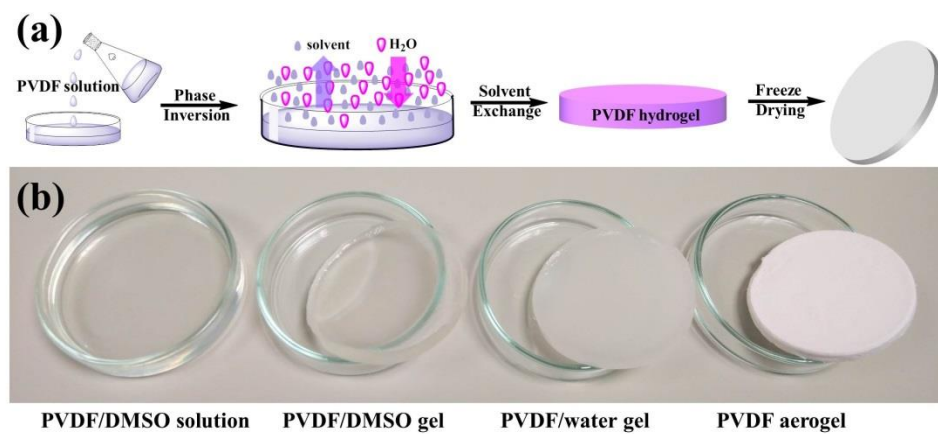


Figure 5.1 (a) Schematic illustration of the formation of PVDF aerogel (b) Digital photo of different steps in fabricating PVDF aerogel.

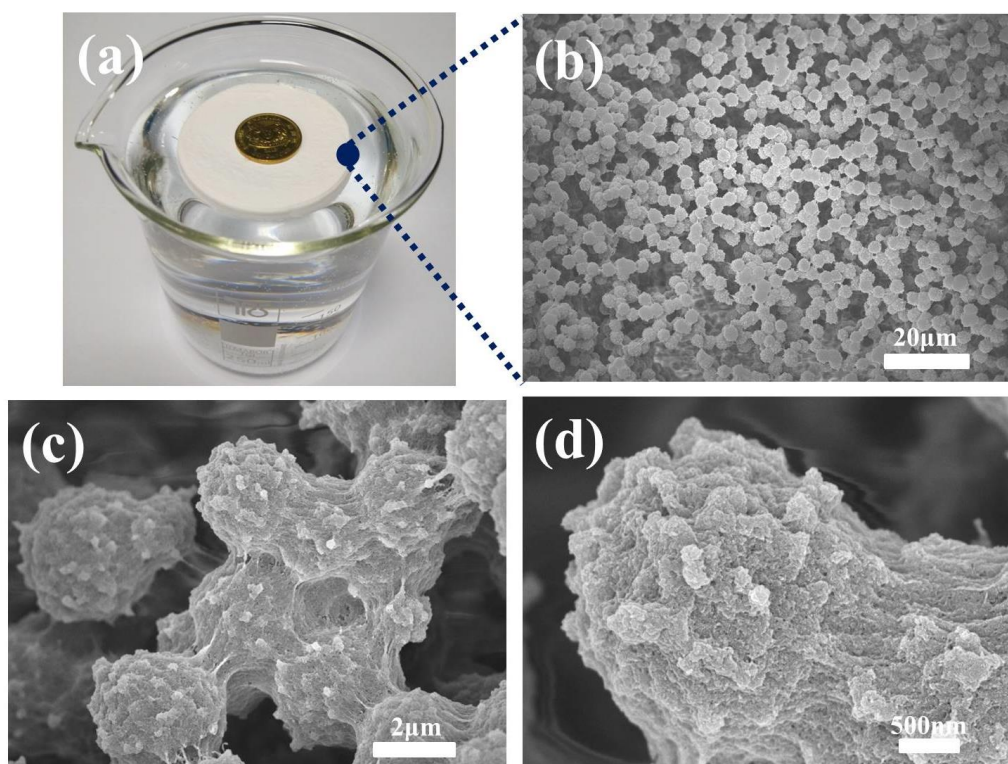


Figure 5.2 Photograph of PVDF aerogel on water with five cent Singaporean coin (diameter 16.75mm, thickness 1.22mm, mass 1.70g) on top (a) and FESEM of PVDF aerogel with different magnifications.

PVDF aerogel has very low density around 0.2 g/cm^3 . Figure 5.2 (a) shows photograph of 1 g PVDF aerogel floating on water with 1.7 g coin on topside. The low density is due to high porous structure. FESEM show that the PVDF aerogel are composed of spherical particulates with size of several micrometers that are partially connected with each other, leaving interconnected channels (or pores) from several micrometers to dozens of micrometers. The pore size is critical in separating surfactant stabilized oil/water emulsion which features with small droplets. It is believed many superhydrophobic/superoleophilic materials are incapable of removing oils from water in emulsified solution due to the oversized pores.²⁹ Besides, the surface of those spherical structures is not smooth but covered by abundant nano protrusions pointing outwards, making it a coral-like structure. The sphere and nano protrusion are around $3 \mu\text{m}$ and $100\sim 200 \text{ nm}$, respectively. This kind of hierarchical structure is vital for the high hydrophobicity and superoleophilicity via enhancement of surface roughness.³⁰

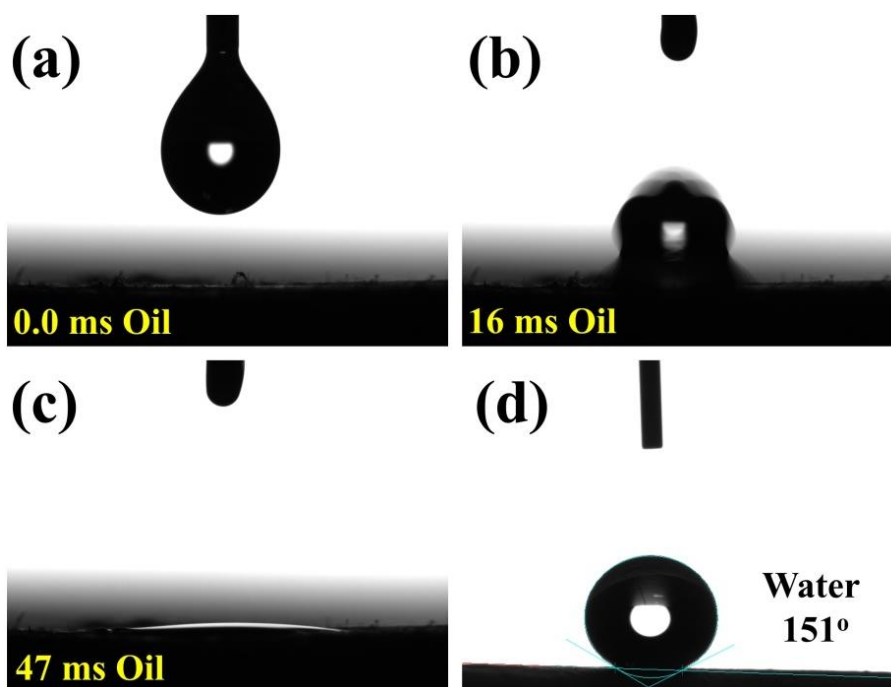


Figure 5.3 Absorbing process of oil (a, 0.0ms; b, 16ms; c, 47ms) and contact angle of water (d). The volume of oil and water are 6 and $10 \mu\text{l}$, respectively. The photos are captured by the camera attached with contact angle measurement system.

PVDF aerogel responds drastically different toward oil (toluene was used as oil) and water. As shown in Figure 5.3, as soon as oil droplet touched the surface, it penetrated the aerogel quickly. Within 47 ms, most of the oil was absorbed, demonstrating the superoleophilicity of the aerogel. By contrast, the aerogel has large water contact angle of 151° , which is much higher than the contact angle on bulk PVDF film with smooth surface prepared by hot press ($\sim 70^\circ$). The water repellency of the aerogel was also evaluated based on water sliding angle, which was determined to be as low as 3° , indicating high water repellency as observed for lotus leaf and butterfly wings.³¹ It is understood that the surface properties of materials are governed critically by both surface free energy and roughness. The surface free energy is determined by the chemical structure of materials; while on the other hand, original surface wetting behavior can be enhanced by a rougher surface, i.e., hydrophobic/hydrophilic material possesses even higher degree of hydrophobicity/hydrophilicity with increased roughness. With a rough surface, the real solid-liquid interface is much larger than the apparent value.³² The remarkable oleophilicity and hydrophobicity of prepared PVDF aerogel are attributed to the hierarchical microstructure which traps air pockets, and a larger solid-liquid interface when water droplet deposits on the aerogel. Recent studies indicated that the boundary of water contact angle dividing hydrophobicity and hydrophilicity is 65° , rather than 90° .³³ ³⁴ Many materials previously regarded as hydrophilic could be made superhydrophobic by increasing the surface roughness.³⁵⁻³⁷

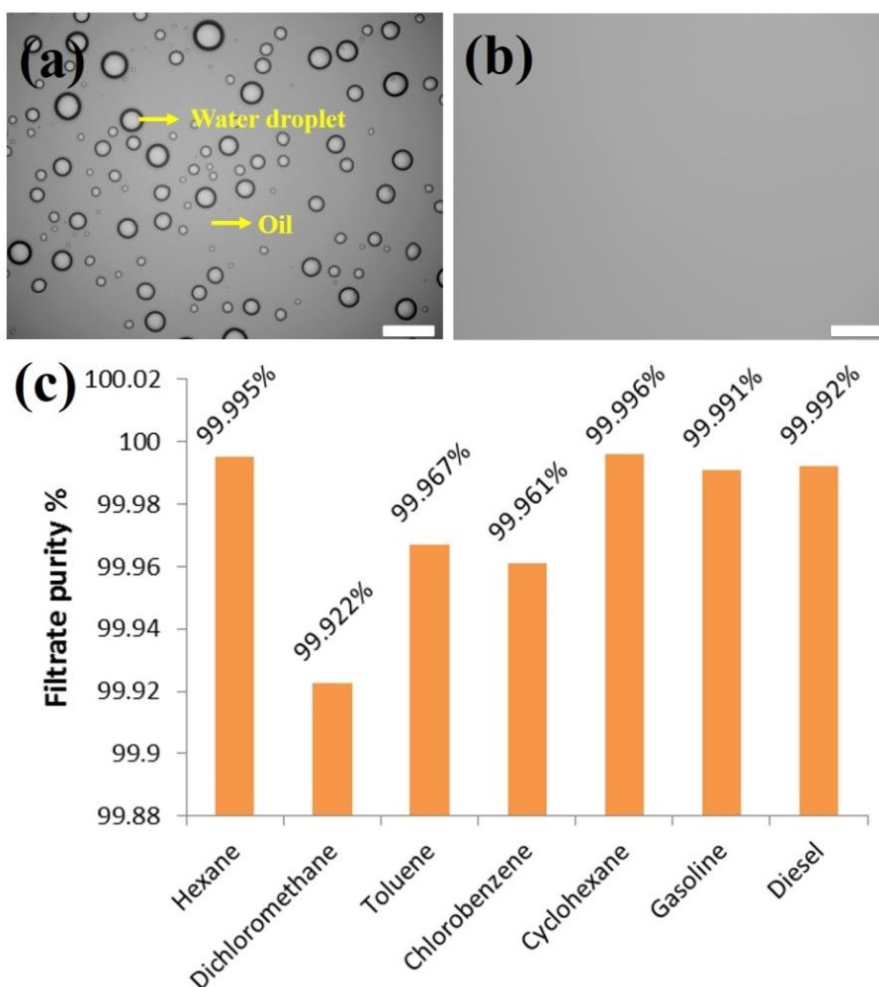


Figure 5.4 Optical images of oil/water mixture without surfactant before (a) and after (b) filtration and (c) filtrate purity of oil/water mixtures with various oils. The scale bar is 100μm.

To examine the separation capability of PVDF aerogel toward oil/water mixtures, a filtration system is set up with PVDF aerogel serving as the filter medium. The prepared emulsions were filtered through the PVDF aerogel and the filtrates were collected for the purity tests. Before the filtration, the water droplets in oil/water mixture were examined under optical microscope. Figure 5.4 (a) shows the typical appearance of water droplets in toluene. It was observed that water droplets with size between 10 ~ 50 μm were well distributed in continuous oil phase. The optical microscopic image of the filtrate is shown in Figure 5.4 (b), and there is no observable droplet, indicating successful removal of the water from toluene. The purity of filtrate, as determined by moisturemeter, could be as high as 99.97 %; which is comparable to, if not higher than the liquid chromatographic

grade. Considering the unavoidable absorption of atmospheric moisture during experiments, the actual filtrate purity could even be higher than measured value. Several other oil/water emulsions with hexane, dichloromethane, chlorobenzene, cyclohexane, gasoline and diesel as the continuous phase had also been tested, and the respective filtrate purities are listed in Figure 5.4(c). Despite the difference in filtrate purity that was dependent on the type of oil, all filtrates possessed oil phase of more than 99.9 % high in purity. For certain oils, including hexane, cyclohexane, gasoline and diesel, the filtrates possess purity that is even higher than 99.99 %.

The difference in filtrate purities is believed to be closely related to the polarity of oils, i.e. oil with higher polarity has lower separation efficiency. The polarity of oils used in the study is as follows: hexane, cyclohexane < toluene < chlorobenzene < dichloromethane³⁸; while the sequence of filtrate purity is hexane, cyclohexane > toluene > chlorobenzene > dichloromethane. It is expected that oil with higher polarity has stronger interaction with water, making the separation more difficult. Both gasoline and diesel are intrinsically mixtures of mostly short chain hydrocarbon alkyl; therefore they have similar polarity to hexane. In our experiments, filtrate purity using gasoline and diesel as the oil phase could be achieved as high as that of hexane. The flux of surfactant-free emulsion separation is calculated to be $\sim 1240 \text{ L/hm}^2$. Similar fluxes were also witnessed for other oil/water emulsions. It was noted that the separation was driven only by gravity. There is no doubt that by increasing the oil/water emulsion volume (height) in the funnel (larger static pressure) or simply exerting external force (e.g., vacuum pump) could further increase the separation flux. The flux is also related to the thickness of the filter medium. It is envisioned that with reduced aerogel thickness, the separation efficiency can also be enhanced.

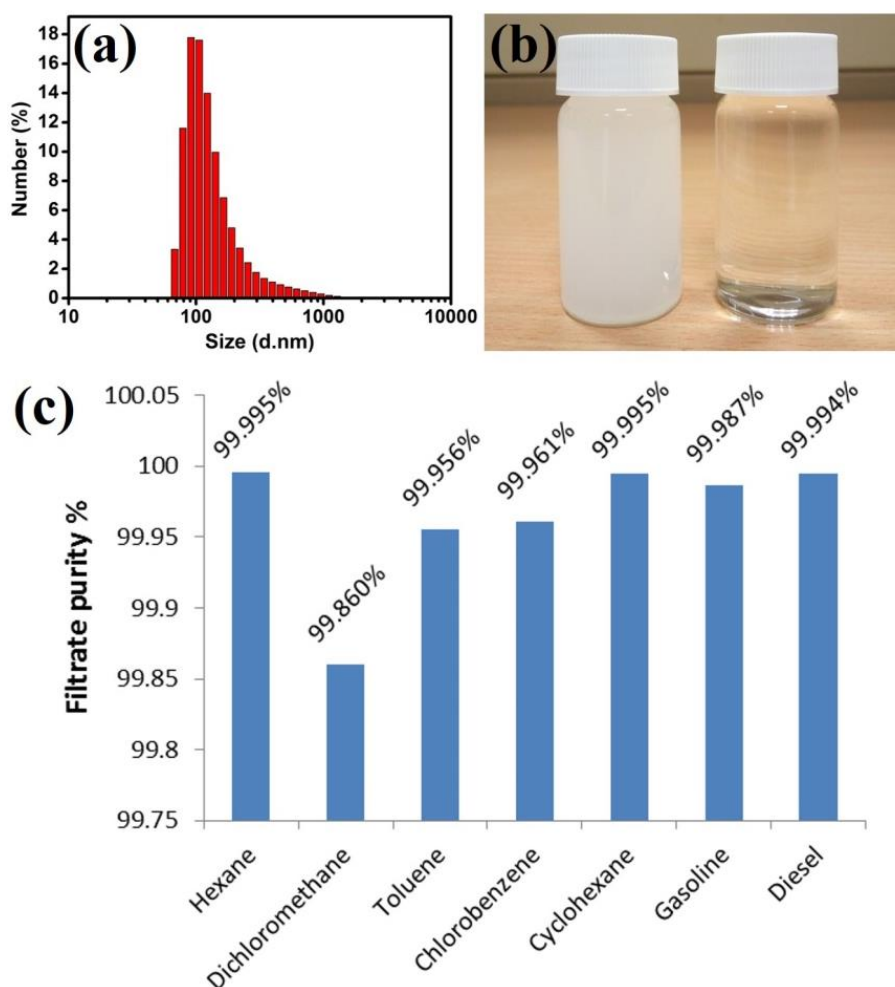


Figure 5.5 Size distribution of surfactant stabilized oil/water mixture before (a) and after (b) filtration and (c) filtrate purity of oil/water mixtures with various oils.

Industrial waste effluent often contains various types of surfactants or dispersants. To investigate the effectiveness of PVDF aerogel in separating surfactant-stabilized emulsions, further tests involving surfactant in different oil/water mixtures were conducted. Firstly, the number and size of water droplets are investigated before and after the filtration. Figure 5.5 (a) shows the size distribution of water droplet in cyclohexane before the separation test, as determined by dynamic light scattering (DLS). It is seen that the size ranges from ~ 60 nm to $1\text{ }\mu\text{m}$, with the majority centered at approximately 100 nm. The emulsion was stable for 4 days without sedimentation or phase separation. After filtration of the surfactant-stabilized emulsion through the PVDF aerogel, no size data was measurable by DLS due to the lacking of water droplet in oil, indicating complete

removal of water from the emulsion. From the digital photos of the emulsions before and after filtration, as shown in Figure 5.5 (b), the milky solution became totally transparent as contributed by the complete removal of water. The filtrate purity of cyclohexane, as well as those of other oils is listed in Figure 5.5 (c). There was virtually no decrease in the filtrate purity after the introduction of surfactant with the values ranging from 99.86% of dichloromethane to all others that exceeded 99.9%. Nevertheless, it was observed that the separation flux of surfactant-stabilized emulsion was lower than those without surfactant. On top of the subtle change in separation performance among different batches of prepared aerogel, the flux for surfactant stabilized water-in-cyclohexene is calculated to be around 220 L/hm². Comparable fluxes are obtained for the cases of other oils. This range of flux values was much lower than those of the separation of surfactant-free emulsion, partially due to increased viscosity after introduction of surfactant. Moreover, it is expected that higher energy is needed to ‘break’ the surfactant/oil interfaces, and this results in further decrease of the separation rate and flux. However, the flux is higher than typical values that were previously reported. Li et al.³⁹ prepared cellulose hollow fiber ultrafiltration membrane for oil/water separation, achieving separation flux less than 10 L/hm² under pressure of 0.1 MPa. Chakrabarty et al.⁴⁰ fabricated a variety of polysulfone membranes with separation flux less than 120 L/hm² under pressure of 103.4kPa. The much higher flux obtained with PVDF aerogel is believed to be ascribed to the superoleophilicity and high porosity.

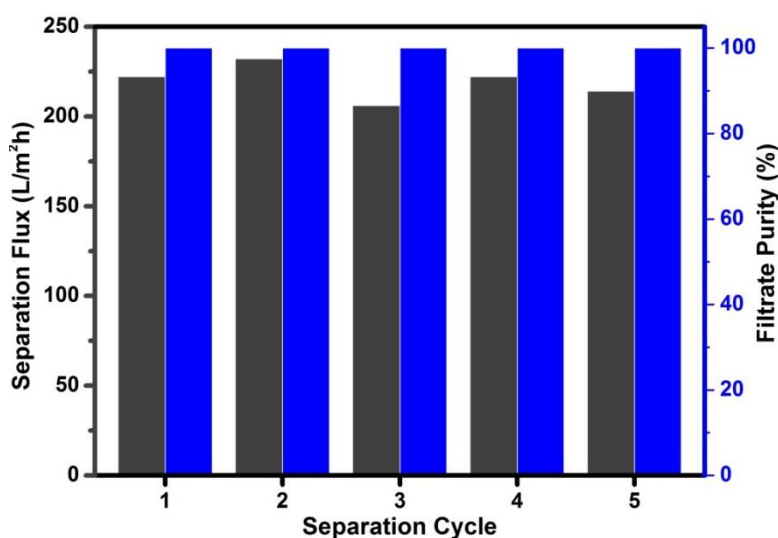


Figure 5.6 Separation flux and efficiency at different separation cycles.

To examine the reusability of PVDF aerogel in separating oil and water, the same PVDF aerogel was repeatedly used to separate surfactant-stabilized emulsion for 5 filtration cycles; using cyclohexene as the continuous oil phase. In each separation test, 100 ml emulsion was filtered through the aerogel; and the aerogel was vacuum dried before it was used for next filtration cycle. The separation flux and filtrate purity were measured for each cycle and the results are shown in Figure 5.6. The separation fluxes for 5 filtration cycles are calculated to be 222, 232, 206, 222 and 214 L/hm², respectively. Within experimental error, it can be regarded that there was no obvious decrease in the flux. On the other hand, high separation efficiency was observed for all 5 filtration cycles, with all purities of filtrated cyclohexane surpassing 99.99%. The results indicate that the aerogel can be used repeatedly without compromising its performance in oil/water separation.

The sharp contrast of surface affinity between PVDF aerogel to water and oil, along with its unique 3D structure, suggest that the aerogel possesses high potential to be used for oil absorption. To evaluate the absorption performance, the up-taking capability of various oils by the aerogel was tested. The aerogel was immersed in oils for 1 h for complete oil up-taking. The absorption capacities of various oils by the aerogel were represented by the ratio of weight of aerogel after and before the up-taking. The calculated absorption capacities are compiled in table 5.3, that it can be seen that PVDF aerogel possesses moderate up-taking ability towards various oils with capacity of about 3 to 7 g/g.

Table 5.3 Absorption capacity of PVDF aerogel for various oils.

Oil Type	Absorption Capacity (g/g)
Hexane	3.10
Toluene	4.17
Gasoline	3.54
Diesel	4.05
Dichloromethane	6.78
Chlorobenzene	5.58
Cyclohexane	4.01

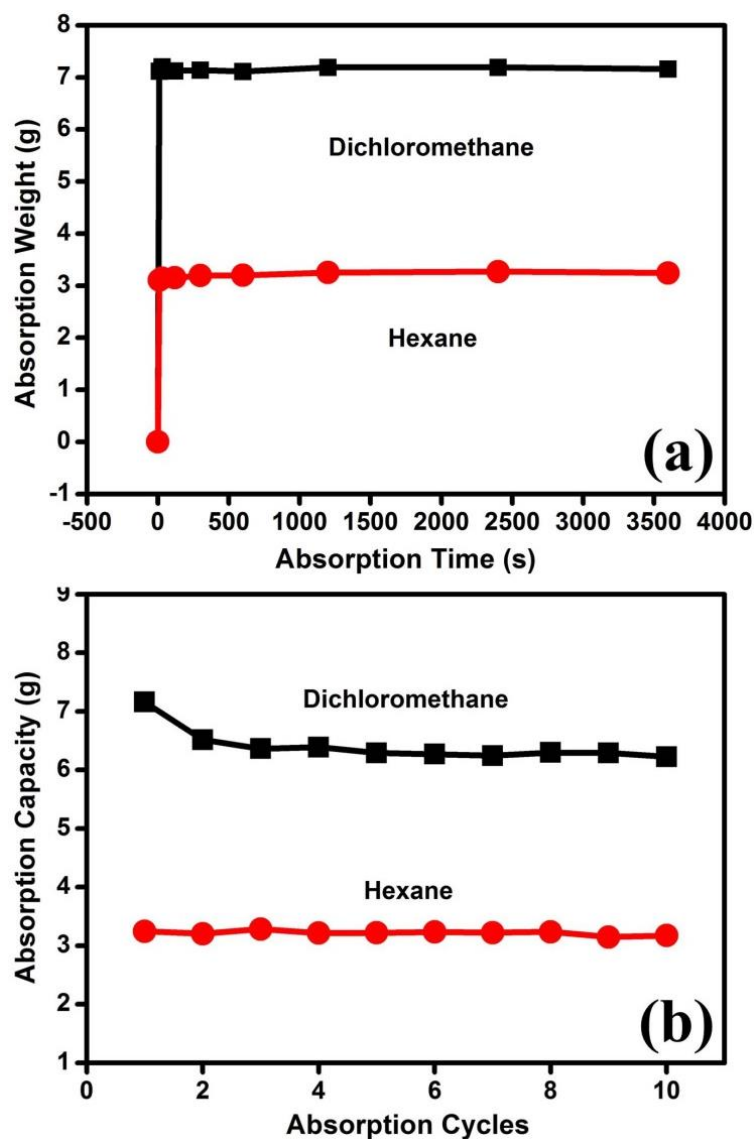


Figure 5.7 Change of absorption weight as function of time of PVDF aerogel in dichloromethane and hexane (a) and absorption capacity as function of number of cycles in dichloromethane and hexane (b).

Apart from oil absorption capacity, other factors, such as oil absorption kinetics, reusability and the ease of oil recovery, are important considerations to assess the suitability of a material for oil cleanup. Dichloromethane and hexane were used as the oil phases to examine the absorption rate and reusability. PVDF aerogel was weighed after immersion in oils for durations of 10s, 30s, 2 min, 5 min, 10 min, 20 min, 40 min and 60 min. The absorption weights as a function of time are showed in Figure 5.7 (a). Minimal change is observed for the weight absorbed after 10 s and 60 mins, indicating a fast

absorption rate towards oils. Within 10 s, the aerogel absorbs up to 99.4 % of its capacity for dichloromethane and 102.3% for hexane, respectively. The fast absorption rate was ascribed to the superoleophilicity towards oils and the large surface area of PVDF aerogel. The reusability was also tested by repeated immersion-drying cycles of aerogel in oil; the oil uptake capacities after different absorption cycles are shown in Figure 5.7 (b). It can be seen that a decrease in absorption capacity for chloromethane was observed during the second uptake, which is believed to be due to solvation effect that induced shrinkage of the aerogel. The subsequent uptakes of dichloromethane by aerogel stabilized and the absorption capacity after 10 cycles was about 91 % of its first-cycle capacity. As for the case of hexane, the absorption capacity remained constant within 10 cycles, indicating the good structural stability of PVDF aerogel toward hexane. Looking at conventional natural absorbents used for cleanup of oil spillage, such as cellulose, wood waste, zeolite and cotton fibers, they often suffer from slow absorption rate, co-absorption of water and incurred deactivation of absorbents.^{41, 42} As for the PVDF aerogel, with its high absorption rate, good reusability and high selectivity towards oils, it exhibits great potential to be used for oil spillage remediation. Another advantage of PVDF aerogel is that it can be easily cleaned and regenerated by rinsing with common organic solvents. In fact, often in the real application involving oil/water separation, high amount/weight of solution and harsh environmental conditions would demand good mechanical properties of separation materials. The mechanical properties of porous aerogel is known to be very different from that of bulk materials. In this regard, we studied the effect of polymer concentrations on the mechanical properties of the PVDF aerogel by compression test. The typical compressive stress-strain curves of PVDF aerogel of different PVDF concentrations are plotted in Figure 5.8 (a). Generally speaking, the stress-strain curves can be divided into two regions, with boundary at strain of around 30%. Before strain reaches 30%, the trend of the curves is not obvious due to the existence of tilt edge formed during the sol-gel process. After strain reached 30%, aerogels fabricated from higher polymer loading exhibited clearly higher compressive strength and modulus. Taking the compressive strength at 45% strain for example, the values increased from 139 kPa by 66.2% to 231 kPa, when PVDF concentration increases from 8 to 20 wt. %;

while the elastic modulus increased from 665 to 1870 kPa, by an increment of 181 %. Detailed values are compiled in table 5.4.

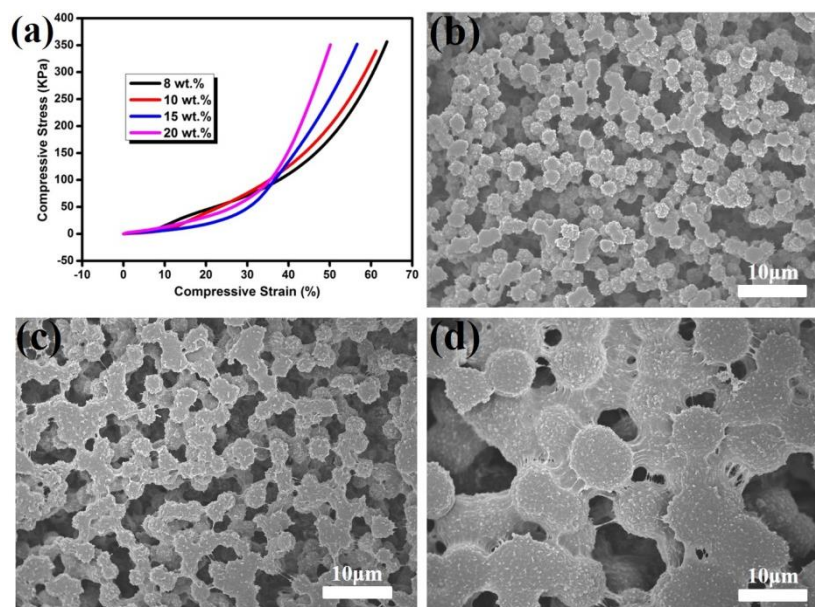


Figure 5.8 Stress-strain curves of aerogels prepared from PVDF solutions with concentration 8, 10, 15 and 20 wt. % (a) and FESEM images of aerogel prepared from polymer loading of 8 wt. % (b), 15 wt.% (c) and 20 wt.% (d).

The mechanical properties of PVDF aerogel are in turn critically determined by its microstructure. Using FESEM, the morphologies of aerogels prepared from different concentration of PVDF were observed, from 8 wt. % to 20 wt. % (corresponding to image b to d in Figure 5.8). It was observed that the micro-sized spherical particulate became larger with the increase of polymer concentration. For example, the spherical particulate size of 8 wt. % aerogel is around only 2 μm , while that of aerogel from 20 wt. % is 4 times larger. Furthermore, the spherical particulates are more packed with higher PVDF loading. It could be seen that the spherical particulates of aerogels prepared from higher PVDF loading have more contacting interfaces with neighboring ones. The above observed morphology is believed to have contributed to the superior mechanical properties. Nevertheless, despite the variations in PVDF structure, owing to the existence of air within porous structures, aerogels prepared from all polymer concentrations exhibited similar hydrophobicity and oleophilicity.

Table 5.4 Compressive strength and modulus of each aerogel prepared from different PVDF concentrations. To enable statistical reliability, 5 samples for each concentration were tested.

Concentration	Compressive Strength	Compressive Modulus
8 wt. %	139(6) ^a	665 ^b (32)
10 wt. %	157(2)	724(23)
15 wt. %	217(20)	1296(75)
20 wt. %	231(7)	1870(27)

^aThe value in the bracket is mean deviation, calculated according to the formula $x = \frac{\sum_{i=1}^n |x_i - \bar{x}|}{n}$, where \bar{x} is the mean value and n is the sample number.

^bThe modulus E at strain of 45% is estimated by the formula $E(45\%) = \frac{\sigma(46\%) - \sigma(44\%)}{\varepsilon(46\%) - \varepsilon(44\%)}$, where σ and ε are stress and strain, respectively.

The chemical resistance of PVDF aerogel to alkali was also investigated. It is well known that PVDF is highly thermally stable, anti-oxidative, anti-radiative and anti-corrosive to most of the harsh chemicals, however, PVDF is vulnerable to the attack of concentrated alkali solution such as sodium hydroxide.⁴³ Different from perfluoropolymer, PVDF has unsubstituted β -carbon in the molecular chain, which enables the E2 elimination reaction in the presence of alkali solution, involving elimination of HF and leaving polyene chain. Exposure to concentrated sodium hydroxide also creates hydroxide and carbonyl groups, seriously impairing the mechanical and other physical properties of PVDF.⁴⁴ To evaluate alkali-resistance properties of PVDF aerogel, PVDF aerogel (10 wt.%) was immersed and kept in saturated sodium hydroxide solution at room temperature, and it was found to be intact after one year time. The excellent resistance to alkaline solution is believed to be made possible by the superhydrophobicity of the aerogel surface, which effectively limits any interaction between PVDF and sodium hydroxide molecules. This encouraging anti-corrosion property of PVDF aerogel gives promise for it to be used in more complex and harsh operation conditions. It needs to be highlighted here that PVDF aerogel is also a non-crosslinked thermoplastic polymer that can be easily recycled, reused and reformed into any shape, thus greatly widening its applications.

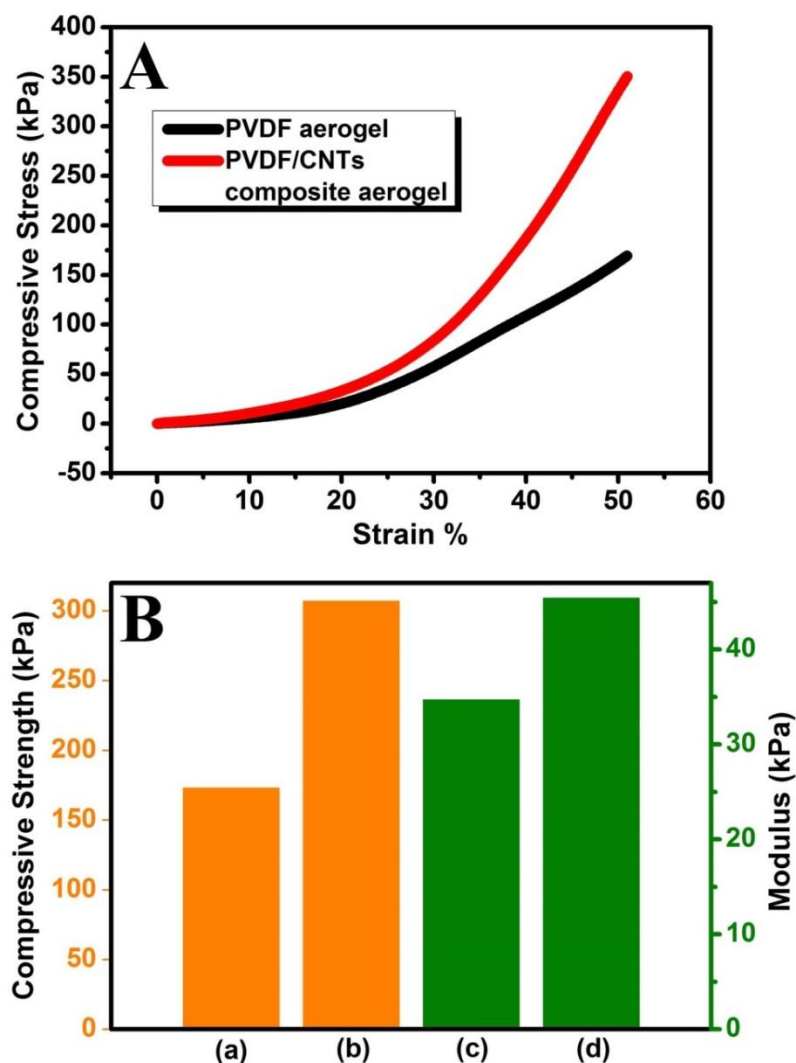


Figure 5.9 Stress-strain curve (A) and Young's modulus as well as compression strengths (B) of PVDF aerogel and of PVDF/CNTs composite aerogel. (a) Compression strength of PVDF aerogel, 173 (66) MPa (b) compression strength of PVDF/CNTs composite aerogel, 307 (41) MPa (c) Young's modulus of PVDF aerogel, 34.7 (18.5) MPa (d) Young's modulus of PVDF/CNTs composite aerogel, 45.4 (23.8) MPa; the value in the bracket is standard deviation.

The mechanical performances of PVDF aerogel and PVDF/CNTs composite aerogel were examined by compression testing. Stress-strain curve, compression strength and Young's modulus are shown in Figure 5.9. It can be seen after introduction of 0.1 wt. % CNTs, the mechanical performance of PVDF aerogel are markedly enhanced. The compression strength and Young's modulus increase by 31 and 77 %, respectively. The mechanical data reveal that the good dispersion and potential as strong fillers of CNTs have been well realized.

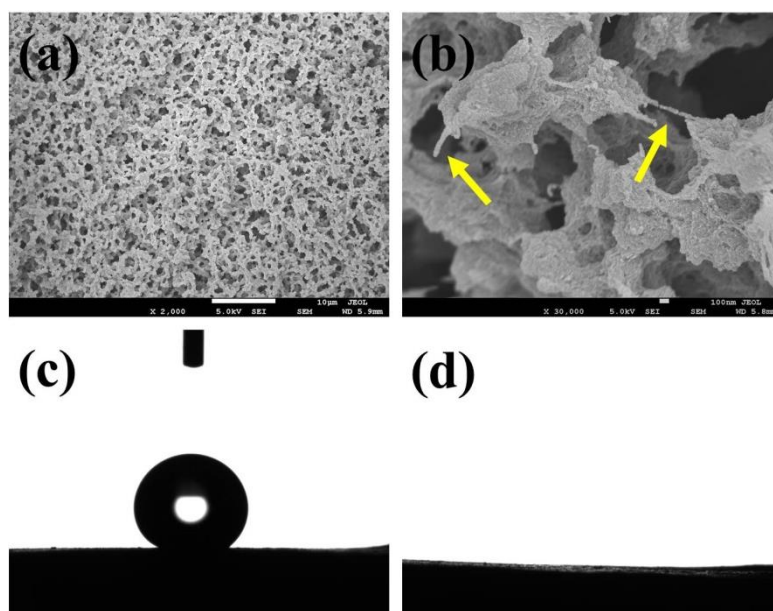


Figure 5.10 FESEM (a, b), water (c) and oil (d) contact angle of PVDF/CNTs composite aerogel.

PVDF/CNTs composite aerogel displays a very different morphology compared with PVDF aerogel, shown in Figure 5.10. Partially connected micro particles that constitute PVDF aerogel cannot be seen. Instead, the composite aerogel is composed of more irregular shaped foam-like structures which also connected with each other. It is noted that there are more interfaces between that the particulates; which is believed to contribute to the enhanced mechanical properties of composite aerogel. Besides that fact that spherical structures disappear after the introduction of CNTs, the particulates surfaces are far from smooth and covered with irregular nano-size protrusions, see the higher magnification SEM in Figure 5.10 (b). Furthermore, as indicated by the arrow, CNTs can be clearly observed in the composite aerogel. It is seen CNTs either protrude out from particulates or connect two neighboring particulates. The well dispersed CNTs can readily absorb energy under compression, leading to significantly enhanced compression strength and modulus.

Figure 5.10 (c) shows that the water contact angle of composites is 142° , very close to that of PVDF aerogel. Within the experimental error, it can be regarded they are the same. Similar to PVDF aerogel, the composite aerogel absorb the oil very quickly; no contact angle could be obtained, shown in Figure 5.10 (d). This suggests the introduction of CNTs does not impair the surface properties of aerogel.

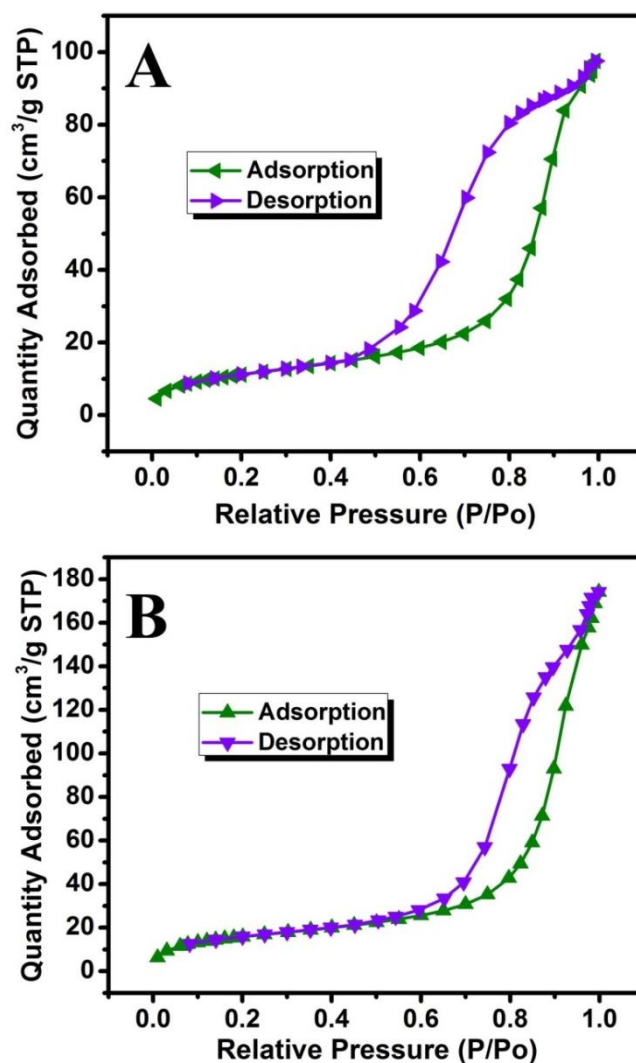


Figure 5.11 Nitrogen adsorption and desorption isotherms of (A) PVDF aerogel and (B) PVDF/CNTs composite aerogel.

Nitrogen adsorption and desorption isotherms of PVDF aerogel and PVDF/CNTs composite aerogel are shown in Figure 5.11. Both PVDF aerogel and the composite aerogel belong to Type IUPAC IV isotherm characteristic. The BET surface area and average pore size radius of PVDF aerogel are $40.3 \text{ m}^2/\text{g}$ and 15.0 nm while that of composite aerogel are $56.5 \text{ m}^2/\text{g}$ and 19.1 nm . The increments are respectively 40.2 and 27.3% . The large variation in surface area and pore size is understandable considering the large morphology changes after the introduction of CNTs. It is reported that the surface aerogel slightly decrease after CNTs are filled in the cellulose aerogel.⁴⁵ For example, with 3 and $10 \text{ wt. } \%$ CNTs loading, the surface area of PVDF aerogel decreases

from 163.2 m²/g to 159.1 and 140.4 m²/g. The different results come from the different effects of CNTs addition on the final morphology of cellulose and PVDF aerogel. Different from our prepared PVDF/CNTs aerogel, the cellulose/CNTs composite aerogel has very similar morphology to that of pure cellulose aerogel. The large change in the morphology between PVDF aerogel and composite aerogel indicates that the CNTs play an important role in the sol-gel process of PVDF/CNTs aerogel. One plausible explanation is that CNTs accelerate the crystallization behavior of PVDF. Similar results were reported in graphene oxide (GO) filled porous PVDF membrane. Zhao et al.⁴⁶ prepared PVDF/GO membrane with increased porosity and pore size than the pure PVDF membrane and they believed that the hydrophilic GO can facilitate the diffusion rate between solvent and non-solvent which is beneficial for the new morphology. Zhang et al.⁴⁷ fabricated PVDF membrane filled with oxidized CNTs and GO and found that significant morphology change compared with that of neat PVDF membrane, which was also claimed to be due to the strong hydrophilicity of oxidized CNTs and GO. However, in this study, the CNTs used are actually hydrophobic, which can hardly accelerate the solvent/non-solvent exchange process. Instead, we believe that the existence of CNTs facilitates the crystallization of PVDF in the sol-gel process, benefitting the formation of larger pore size and leading to the resulting morphology.

The porosity P of PVDF aerogel and composite aerogel can be calculated according to the following equation:

$$P = \frac{V - \frac{W}{\rho}}{V} \quad (5.1)$$

Where V , W and ρ are volume of aerogel, weight of aerogel and density of bulk PVDF or PVDF/CNTs.

Considering the low concentration of CNTs (0.1 wt. %), the density of bulk PVDF and PVDF/CNTs can be regarded the same. Furthermore, there is no obvious volume change in the PVDF aerogel and composite aerogel. Therefore, in spite of the large difference in surface area, PVDF aerogel and composite aerogel possess very similar porosity.

Although it is expected that more CNTs loading will further enhance the mechanical performance, our study on PVDF/CNTs composite aerogel with 0.2 wt. % and above show rather tortile shape instead of regular cylinder, making mechanical testing

impossible to be carried out. This might be due to higher CNT loading that leads to aggregation during the sol-gel process, further resulting in considerable torque during freeze drying because of different densities in various sections. It is expected that the section with higher density undergoes less shrinkage while lower density area has more shrinkage after drying.

5.4 Summary

A facile vapor induced phase inversion method was used to fabricate PVDF aerogel with unique hierarchical micro-nano structure. The superoleophilicity and superhydrophobicity were achieved without using any additives. This highly porous and light-weight PVDF aerogel is able to separate both surfactant-free and surfactant-stabilized water-in-oil emulsion with high filtrate purity and separation flux. Emulsified water droplets with size as small as 60 nm can be effectively removed from continuous oil phase. Owing to its 3D structure, PVDF aerogel also exhibits promising absorption capacity towards various oil and almost instantaneous up-taking ability. Good reusability of aerogel for both oil/water separation and absorption of oil was demonstrated. The introduction of low loading content of CNTs can effectively enhance the mechanical performance compared with that of PVDF aerogel, without suppressing the surface properties. With the combinations of these good properties, it is envisioned that thermoplastic PVDF aerogel could find potential applications in both separation and absorption of oil under various scenarios.

References

1. X.-M. Li, D. Reinhoudt and M. Crego-Calama, *Chemical Society Reviews*, 2007, **36**, 1350-1368.
2. J. Fresnais, J. Chapel and F. Poncin-Epaillard, *Surface and Coatings Technology*, 2006, **200**, 5296-5305.
3. A. Pozzato, S. D. Zilio, G. Fois, D. Vendramin, G. Mistura, M. Belotti, Y. Chen and M. Natali, *Microelectronic Engineering*, 2006, **83**, 884-888.
4. N. A. Patankar, *Langmuir*, 2004, **20**, 8209-8213.
5. W. Ming, D. Wu, R. van Benthem and G. De With, *Nano letters*, 2005, **5**, 2298-2301.
6. I. A. Larmour, S. E. Bell and G. C. Saunders, *Angewandte Chemie*, 2007, **119**, 1740-1742.
7. M. Li, J. Xu and Q. Lu, *J. Mater. Chem.*, 2007, **17**, 4772-4776.
8. N. Yoshida, M. Takeuchi, T. Okura, H. Monma, M. Wakamura, H. Ohsaki and T. Watanabe, *Thin Solid Films*, 2006, **502**, 108-111.
9. Y. Li, W. Cai, G. Duan, B. Cao, F. Sun and F. Lu, *J. Colloid Interface Sci.*, 2005, **287**, 634-639.
10. F. Liu, N. A. Hashim, Y. Liu, M. Abed and K. Li, *J. Membr. Sci.*, 2011, **375**, 1-27.
11. M. Peng, H. B. Li, L. J. Wu, Q. Zheng, Y. Chen and W. F. Gu, *J. Appl. Polym. Sci.*, 2005, **98**, 1358-1363.
12. C. Yang, X. M. Li, J. Gilron, D. F. Kong, Y. Yin, Y. Oren, C. Linder and T. He, *J. Membr. Sci.*, 2014, **456**, 155-161.
13. S. H. Park, S. M. Lee, H. S. Lim, J. T. Han, D. R. Lee, H. S. Shin, Y. J. Jeong, J. Kim and J. H. Cho, *ACS Appl. Mater. Interfaces*, 2010, **2**, 658-662.
14. Y. B. Chen and H. Kim, *Appl. Surf. Sci.*, 2009, **255**, 7073-7077.
15. Y. Liao, R. Wang and A. G. Fane, *J. Membr. Sci.*, 2013, **440**, 77-87.
16. S. A. Wang, Y. P. Li, X. L. Fei, M. D. Sun, C. Q. Zhang, Y. X. Li, Q. B. Yang and X. Hong, *J. Colloid Interface Sci.*, 2011, **359**, 380-388.
17. S. W. Meng, J. Mansouri, Y. Ye and V. Chen, *J. Membr. Sci.*, 2014, **450**, 48-59.
18. J. Zhang, Z. Y. Song, B. A. Li, Q. Wang and S. C. Wang, *Desalination*, 2013, **324**, 1-9.

19. F. J. Wang, S. Lei, J. F. Ou, M. S. Xue and W. Li, *Appl. Surf. Sci.*, 2013, **276**, 397-400.
20. A. M. A. Mohamed, R. Jafari and M. Farzaneh, *Appl. Surf. Sci.*, 2014, **288**, 229-237.
21. S. S. Madaeni, S. Zinadini and V. Vatanpour, *Sep. Purif. Technol.*, 2013, **111**, 98-107.
22. B. B. J. Basu and A. K. Paranthaman, *Appl. Surf. Sci.*, 2009, **255**, 4479-4483.
23. Z. R. Zheng, Z. Y. Gu, R. T. Huo and Z. S. Luo, *Appl. Surf. Sci.*, 2010, **256**, 2061-2065.
24. Z. R. Zheng, Z. Y. Gu, R. T. Huo and Y. H. Ye, *Appl. Surf. Sci.*, 2009, **255**, 7263-7267.
25. D. A. Zha, S. L. Mei, Z. Y. Wang, H. J. Li, Z. J. Shi and Z. X. Jin, *Carbon*, 2011, **49**, 5166-5172.
26. L. Zhang, D. A. Zha, T. T. Du, S. L. Mei, Z. J. Shi and Z. X. Jin, *Langmuir*, 2011, **27**, 8943-8949.
27. J. Biener, M. Stadermann, M. Suss, M. A. Worsley, M. M. Biener, K. A. Rose and T. F. Baumann, *Energy Environ. Sci.*, 2011, **4**, 656-667.
28. S. H. Kim, M. A. Worsley, C. A. Valdez, S. J. Shin, C. Dawedeit, T. Braun, T. F. Baumann, S. A. Letts, S. O. Kucheyev and K. J. J. Wu, *RSC Adv*, 2012, **2**, 8672-8680.
29. M. Tao, L. Xue, F. Liu and L. Jiang, *Adv. Mater.*, 2014, **26**, 2943-2948.
30. L. Feng, S. Li, Y. Li, H. Li, L. Zhang, J. Zhai, Y. Song, B. Liu, L. Jiang and D. Zhu, *Advanced materials*, 2002, **14**, 1857-1860.
31. Y. Zheng, X. Gao and L. Jiang, *Soft Matter*, 2007, **3**, 178-182.
32. R. N. Wenzel, *Industrial & Engineering Chemistry*, 1936, **28**, 988-994.
33. E. A. Vogler, *Adv Colloid Interface Sci*, 1998, **74**, 69-117.
34. J. M. Berg, L. T. Eriksson, P. M. Claesson and K. G. N. Borge, *Langmuir*, 1994, **10**, 1225-1234.
35. L. Feng, Y. Song, J. Zhai, B. Liu, J. Xu, L. Jiang and D. Zhu, *Angewandte Chemie*, 2003, **115**, 824-826.
36. C. Guo, L. Feng, J. Zhai, G. Wang, Y. Song, L. Jiang and D. Zhu, *Chemphyschem*, 2004, **5**, 750-753.
37. E. Hosono, S. Fujihara, I. Honma and H. Zhou, *J Am Chem Soc*, 2005, **127**, 13458-13459.

38. C. Reichardt and T. Welton, *Solvents and solvent effects in organic chemistry*, John Wiley & Sons, 2011.
39. H.-J. Li, Y.-M. Cao, J.-J. Qin, X.-M. Jie, T.-H. Wang, J.-H. Liu and Q. Yuan, *J Memb Sci*, 2006, **279**, 328-335.
40. B. Chakrabarty, A. Ghoshal and M. Purkait, *J Memb Sci*, 2008, **325**, 427-437.
41. B. Akhavan, K. Jarvis and P. Majewski, *ACS Appl. Mater. Interfaces*, 2013, **5**, 8563-8571.
42. J. G. Reynolds, P. R. Coronado and L. W. Hrubesh, *Journal of Non-Crystalline Solids*, 2001, **292**, 127-137.
43. G. Ross, J. Watts, M. Hill and P. Morrissey, *Polymer*, 2000, **41**, 1685-1696.
44. H. Kise and H. Ogata, *Journal of Polymer Science: Polymer Chemistry Edition*, 1983, **21**, 3443-3451.
45. H. Qi, E. Mäder and J. Liu, *Journal of Materials Chemistry A*, 2013, **1**, 9714-9720.
46. C. Zhao, X. Xu, J. Chen and F. Yang, *Journal of Environmental Chemical Engineering*, 2013, **1**, 349-354.
47. J. Zhang, Z. Xu, M. Shan, B. Zhou, Y. Li, B. Li, J. Niu and X. Qian, *J Memb Sci*, 2013, **448**, 81-92.

Chapter 6 Conclusions and Future Recommendations

Based on previous discussions on the respective three studies, the main findings and outcomes are briefly summarized in this chapter, which also includes the connection between each work. Some recommendations for future works have also been proposed.

6.1 Conclusions

Three studies have been conducted to address the scope of this thesis, focusing on the fabrication and properties investigations of PVDF/CNTs composites. In view of the critical role of CNTs surface properties in manufacturing of uniform composite, which affects realization of full CNTs functions, the surface functionalization of CNTs was firstly studied. The mechanical properties of materials often lay the foundation for other advanced functional properties. Therefore, the influence of CNTs on the mechanical performance of PVDF is investigated. As one important fluoropolymer, PVDF is widely used in separation applications. The oil/water separation potential of PVDF and its CNTs composite counterpart were examined. Promising results and main contributions of this thesis are summarized as follows:

- (1) An environmental-friendly approach was established for the surface functionalization of CNTs. This is a facile method that leads to a high yield of treated CNTs up to 90%, with very little reduction of the sp^2 graphitic carbon structure. The surface functionalization of both ether C-O-C and quinone C=O groups on CNTs surface enables the excellent dispersion of the treated CNTs in organic solvents including ethanol, acetone, chloroform and DMF.
- (2) The oxidation mechanism was proposed for elucidating the CNT oxidation in air condition. To formed C-O-C groups, representing the first and also the most crucial step is the 1, 4 peroxidation. After that, the π electrons in the two adjacent C=C bonds rearrange and simultaneously form single bonds with the two oxygen atoms, while the -O-O- bond breaks homolytically. The formation of C=O groups begins with a 1, 2 peroxidation on the graphitic ring, and this is followed by simultaneous hemolytic breaking of C-C and O-O bond, leading to the formation of two quinone groups.
- (3) PVDF/CNTs nanocomposite with uniform CNTs dispersion and distribution were fabricated through a method of solution mixing and melt blending. The nanocomposites demonstrated significantly enhanced ductility and toughness at very

- low CNTs concentration (0.2 wt. %), without compromising the yield strength and the modulus.
- (4) The mechanism behind the drastically enhanced ductility of PVDF/CNTs is illustrated. It is believed that the γ phase of PVDF transformed into β crystallite during the stretching process. The disassembly of γ phase and re-assembly into β crystallite create a plasticized zone around CNT. This plasticized zone leads to striking increase of ductility and fracture toughness of the resultant composites. Simultaneously, CNTs also hinder the propagation of microcracks via “pinning effect”, further preventing fusion of the macrocracks and therefore synergistically contributing to the enhanced ductility and toughness.
- (5) PVDF aerogel was prepared via a physical phase inversion process. The aerogel is both superoleophilic and superdrophobic owing to its unique hierarchical micro-nano structure. Both surfactant free and surfactant stabilized water-in-oil emulsions can be effectively separated with gravity as the only driving force. The PVDF aerogel also exhibits moderate oil absorption capacity and almost instantaneous oil up-taking when tested using various types of oil.
- (6) PVDF/CNTs composite aerogel is also prepared using the same methodology for producing PVDF aerogel. Both compression strength and modulus are enhanced with the introduction of low loading content of CNT without impairing the surface properties.

6.2 Recommendations for Future Works

6.2.1 Investigation of CNTs Induced Phase Transition in Other Polymer Systems

In chapter 5, we have investigated the CNTs induced phase transition phenomenon. Along with the phase transition is the remarkable increase in ductility and toughness. This study indicates that an in-depth understanding of polymorphism and precise

manipulation of transformation between each phase might be valuable for many applications. In addition to PVDF, many polymers possess more than one crystalline structure, such as iPB (isotactic polybutene)¹, s-PS (syndiotactic polystyrene)², PTFE (poly(tetrafluoroethylene))³, ETFE(ethylene-tetrafluoroethylene)⁴, iPP (isotactic polypropylene)⁵, nylon 6⁶, poly (tetramethylene succinate)⁷. As a matter of fact, it is believed that most of the crystalline polymer can be polymorphic, only if the right crystallization condition is identified.⁸

Previous studies discovered that the phase transition could be triggered by controlling the crystallization temperature and rate⁹, the thermal treatment¹⁰ or the use of external fields⁶. However, the effect of nanofillers, such as CNTs, toward the phase transition has not been systematically examined. Not only mechanical performance, many other physical properties can also be greatly affected by this kind of nanofiller induced (or promoted) phase transition. Therefore, additional studies could be performed on the nanocomposite polymorphism.

6.2.2 Enhancement of the Mechanical Properties of PVDF Aerogel

To facilitate the stress transfer between CNTs and PVDF aerogel matrix, CNTs can be chemically bonded with PVDF molecules. As early as in 1991, the generation of oxygen-containing group in PVDF was reported¹¹. In the following two decades, several groups¹²⁻¹⁴ deepened their understanding and found that hydroxyl groups can be produced in PVDF. Therefore, PVDF polymer chain can be functionalized with hydroxyl groups while CNT might be functionalized with carboxylic groups. The PVDF containing hydroxyl groups can react with carboxylated CNT to form PVDF/CNT hybrid. The chemical bonding between CNTs and PVDF matrix is promising in enhancing mechanical properties of PVDF/CNTs composite aerogel.

In addition to adding CNTs into PVDF aerogel, it is hypothesized that by crosslinking the PVDF molecules, both the mechanical properties and the durability can be further enhanced. In previous work, we have found that double bonds could be generated in PVDF polymer chain with alkali solution. The treated PVDF containing double bond can

be activated by organic peroxide, such as dicumyl peroxide, to promote/induce crosslinking. The reaction could be carried out by reactive extrusion.¹⁵⁻¹⁷

6.2.3 Functionalize CNTs with Other Reactive Gases

In Chapter 6, CNTs were surface functionalized through gas phase air annealing. Compared with the conventional liquid boiling approaches, gas phase reaction has the advantage of simple operation, high efficiency and low toxicity to environment. More importantly, the tedious purification procedures after functionalization, such as washing, filtration and drying process can be either avoided or simplified. In our work, oxygen is adopted as the reactive gas to oxidize the functionalized CNTs. Since many materials may have high oxidizing property, they might be used to functionalize CNTs or other carbon materials, such as graphene or carbon nanofibers. The gases may react with the carbon materials in the gas phase that contains, but not limited to ozone, NH_3 gas, HNO_3 gas, HCl gas, CO (carbon monoxide), SO_x (sulfur oxide), F_2 (Fluorine), Cl_2 (chlorine), Br_2 (bromine), I_2 (iodine), NO_x (nitrogen oxide), H_2 (hydrogen), C_2H_2 (acetylene) and other volatile organic compounds. The study by Ming and his colleagues¹⁸ indicates that system at high pressure may greatly reduce the amount of required oxidant and enhance the reactivity. Therefore, a higher pressure system may be employed involving many reactive gases.

6.2.4 Modeling and Simulation

Modeling and simulation is a beneficial commentary part to provide a more comprehensive understanding in atom or molecular scale. Quite a few simulation works have been performed on PVDF materials, most of which focus on the ferroelectricity. Using Monte Carlo computations, Kühn et al.¹⁹ showed that the typical dielectric and ferroelectric properties resulting from the dipole–dipole interaction and the coercive field increases if monolayer numbers decrease, which is consistent with experimental results. Zhu et al.²⁰ investigated the origin of piezoelectricity in β phase PVDF using the energy-minimization method in molecular simulation, and found that piezoelectricity is mostly

governed by the dimensional effect. Besides, polarization switching phenomena, the effect of doping on ferroelectricity and relaxation process of PVDF have also been studied in many simulation works.²¹⁻²³ Many techniques have also been used to simulate CNTs filled polymer system, such as molecular dynamic approaches, micromechanical approach and multiscale modeling.²⁴ In future work, simulation works could be performed to investigate the effect of the introduction of CNTs on the crystallization of different phases, the mechanism behind the phase transformation among different PVDF phase influence the ductility, modulus and yield strength, the effect of CNTs pinning effect on the mechanical response of composites, and so on. On top of that, simulations can also be expanded to model the attack of oxygen atom towards carbon atom on CNT wall and oil/water separation process on the surface of PVDF aerogel.

References

1. F. Danusso and G. Gianotti, *Die Makromolekulare Chemie*, 1963, **61**, 139-156.
2. Y. Chatani, Y. Shimane, T. Inagaki, T. Ijitsu, T. Yukinari and H. Shikuma, *Polymer (Guildf)*, 1993, **34**, 1620-1624.
3. P. Corradini, C. De Rosa, G. Guerra and V. Petraccone, *Macromolecules*, 1987, **20**, 3043-3046.
4. A. Funaki, S. Phongtamrug and K. Tashiro, *Macromolecules*, 2011, **44**, 1540-1548.
5. C. De Rosa, G. Guerra, R. Napolitano, V. Petraccone and B. Pirozzi, *Eur Polym J*, 1984, **20**, 937-941.
6. K. Miyasaka and K. Ishikawa, *Journal of Polymer Science Part A - 2: Polymer Physics*, 1968, **6**, 1317-1329.
7. Y. Ichikawa, J. Washiyama, Y. Moteki, K. Noguchi and K. Okuyama, *Polym. J.*, 1995, **27**, 1230-1238.
8. P. Corradini and G. Guerra, in *Macromolecules: synthesis, order and advanced properties*, Springer, 1992, pp. 183-217.
9. G. Guerra, V. M. Vitagliano, C. De Rosa, V. Petraccone and P. Corradini, *Macromolecules*, 1990, **23**, 1539-1544.
10. M. Iuliano, C. De Rosa, G. Guerra, V. Petraccone and P. Corradini, *Die Makromolekulare Chemie*, 1989, **190**, 827-835.
11. R. Crowe and J. P. S. Badyal, *J. Chem. Soc., Chem. Commun.*, 1991, 958-959.
12. J. Marchand - Brynaert, N. Jongen and J. L. Dewez, *J. Polym. Sci., Part A: Polym. Chem.*, 2000, **35**, 1227-1235.
13. Y. Chen, W. Sun, Q. Deng and L. Chen, *J. Polym. Sci., Part A: Polym. Chem.*, 2006, **44**, 3071-3082.
14. X. Zhao, L. Song, J. Fu, P. Tang and F. Liu, *Surf Sci*, 2011, **605**, 1005-1015.
15. Y.-J. Sun, G.-H. Hu, M. Lambla and H. K. Kotlar, *Polymer (Guildf)*, 1996, **37**, 4119-4127.
16. G. Moad, *Prog Polym Sci*, 1999, **24**, 81-142.
17. D. Shi, J. Yang, Z. Yao, Y. Wang, H. Huang, W. Jing, J. Yin and G. Costa, *Polymer (Guildf)*, 2001, **42**, 5549-5557.

18. J. Ming, Y. Wu, Y. Yu and F. Zhao, *Chem. Commun.* , 2011, **47**, 5223-5225.
19. M. Kühn and H. Kliem, *physica status solidi (b)*, 2008, **245**, 213-223.
20. G. Zhu, Z. Zeng, L. Zhang and X. Yan, *Comput. Mater. Sci.* , 2008, **44**, 224-229.
21. V. Bystrov, *Physica B* 2014, **432**, 21-25.
22. N. Lee, J. Lee, T. Ryu, Y. Kim, Y. Lansac and Y. H. Jang, *Science of Advanced Materials*, 2014, **6**, 2422-2427.
23. J. Miao, R. S. Bhatta, D. H. Reneker, M. Tsige and P. L. Taylor, *Polymer (Guildf)*, 2015, **56**, 482-489.
24. G. Pal and S. Kumar, *Prog. Aerosp. Sci.* , 2016, **80**, 33-58.